Author Email: bibhutib@gmail.com

MAGNETIC NANOCOMPOSITE MATERIALS

Thesis

Submitted in partial fulfillment of the requirements for the degree of

DOCTOR OF PHILOSOPHY

by

BIBHUTI BHUSAN NAYAK
(00411005)

Supervisors:

Prof. D. Bahadur
and
Prof. Satish Vitta

DEPARTMENT OF METALLURGICAL ENGINEERING AND MATERIALS SCIENCE

INDIAN INSTITUTE OF TECHNOLOGY, BOMBAY

2006

APPROVAL SHEET

Thesis entitled "**MAGNETIC NANOCOMPOSITE MATERIALS"** by **BIBHUTI BHUSAN NAYAK** is approved for the degree of **DOCTOR OF PHILOSOPHY**.

Examiners

_____

_____

Supervisors

_____

_____

Chairman

_____

Date: _____

Place: _____

INDIAN INSTITUTE OF TECHNOLOGY, BOMBAY, INDIA

CERTIFICATE OF COURSE WORK

This is to certify that Mr. Bibhuti Bhusan Nayak was admitted to the candidacy of the Ph. D. degree on 02.01.2001, after successfully completing all the courses required for the Ph. D. Degree Programme. The details of the course work done are given below.

Sr. No.	Course No.	Course Name	Credits
1.	MM 678	Magnetism and Magnetic Materials	6.00
2.	MM684	X-Ray Diffraction and Electron Microscopy	6.00
3.	MMS801	Seminar	4.00
4.	MM685	Electrical and Magnetic Materials	AU
5.	MM691	Topics in Phase Transformations	AU

I. I. T, Bombay

Dated: _____

Dy. Registrar (Academic)

TO MY PARENTS

LATE RANGADHAR NAYAK

AND

Smt. SNEHALATA NAYAK

CONTENTS

ABSTRACT

The present work deals with synthesis of composite materials consisting of magnetic nanoparticles dispersed in a magnetic or nonmagnetic insulating matrix and a study of their transport and magnetic properties. Two types of composites: ceramic–ceramic and metal–ceramic have been synthesized using three different techniques, microwave refluxing, glass-ceramic and aqueous reduction. These techniques promote formation of composites at the nano level, which is one of the primary aims of this thesis. These techniques are highly versatile and can be used for the synthesis of a wide variety of materials. Moreover, synthesis of nanocomposites using these techniques has not been investigated in detail earlier and this forms the objective in using these techniques.

In ceramic–ceramic system, the main magnetic material is manganite with a perovskite type structure. The manganites are of interest because they exhibit colossal magnetoresistance (CMR) behavior and enhancing the magnitude of CMR is of significant interest. Two different combinations of composites: magnetic phase distributed in magnetic or nonmagnetic matrix have been synthesized.

In the magnetic–magnetic ceramic system, the work describes the structural, transport and magnetic properties of nanocrystalline CMR oxide, $La_{0.67}Ca_{0.33}MnO_3$ (LCMO) and their distribution in a magnetic insulating $NiFe_2O_4$ (NF) matrix synthesized using microwave refluxing. The structural, transport and magnetic properties are found to depend strongly on the Mn^{4+} concentration, grain size, pH of the precursor solution and the annealing temperature. In the magnetic–nonmagnetic system, the work describes the structural, transport and magnetic properties of LCMO distributed in an insulating nonmagnetic silicate or borate matrix synthesized using glass-ceramic route. Selection of glass composition and effect of nucleating agents are the important factors for making nanocomposites using this technique. The CMR property of LCMO is found to vanish in the case of LCMO/NF nanocomposites with increasing NF content while isolation of LCMO by SiO_2 or borate based glass leads to loss of CMR behavior. These results clearly show that both magnetic and transport properties depend on interactions between LCMO grains.

In metal–ceramic nanocomposite system, Ni: NiO/ZrO_2 nanocomposite materials have been studied in detail. Different size and shapes (spherical, cylindrical, ellipsoid, hexagonal and polyhedral) of Ni nanoparticles with a core-shell structure have been synthesized by chemical reduction using sodium borohydride as a reducing agent. Crystalline Ni varying in size from 2 nm to 26 nm distributed in a non-magnetic matrix of NiO/ZrO_2 has been prepared at room temperature by controlling the time of reaction and addition of Zr-salt solution of different concentrations. The crystalline Ni clusters are found to be ferromagnetic at room temperature with a well defined hysteresis and coercivity. The absolute resistivity of the annealed samples (in H_2 atmosphere) decreases up to $x \leq 0.10$ (where x is the molar concentration of Zr-salt) and then increases with the concentration of Zr-salt. These results are in agreement with the microstructural results, which show that initially the addition of Zr-salt promotes Ni formation leading to a better inter-particle connectivity. For $x > 0.10$, the inter-particle connectivity is reduced due to ZrO_2 encapsulation and hence results in an increase in resistivity. The microstructural results together with the transport and magnetic properties of the nanoparticle system clearly show the potential of this technique to obtain size controlled property tuning.

Keywords: Magnetic nanocomposite; Colossal magnetoresistance; Nanoparticle; Microwave refluxing; Glass-ceramic; Chemical reduction; Electrical transport; Magnetetoresistance.

ACKNOWLEDGEMENTS

With deep regards and profound respect, I avail this opportunity to express my deep sense of gratitude and indebtedness to Professor D. Bahadur and Professor Satish Vitta, Metallurgical Engineering and Materials Science, IIT Bombay, for introducing the present research topic and for their inspiring guidance, constructive criticism and valuable suggestion throughout in this research work. It would have not been possible for me to bring out this thesis without their help and constant encouragement. I am also thankful to Madam Ruby Bahadur and Madam Dr. Padma Satish for giving me love and support.

I am also grateful to Prof. C. M. Srivastava whose vast knowledge in the field of science and technology has enlightened me in different areas of this experimental research work. His deep sense of appreciation and dedication to research has been a constant source of inspiration to me.

I would like to express my gratitude to Head of the department for their cooperation in one way or the other. I wish to record my thanks and gratitude to Prof. Om Prakash and Prof. K. G. Suresh members of the RPC committee, and also to other faculty members of Metallurgical Engineering and Materials Science for their valuable suggestions and encouragements at various stages of the work.

I am grateful to Prof. A. K. Nigam of the 'Low Temperature Physics' group of Tata Institute of Fundamental Research (TIFR) for conducting magnetic measurements using VSM and SQUID on many of my samples. I am also thankful to Dr. T. K. Gundu Rao of Sophisticated Analytical Instrument Facility (SAF), IIT-Bombay, for his valuable suggestions and encouragements. I am thankful to Dr. S.L. Kamath for his help in carrying out SEM and DTA analysis in our department.

I would like to thank all of my "Maglab" members especially Dibakar, Saket, Rajkumar, Pallab, Giri, Kanhu, Harsha, Nandkishore, Ritu, Chandu and Dhuri for providing all joyful environment in the lab and helping me out in different ways.

My special thanks go to few of my endless list of friends Himanshu Saxena, Sunil (tikole), Deepak (petu), BibhuP, Suraj, Umasankar, Vikram Dabhade, Vikram Singh, Ajay, Neeraj, Santosh, Devidas, Kiran (KK), Pankaj bhai and Akhyaya bhai. I must recall my childhood best friends Sameer, Manoj, Sukant, Soumendra, Saroj and Anjan. Their friendship is a blessing my heart will always treasure. I also thank to all my teachers and professors, from academic and nonacademic levels, who inspire me to be wise and knowledgeable. I am truly indebted to all who have supported me and brought me so far.

I am thanking my beloved wife Dr. Aparna Mondal for all the hope, true love, affection, caring, concern and constant encouragement she lends. She gives me many reasons to smile everyday and to pursue my research work happily. I would like to thank her family members for giving me love and support.

I would like to thank my parents and other family members, uncles, aunties, brothers (Kishore, Rajkishore, Bhudev), brother-in-laws, sisters, sister-in-laws for their support for choices in all my life and their love, which has been a constant source of strength for everything I do. I feel a deep sense of gratitude for my father Late Rangadhar Nayak and mother Smt. Snehalata Nayak who formed a part of my vision and taught me the good things that really matter in life.

I also mention the sweet company of my niece Nikki, Naina, and nephew Rahul Raj. I appreciate their gifts beyond measure.

I am happy to acknowledge Department of Science and Technology and IIT Bombay for sponsoring me to attend and present my research papers in International INTERMAG 2005 conferences at Nagoya, Japan. It was a great experience for me to interact with leading scientists and academicians from various universities in the world during my visit.

24th July 2006

(Bibhuti Bhusan Nayak)

List of Figures

List of Tables **Page No**

Nomenclature

a, b, c	Lattice parameters
α	Temperature coefficient of resistance
β	Angular line width of half maximum intensity (X-ray diffraction)
d_h	hydrodynamic diameter
ΔE	Difference between FM, ground state and PM, insulating state
E_0	ΔE at T = 0
E_g	Activation energy for polaron mediated conduction
FM	Ferromagnetic
H	Magnetic field
H_c	Coercive field strength
K	Kelvin
k_B	Boltzman Constant
λ	X-ray wavelength
M	Magnetization
m	Magnetic moment
m (T)	Metallic volume fraction at temperature T
MD	Multi domain
M_s	Saturation magnetization
M_r	Remanent Magnetization
MR	Magnetoresistance
(N)	Normality of the Solution
PM	Paramagnetic
R	Resistance
R (0)	Resistance at zero magnetic field
R (H)	Resistance at magnetic field H
ρ	Resistivity
ρ (0)	Resistivity at zero magnetic field
ρ (H)	Resistivity at magnetic field H
ρ_{ht}	Resistivity at semiconducting region
ρ_{lt}	Resistivity at ferromagnetic region

ρ_0	Residual resistivity at T = 0
T	Absolute temperature in K
T_c	Curie temperature
T_{MI}	Metal-insulator transition temperature
T_B	Blocking temperature
T_N	Néel temperature
SP	Superparamagnetic
SD	Single domain
t	Tolerance factor
θ	Bragg's angle
V	Particle Volume
ω_s	Average frequency of the soft optical mode
DTA	Differential thermal analysis
FC	Field cooled magnetization
PCS	Photo correlation spectroscopy
SQUID	Superconductive quantum interference device magnetometer
TEM	Transmission electron microscopy
TGA	Thermogravimetric analysis
VSM	Vibrating sample magnetometer
XRD	X-ray diffraction
ZFC	Zero field cooled

Chapter 1

GENERAL INTRODUCTION

1.1 Introduction

Materials with features on the scale of nanometer often have properties dramatically different from their bulk scale counterparts. Nanocrystalline materials are single phase or multiphase polycrystals, the crystal size of which is of the order of few nanometers so that about 40 to 80 % of the atoms are in the grain boundaries [1]. Nanostructure science and technology is a broad and interdisciplinary area of research and development activity that has been growing worldwide in the past decades [2]. Important among these nanoscale materials are nanocomposites, in which the constituents are mixed at nanometer length scale. They often have properties that are different compared to conventional microscale composites and can be synthesized using simple and inexpensive techniques. The study of nanocomposite materials requires a multidisciplinary approach with impressive technological promise, involving novel synthesis techniques and an understanding of physics and surface science [3].

During the last decade, the development of magnetic nanocomposite materials has been the source of discovery of spectacular new phenomena, with potential applications in the fields of information technology, telecommunication or medicine [4, 5]. Magnetic nanocomposite materials are generally composed of ferromagnetic particles (grain size in nanometer scale) distributed either in a non-magnetic or magnetic matrix [6, 7]. The shape, size and distribution of the magnetic particles play an important role in determining the properties of such materials [8]. The matrix phase separates the magnetic particles and changes the magnetic exchange interaction. This affects the transport and magnetic properties. Therefore, understanding and controlling the structure of materials is essential to obtain desired physical properties.

Hence in this chapter, a general introduction to the important magnetic properties of nanomaterials, colossal magnetoresistance (CMR) materials, and various electrical transport mechanisms are described based on literature. The organization of thesis is given in the last part of this chapter. The main objective of the present work is presented at the end of the second chapter, which is based on a critical literature survey.

1.2 Magnetic properties of nanomaterials

The effect of reducing the physical size of materials is of great importance from both fundamental considerations and modern practice. A brief discussion of magnetic behavior of low dimensional systems is focused based on literature. Magnetic nanoparticles exhibit

specific properties such as coercivity and superparamagnetism, generally attributed to reduced dimensions.

1.2.1 Coercivity

The coercivity of fine particles has a striking dependence on their size. Fig. 1.1 shows very schematically, how the size range is divided, in relation to the variation of coercivity with particle radius r.

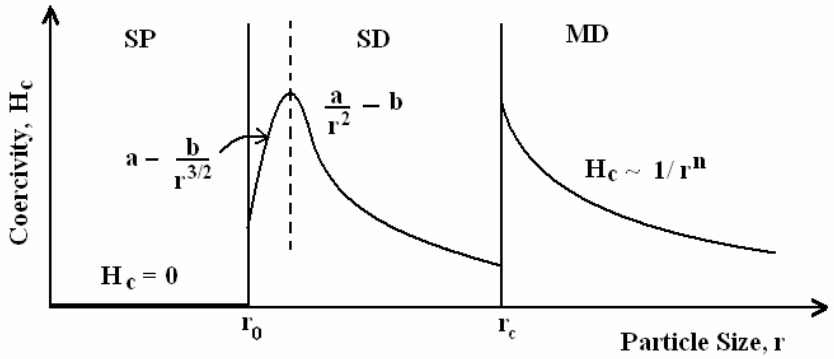

Fig. 1.1: Overview of the size dependence of coercivity exhibited by magnetic particles: $H_C = 0$ below superparamagnetic (SP) particle size limit r_0; single-domain behavior (SD) between r_0 and the single domain limit r_c; and multidomain behavior (MD) for $r > r_c$. [Adapted from ref. 9]

Beginning at larger size the following regions can be distinguished:

(i) Multi-domain (MD): It is observed for $r > r_c$ and in this region, the coercivity decreases as the particle size increases and the coercivity H_c is found to vary with size as $\sim 1/r^n$.

(ii) Single-domain (SD): For $r_0 < r < r_c$, the particles become single domain and in this size range, the coercivity reaches a maximum.

(iii) Superparamagnetic (SP): Below a critical size r_0, the coercivity is zero because of thermal effect, which is strong enough to spontaneously demagnetize the assembly of magnetic particles.

1.2.2 Superparamagnetism

The effective magnetic moment of a ferromagnetic particle is determined by its size. A ferromagnetic sample with a volume greater than a critical value V_c divides into multiple magnetic domains, each magnetized along the local easy axis but in one of two opposite

directions. The multiple domain structure is, however, no longer favorable below the critical volume, and the particle becomes a single domain with ferromagnetic alignment of all its moments along the easy axis in the same direction. Thermal fluctuations of the moment exist on a microscopic scale, but to reverse the direction of the single domain's magnetization requires an energy ΔE to overcome the crystal-field anisotropy. If single domain particles become small enough, KV would become so small that thermal fluctuations could overcome the anisotropy forces and spontaneously reverse the magnetization of a particle from one easy direction to the other, even in the absence of an applied field. Each particle has a magnetic moment $\mu = M_s V$ and, if a field is applied, the field will tend to align the moments of the particles and the thermal energy will tend to disalign them. This is called superparamagnetism. The probability of such a reversal by thermal activation is proportional to $\exp(-\Delta E/kT)$. This differs from conventional paramagnetism because the effective moment of the particle is the sum of its ionic particles, which can be several thousand spins in a ferromagnetic particle small enough to show superparamagnetism [9].

Very fine ferromagnetic particles have very short relaxation times even at room temperature and behave superparamagnetically; that is, their behavior is paramagnetic but their magnetization values are typical of ferromagnetic substances. The individual particles have normal ferromagnetic moments but very short relaxation times so that they can rapidly follow directional changes of an applied field and, on removal of the field, do not hold any remanent moment. Superparamagnetism is characterized by two experimental features:

1. There is no hysteresis; (i.e., both the retentivity and the coercivity are zero) in the field dependence of magnetization.
2. Magnetization curves measured at different temperatures superimpose when magnetization (M) is plotted as a function of Field (H) / temperature (T).

Superparamagnetism can be destroyed by cooling. This follows because the characteristic fluctuation time for a particle's moment varies exponentially with temperature, so the magnetization appears to switch sharply to a stable state as the temperature is reduced. The temperature at which this occurs is called the blocking temperature (T_B), and it depends linearly on the sample's volume and on the magnitude of the crystal-field anisotropy.

In the case of superparamagnetic materials, the magnetization shows temperature and path dependence which is shown schematically in Fig. 1.2.

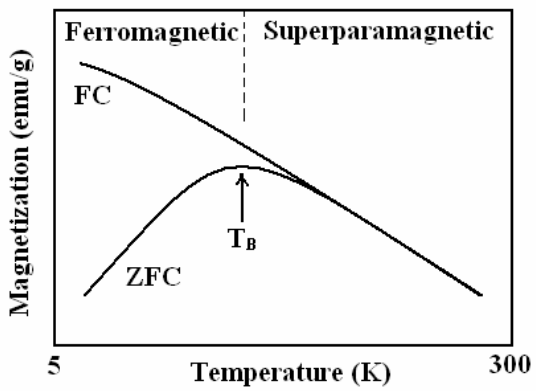

Fig. 1.2: Schematic diagram of ZFC and FC magnetization curves as a function of temperature taken in an applied field H. Arrow indicates blocking temperature, T_B.

The two curves zero field cooled (ZFC) and field cooled (FC) show different behavior at low temperatures. As the temperature increases the magnetic moment in the FC curve decreases. However, as the temperature begins to rise from 5 K, the moment in the ZFC curve begins to increase. At a certain temperature, the ZFC curve reaches a peak and this temperature is called the blocking temperature (T_B). The divergence of ZFC and FC curve and the blocking temperature depend on the particle size and its distribution. The blocking temperature of a substance should decrease with increasing applied field and eventually disappear when the field reaches a critical value. The higher field is expected to lower the barriers between the two easy axis orientations.

For a particle of constant size below the blocking temperature T_B, the magnetization will be stable and shows hysteresis. It refers to particles which have relaxation time for demagnetization longer than 100 sec. For uniaxial particles using the same criterion for stability gives,

$$T_B = \frac{KV}{25k} \qquad 1.1$$

Where K = Anisotropy constant

V = Volume of the particle

k = Boltzmann's constant (1.38×10^{-23} J K^{-1})

If one considers Ni as a classical example with an anisotropy constant K = 4.5×10^3 J m^{-3} then for a size 20 nm, the particle will show a blocking temperature (T_B) at ~ 55 K using equation 1.1. Below T_B, the magnetization will have relatively stable and shows ferromagnetic behavior. While above T_B, the thermal energy will be sufficient to suppress the ferromagnetic behavior and thus the particles become superparamagnetic.

1.3 Colossal magnetoresistance (CMR)

Magnetoresistance (MR) in materials is of enormous technological importance, as these materials can be used as read heads for hard disks, magnetic storage and sensing devices. The effectiveness of these materials is directly related to the percentage change of resistance in an external magnetic field. MR is defined as

$$MR(T) = \frac{[\rho(H,T) - \rho(0,T)]}{\rho(0,T)} \qquad 1.2$$

$\rho(H, T)$ and $\rho(0, T)$ are the resistivity at a given temperature T in the presence and absence of magnetic field H respectively. A negative MR was first found in perovskite manganites, exhibiting huge decrement in electrical resistivity in the presence of magnetic field. The perovskite manganites of the general formula $RE_{1-x}A_xMnO_3$ (RE = trivalent rare-earth element such as La, Pr, Sm, Gd etc and A = divalent alkaline earth ions such as Ca, Sr, Ba, etc) has spurred considerable interest in recent years because of their colossal magnetoresistance (CMR) behavior. In perovskite structure, (RE, A) elements occupy the A-site position (corner of a cube) and manganese occupies the B-site position (body center of a cube). All the face-centered positions are occupied by oxygen. At low temperature, the resistivity is metallic both in magnitude as well as in its dependence on temperature. With increase of temperature, it increases up to a temperature, T_{MI} (called the metal – insulator transition temperature) beyond which it decreases having a negative temperature coefficient of resistance while maintaining a large magnitude. This metal to insulator transition at this temperature T_{MI} is usually accompanied by a ferromagnetic to paramagnetic transition. The coexistence of metallic conductivity and ferromagnetic coupling in these materials at low temperature has been explained in terms of a double exchange mechanism, proposed by Zener in 1951 [10]. This mechanism involves the excitation of d electron from the Mn cation with the highest number of such electrons (lower valency, Mn^{3+} in the present case) into an overlapping anion orbital (O^{2-} ion in this case), with the transfer of one anion p electron to other cation (Mn^{4+} in the present case). This type of electron hopping is schematically shown in Fig. 1.3. Simultaneous transfer of an electron from Mn^{3+} to O^{2-} and from O^{2-} to Mn^{4+} is called double exchange.

Fig. 1.3: Schematic shows Double exchange mechanism in manganites. [Adapted from ref. 10]

Fig. 1.4 shows schematic electronic phase diagram of $La_{1-x}Ca_xMnO_3$ (a CMR oxide) showing the compositional stability of different phases. The Curie temperature is maximized at x = 3/8 according to Cheong and Hwang [11], contrary to the x = 0.30 believed by many to be the most optimal compositions for ferromagnetism.

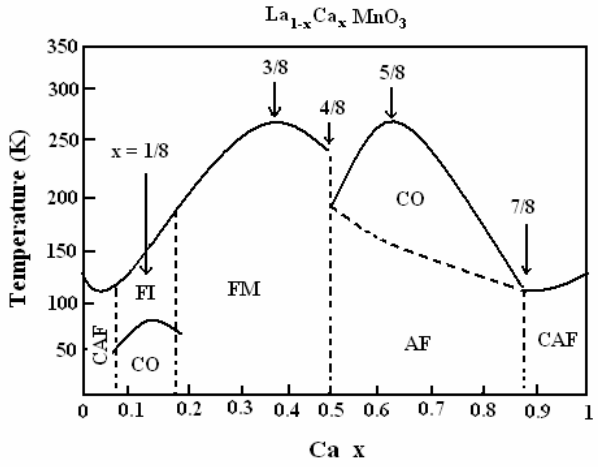

Fig. 1.4: Schematic electronic phase diagram of $La_{1-x}Ca_xMnO_3$ showing the compositional stability of different phases. FM: Ferromagnetic metal, FI: Ferromagnetic Insulator, AF: Antiferromagnetism, CAF: Canted AF, and CO: Charge/Orbital Ordering. [Adapted from ref.11]

The electrical transport in these materials exhibits both insulating and metallic behavior depending on the transition temperature T_{MI}. Since the transport mechanism in the two states is different, these transport mechanisms are discussed in brief in the next section.

1.4 Electrical Transport

The resistivity as a function of temperature and or composition for a material can be represented as in Fig. 1.5. The curve can be described as consisting of two different regions. In the low temperature regime, the resistivity increases with temperature and in the high temperature regime, the resistivity decreases with increasing temperature. The resistivity has a metallic behavior ($d\rho/dT > 0$) below the peak and a semiconducting (insulator) behavior ($d\rho/dT < 0$) above.

The conduction mechanism in the manganites exhibits both metallic and insulating behavior depending on composition and temperature. In a particular composition range, the manganites undergo insulator to metal transition on cooling and hence this is used as a model system to describe briefly the various electrical transport mechanisms.

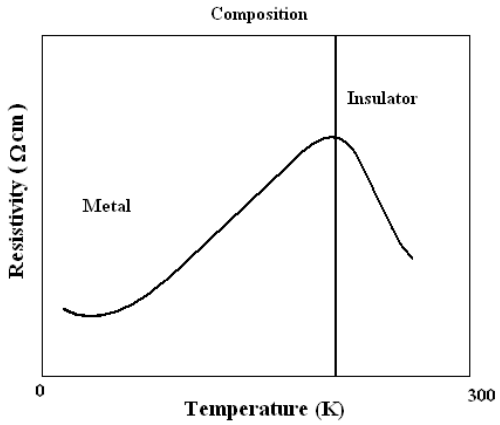

Fig. 1.5: A typical resistivity versus temperature and composition for a material

(i) Insulating region

Temperature causes electrons to be excited in to the conduction band and hence resistivity is considered as a thermally activated process. Jonker and Van Santen [12] measured the resistivity of $LaMnO_3$-$AMnO_3$ (where A = Ca, Sr and Ba) and they found that the resistivity plotted as log ρ versus 1/T, was linear, showing a thermally activated behavior given by the relation.

$$\rho(T) = A \exp\left(\frac{E_0}{k_B T}\right) \qquad 1.3$$

where E_0 is the activation energy, k_B Boltzmann's constant and *A is* a constant which depends on the mobility of the charge carriers.

An alternative electrical transport mechanism in insulating region is due to the formation of polarons (strong coupling between an electron and phonons). The following behavior has also been suggested which is due to polaron mediated hopping [14];

$$\rho(T) = B T \exp\left(\frac{E_0}{k_B T}\right) \qquad 1.4$$

where B is a measure of ideal conductivity at elevated temperatures and depends on polaron concentration. The activation energy for polaron mediated conduction is given by E_0.
Yeh et al. [13] fitted the resistivity behavior using the following equation

$$\rho(T) = \rho_0 T^{\alpha} \exp\left(\frac{E_0}{k_B T}\right) \qquad 1.5$$

where ρ_0 is the residual resistivity at T = 0, α equal to 1.6, identifying the behavior as non-adiabatic small polaron hopping in most cases, and α equal to 1 in some cases. In all cases their data was best fitted with some type of polaronic hopping [14]. Other groups have found that variable range hopping (VRH) best describes the electronic transport. VRH was

suggested by Mott to describe transport at low temperatures when the electronic states are localized near Fermi energy [15]:

$$\rho(T) = \rho_0 \exp\left(\frac{E_0}{K_B T}\right)^{1/4} \qquad 1.6$$

Coey et al. [16] found that this kind of expression best fitted their data on a variety of films. To summarize, in the paramagnetic insulating region there is clear evidence of activated behavior, but there is no agreement on the exact form of temperature dependence.

(ii) Metallic region

In the metallic region the resistivity has been found to be quite well described by

$$\rho(T) = \rho_0 + C T^2 + D T^n \qquad 1.7$$

where ρ_0 is the residual resistivity at T = 0, C the electron-electron scattering coefficient and D the electron – phonon or electron – magnon scattering coefficient [17]. The value of n has been predicted to be 5 for electron – phonon scattering while it has a value of 4.5 for electron – magnon scattering [18].

1.5 Organization of the thesis

The physical size of the material when reduced to nanodimensions affects the transport and magnetic behavior. Hence, the effect of size on magnetic behavior together with the colossal magnetoresistance mechanism is discussed in chapter 1. Chapter 2 provides a detailed discussion of literature on CMR materials and Ni nanoparticles. The synthesis and properties of nanocomposites of these materials are also discussed in chapter 2. The main objective of the present work, which is based on the literature survey, is presented towards the end of chapter 2. In chapter 3, the various synthesis and characterization techniques used in the present work are described in detail. Chapter 4 describes the results of $La_{0.67}Ca_{0.33}MnO_3$ (LCMO), a CMR material synthesis and characterization. The synthesis and characterization of nanocomposites of this CMR material in a magnetic, insulating Ni-ferrite are also discussed in this chapter. Chapter 5 describes the synthesis and characterization of LCMO: SiO_2 (nonmagnetic insulator) nanocomposites prepared by glass-ceramic process with and without the addition of nucleating agents. Chapter 6 describes the microstructural evolution of Ni nanoparticles synthesized through an aqueous reduction technique. Finally, conclusions of Ph.D. work are given in Chapter 7. Synthesis of Ni and Ni-nickel oxide nanoparticles with different shapes and a core shell structure are discussed in appendix.

Chapter 2

LITERATURE REVIEW

2.1 CMR nanocomposites

Since the discovery of large, negative magnetoresistance (CMR) in manganites, several studies have been conducted on enhancing this property [19]. The manganites undergo a paramagnetic (semiconducting) to ferromagnetic (metallic) transition on cooling which is accompanied by a large conductivity enhancement in the presence of an external magnetic field – negative magnetoresistance. The different methods used for enhancing this property are: substitution doping [20], grain size reduction [21], distribution of the manganite grains in a non-magnetic insulating matrix and magnetic insulating matrix [8]. The paramagnetic, semiconducting state to ferromagnetic, metallic state transition temperatures are found to decrease with substitution doping and grain size reduction. The lowering of transition temperatures is accompanied by an increase in resistivity and reduced saturation magnetization. The magnetoresistance on the other hand is found to increase with decreasing temperature in the ferromagnetic, metallic state.

The earliest work reported in the area of CMR composites was by Li Balcells *et al.* [22] and Petrov *et al.* [23]. Li. Balcells *et al*. [22] have studied the magnetoresistance of x LSMO/ $(1 - x)CeO_2$ composite (x = 100, 80, 60, 40, 30, 25, 20 vol.%) as a function of metal/insulator composition, temperature and magnetic field and have found a dramatic enhancement of LFMR for samples close to the metallic percolation threshold. Petrov *et al.* [23] have studied the electrical and magnetic transport properties of x LCMO / $(1 - x)$ $SrTiO_3$ (x = 10–100 vol.%) composites. A high field MR as well as LFMR close to percolation threshold, x_c = 60% is attributed due to increased disorder in the grain boundary and is almost over an order of magnitude higher than the corresponding pure LCMO value.

Composites with other insulating materials like yttria-stabilized zirconia (YSZ) [24], silica (SiO_2) [25], alumina (Al_2O_3) [26] are also reported. $(LSMO)_{1-x}$ / $(YSZ)_x$ composites with varying x (0.0 to 5%) have been investigated by Xia and his co-workers [24]. Broadening of T_C and shifting of T_{MI} to lower temperatures are observed. But T_{MI}, interestingly decreases up to $x \leq 2\%$ and then it increases. Room temperature MR of the composites is higher compared to pure LSMO at 3T field. Composite of $(LSMO)_{1-x}$ / $(SiO_2)_x$ (where x = 0.0–1.0 mol.%) indicates resistivity rise with increasing x and shifting of T_{MI} towards lower temperatures as observed by Huang *et al*. [25]. In this case the MR behavior of the composites is superior at $T > 150$ K but inferior for $T < 150$ K. MR at 300 K is 21.4% for x = 0.20 but 17.7% for x = 0.0 at 50 kOe field. Spin-polarized tunnelling through the LSMO grains in the presence of the insulating SiO_2 in the grain boundary is ascribed for the observed effect. Another insulating

inert material Al_2O_3, used for the junction MR devices, has been used by Hueso *et al.* [26] to form the composite $(LCMO)_{1-x}(Al_2O_3)_x$ (x = 0.0–25 vol.%). They have observed the MR maximum at the conduction threshold (x = 10%) at 77 K and at 7.5 kOe. $(LSMO)_{1-x}/(MgO)_x$ (x = 0.0–0.5) composites exhibit a pronounced LFMR compared to pure LSMO which is < 1% at $B \leq 1$ kOe at low temperatures. For x = 0.05, MR is 25% at T = 4.2 K, 50 kOe field. Even a small amount of MgO ($x \leq 0.05$) changes the intrinsic metallic bulk electron transport into a grain boundary controlled extrinsic behavior [27]. High field MR (HFMR) is also increased up to 50–60% in the range 4.2–200 K at 50 kOe. In the case of $(LSMO)_x/(SrMeO_3)_{1-x}$ composite [28] (Me = Ti, Zr, x = 20–70 mol.%) the MR enhancement point (x = mol.% LSMO) is dependent on the annealing temperature.

Yan *et al.* [8] have investigated the LFMR of the LSMO/$CoFe_2O_4$ composite for a single composition of 20 wt% $CoFe_2O_4$. The resistivity of the composite is about an order of magnitude larger than that of the same grain-sized pure LSMO. A large LFMR has been obtained in this composite compared to pure LSMO. At 5 kOe, the MR of 20 wt% composite is 10% at 280 K and 5% at 290 K whereas these values for pure LSMO are 2 and 1% respectively. The high resistivity of the composite is attributed to the random scattering of the spin electrons at the surfaces of the magnetic $CoFe_2O_4$ grains. Since the spin-dependent scattering of the conduction electrons at the grain boundaries is highly field sensitive, the magnetic scattering of the polarized charge carriers may be responsible for the LFMR.

Another interesting system with a hard ferromagnetic insulator (HFMI) as the second phase of the composite is reported by Huang *et al.* [29] They have studied $(L_{0.67}Sr_{0.33}MnO_3)_{1-x}$ / $(BaFe_{11.3}(ZnSn)_{0.7}O_{19})x$ (BAM) composites as a function of vol.% (0.0–1.0) of the insulating phase. A resistivity rise with increasing x, indicates a percolative system. But in contrast to the other LFMR / HFMR composite discussed earlier they have reduced LFMR whereas HFMR slopes in the ρ vs H curve are greater. Based on this observation, they suggest that magnetic coupling is not solely responsible for increase in MR at low field, but microstructure also plays an important role to have the desired effect.

For the first time Müller et. al. [30] prepared $(LaSr)MnO_3$ powders with perovskite structure in the basic system MnO_2–SrO–La_2O_3–B_2O_3 by a modified glass crystallization method. The powders show a CMR-effect with a maximum value of 9% at B=1 T at $T \approx$ 380 K typical for high-quality LSMO materials. They have not studied the effect of any nucleating agents on these manganites. The magnetic properties of the powders from borate glasses are comparable with the properties of LSMO single crystals concerning their

magnetization and Curie-temperature [31]. Gupta *et al.* [6] have reported the magnetotransport studies of LSMO–borosilicate glass composites. They have reported an enhanced LFMR of about 1.8% at 200 Oe at room temperature for 25 wt% of glass, the percolation threshold composition for the system. They have further argued that the glass layer, as an amorphous insulator, found in the grain boundaries of the LSMO and acts as a barrier for spin-polarized tunneling thereby enhancing the LFMR. They have also found the sudden resistivity jumps around the percolation threshold. The sharp drop of resistivity in MR vs H curve is attributed to the much-discussed spin-polarized tunneling through the FM grain boundaries whereas the gradual drop thereafter is assigned to the magnetically hard region at the disordered interface. $(LCMO)_{1-x}$ (polyparaphenylene, $PPP)_x$ (x = wt. fraction, 0.0–0.6) composites [7] have been studied by Huang and his group. MR enhances significantly at lower temperatures for the composite, which is 3 times larger than pure LCMO. Similar studies have been carried out by Yan *et al* [32] for the $(LSMO)_{1-x}(PPP)_x$ composites (wt. fraction of PPP, x = 0.0, 0.2, 0.6, 1.0). They have found a remarkable LFMR especially at low temperature and at H < 5 kOe.

The magnetoresistance of $(La_{0.7}Ca_{0.3}MnO_3)_{0.5}/(La_{0.7}Sr_{0.3}MnO_3)_{0.5}$ composite [33] has been investigated as a function of sintering temperature. Raising the sintering temperature triggers the interfacial reaction between LCMO and LSMO which dictates the MR property over a wide temperature range across the room temperature. The coexistence of multiphases at the interface associated with the chemical and magnetic inhomogeneity is the probable cause of the broad MR response across the room temperature as suggested by the authors. Another such composite studied is $(LSMO)_{1-x}$ / $(Sm_{0.7}Sr_{0.3}MnO_3)_x$ (SSMO) [34] with x = 0.0–1.0. Since the transition temperature for SSMO is 63 K, it behaves as a paramagnetic insulator at high temperature and the combination effectively acts as a FM-insulator composite. Maximum MR of 28.3% is obtained at 293 K for x = 0.6 (percolation Threshold) which rises to 46.4% at 200 K for x = 0.7 and at 50 kOe. Composites such as $(LSMO)_{1-x}/(Pr_{0.5}Sr_{0.5}MnO_3)_x$ (PSMO) with x = 0.0–1.0 have been studied by Liu *et al.* [35] and Yuan *et al.*[36]. Resistivity increases and T_{MI} shifts to lower temperatures with increasing x and has been explained in terms of spin-coupling layer inside LSMO grains. Huang et al. [37] studied the microstructural, magnetic and transport properties of $La_{0.7}Sr_{0.3}MnO_3/Nd_{0.7}Sr_{0.3}MnO_3$ (LSMO/NSMO) nanocomposites prepared by a method based on the sol–gel coating of powder. A remarkable enhancement in magnetoresistance as well as LFMR in LSMO/NSMO nanoscaled granular composites is observed. Magnetic measurement shows that the

combination of LSMO with NSMO would lead to a structural disorder and hence an enhanced spin disorder at interfaces and grain boundaries. In this paper, the magnetoresistance effect in the composites is studied based on the tunneling transport model.

A ferromagnetic/metal type composite (LCMO/Ag) has been investigated by Huang *et al.* [38] and a large enhancement in MR near room temperature and a dramatic decrease in resistivity for the composite has been reported. They have observed a shifting of T_{MI} towards T_C in Ag-melted LCMO and suggested magnetic inhomogeneity near the LCMO grain boundaries which are responsible for enhanced MR near room temperature. The magnetic, transport and structural properties of another FM-metallic bulk polycrystalline composites of $La_{0.833}Na_{0.167}MnO_3$ and Ag_2O with molar proportion 1: x(0.0–0.5) has been investigated by Tang *et al.*[20] Observations are much more like that of LCMO/Ag composites. This is because of high temperature sintering of the composites. Ag_2O gets reduced to metallic Ag and gets populated at the grain boundaries of the perovskite manganites. Room temperature MR of the composites improves. Pal et al. [39] also studied the magnetic and transport properties of $La_{0.67}Pb_{0.33}MnO_3$ with the addition of nonmagnetic Ag (0-20 wt%). both resistivity and magnetization decrease with the addition of Ag, particularly for lower concentration of Ag (<10 wt%). Ferromagnetic Curie temperature increases with addition of Ag. Ag added La-Pb-Mn-O composites, both T_p and T_C could be varied over a wide range of temperature with Ag concentrations and small change in resistivity is observed near room temperature which might be important for application point of view.

A tuning between positive and negative MR is observed in $(LSMO)_{1-x}(La_{1.85}Sr_{0.15}CuO_4)x$ (LSCO) (x = wt. fraction, 0.0–0.9) composites [40], a composite between a CMR and a superconducting component. Above the superconducting transition of LSCO all samples show negative MR up to room temperature for $x < 0.5$. But as the applied field increases a positive MR comes into picture for samples with $x > 0.5$ because of the magnetic breakdown of the superconducting coupling within LSCO grains. This magnetic field and composition sensitive competition between the positive and negative MR reveals the coexistence of a ferromagnetic and superconductive ordering in the system that favors the materials to be used as a magnetic field sensitive device like vortex detector. But it limits its applicability to only low temperature because for the superconductive ordering the material must be kept at T below the superconducting transition temperature (TSC) of LSCO.

CMR composite systems involving $La_{0.67}Ca_{0.33}MnO_3$ as the ferromagnetic metallic phase and SiO_2 (insulating refractory oxide) [41], ZnO (a well-known semiconducting

material) [42], SiCN (a conducting polymer-derived ceramic, PDC) [43] and ZrO_2 (an ionic conductor) as the second phase [44] of the composites prepared by citrate gel route [41] were studied. Si being strongly preferred for tetrahedral coordination cannot enter the perovskite lattice. So at best what it can do is either react with LCMO to form another phase or precipitate as SiO_2 or some derivative of this in the grain boundary region. SiCN is conducting, so differs in transport properties from SiO_2. ZnO itself being a semiconducting material should influence the transport properties of conducting LCMO in a different way than the insulating materials like SiO_2 or ZrO_2. ZrO_2 is a well-known ionic conductor. In the polycrystalline bulk synthetic route it is difficult for Zr^{+4} to go into the manganite perovskite lattice (B sites) because of large size mismatch [45]. Moreover Zr^{+4} does not prefer octahedral coordination. Das et.al. [46] synthesized Lu^{3+} substituted $La_{0.67}Ca_{0.33}MnO_3$ (LCMO) by an auto-combustion method. The magnetic and electrical transport properties of the Lu substituted LCMO [$(La_{1-x}Lu_x)_{0.67}Ca_{0.33}MnO_3$ ($0.0 \leq x \leq 0.20$)] system have been investigated and compared with those of the Y^{3+}, Pr^{3+}, Dy^{3+} and Tb^{3+} substituted LCMO systems. The transition temperatures and magnetization decrease as the Lu concentration increases. This is satisfactorily accounted for on the basis of a transition from ferromagnetic at $x = 0$ to canted spin order for $x>0$. All the samples show a higher magnitude of MR compared to that in pure LCMO at 80 kOe field in the temperature range 5–320 K. A fairly high value of low field magnetoresistance (LFMR) of about 30% is obtained in all the samples at a field less than 5 kOe.

2.2 Ni nanoparticles and Ni based ceramic nanocomposites

Ferromagnetic metal nanoparticles have attracted much attention because of their magnetic properties and their applications in building advanced materials as nanoscale building blocks [47, 48]. They form an important class of structural and electronic material for variety of applications in automobiles, information technology, magnetic energy storage and several other disciplines. For these purposes, size and shape-controlled composite nanoparticles with well-defined structure may be favored. When the size of magnetic particles is reduced to a few tens of nanometers, they exhibit a number of different physical properties such as giant magneto resistance, superparamagnetism, large coercivity, decrease in Curie temperature and low saturation magnetization as compared to the corresponding bulk values [49]. A major disadvantage with small particles with large surface area is that they are highly susceptible to surface oxidation. If not controlled, surface oxidation leads to an almost complete oxidation of fine particles. Therefore, ferromagnetic metal nanoparticles are coated

with a thin ceramic surface layer (such as Al_2O_3, ZrO_2, SiO_2, NiO etc.) to minimize oxidation. Being chemically inert, the layer acts as a diffusion barrier and prevents the particle from surface oxidation. In view of the technological importance, the synthesis of magnetic systems with nanoscale dimension has attracted a lot of research attention.

Ferromagnetic nickel (Ni) metal was chosen due to our interest in its magnetic properties as well as its industrial importance. Nickel (Ni) nanoparticles and Ni based-ceramic nanocomposites exhibit interesting magnetic and electrical properties. These properties depend on morphology, size distribution and volume fraction of the metallic Ni nanoparticles [50, 51] in the ceramic matrix. It also depends on the preparation techniques for synthesizing nanoparticles and nanocomposites. Hence, attempts are being made to synthesize nanoparticles with either spontaneous surface oxide or magnetically inert shells in search of new materials with new properties and applications.

The solution precursor method has potential advantage over other methods not only for achieving homogenous mixing of the components on the atomic scale, but also for the possibility of forming desired shapes and sizes which are of technological importance. Other advantages of the these routes are lower processing temperatures, short annealing times, high purity of materials, good control of size and shape of the particles and particle size well below 100nm at low processing temperature. A number of methods such as hydrazine reduction in ethylene glycol [52], sonochemical methods [6], microemulsion techniques [8] and alcohol reduction [53] have been developed for preparation of metal nanoparticles. The reduction of metal ions by a reducing agent ($NaBH_4$) is a useful method for the production of nanoparticles of metals. Change in reaction conditions or mixing procedures can lead to different products, variable yields, and many complications that are still not understood. This process yields boride or mixture of metal and boride under certain reaction conditions. Legrand et al. [54] attempted to synthesize Ni nanoparticles by chemical reduction using $NaBH_4$ in air and they found a mixture of Ni and Ni-B in the reaction product. On the other hand, Glavee et al. [55] reported the formation of both Ni and NiO when the reaction was carried out in aqueous medium using $NaBH_4$.

The magnetic properties of nanoparticles of Ni metal are different from the bulk Ni value as seen from the literature. The saturation magnetization (M_s) and coercivity (H_c) of the bulk Ni at 300 K are about 55 emu/g and 100 Oe respectively [56]. Wu et al. [52] synthesized Ni nanoparticles with a mean diameter of 9.2 nm by using hydrazine reduction of nickel chloride in ethylene glycol. The saturation magnetization (M_s) and coercivity (H_c) was found

to be 22 emu/g and 0.1 Oe respectively. The decrease in M_s might be due to the decrease in particle size or presence of amorphous and nonmagnetic or weakly magnetic phase at grain boundary. A protective layer of ethylene glycol might have formed on the particle surface which causes a decrease in saturation magnetization. The H_c value of nickel nanoparticles was not only lower than that of bulk nickel but also almost equal to zero. Schaefer et al. [48] investigated the ferromagnetic properties of compaction prepared nanocrystalline Ni (crystallite size 10 nm) in order to study the correlation between the disordered interfacial structure and macroscopic properties. It was observed that the magnetic moment of the atoms in the interfaces is decreased to 0.34 μ_B/atom (0.6 μ_B/atom in bulk Ni) and the Curie temperature is 545 K for the interfacial component, lower than the value 630 K for the Ni bulk crystal. These results are discussed based on disordered structure of interfaces. Broto et al. [57] studied the magnetization behavior of two types of particles of different sizes prepared using chemical route under an inert atmosphere. The sample containing the larger grains (30 nm) exhibits a classical ferromagnetic behavior whereas a superparamagnetic behavior is observed for the finest grains (4 nm) in the whole temperature range (4 - 77K). Zhang et al. [58] achieved the size-controlled synthesis of nickel nanocrystals (20 – 60 nm) by the decomposition of nickel acetylacetone in oleylamine under flowing nitrogen gas through three different processes: direct thermolysis, hot injection, and seed-assisted process. The magnetic measurements showed that Ni samples are still ferromagnetic, and that their saturation magnetization and coercivity are size dependent. Magnetic measurement revealed that smaller nanocrystals had higher coercivity and smaller saturation magnetization, reflecting the size effect of nanocrystals.

Magnetic nanocomposites comprised of nano-sized magnetic crystals embedded in an amorphous or crystalline matrix have been shown to have excellent soft magnetic properties. Ceramic-based composites containing nano-sized metal inclusions exhibit several advantageous magnetic properties. Jung et al. [59] studied the magnetic behavior of Ni nanoparticles in an MCM mesoporous material. In this work, an aluminosilicate with the MCM-41 (porous amorphous silica material with a hexagonal honeycomb structure) was used as a host for synthesis of nickel metal nanoparticles (1-2 nm). Initially, ion exchange in aqueous solutions allows the introduction of nickel cations into AIMCM-41, and then reduction with sodium borohydride produces nanometer sized nickel particles. Due to the large channel diameters, the MCM-41 hosts are excellent candidates for nanosized magnetic materials. The magnetization as a function of field obtained at 10 K and 20 K, show no

hysteresis and two curves are superimpose whereas the magnetization curves show a significant hysteresis below 5 K. This magnetic behavior confirms the superparamagnetism of the nanocomposite system with a blocking temperature (T_b) of 5 K. González et al. [60] studied the magnetic behavior of Ni nanoparticles in the range of 1-20 nm (with a controlled size and distribution) embedded in a silica xerogel. An inorganic matrix like glasses or SiO_2 xerogels is a good host for crystalline metallic nanoparticles in which we tailor the size and dispersion. Their magnetic behavior is superparamagnetic at 300 K. Three samples were prepared to study the magnetic behavior. For samples A and B which have similar average size and distributions but differ only in the interparticle distances (larger in A than in B), the blocking temperature is higher for B than for A. By comparison, the blocking temperature is similar for samples C and B even though the particle size is smaller for C. This may be due to the ratio of the interparticle distances to the average diameter of the particles being similar for the two samples. Aharon et al. [61] studied the magnetic properties of alumina – nickel nanocomposites (8.7 wt % Ni) produced by infiltration of alumina perform with a nickel-nitrate solution, followed by reduction and sintering. The nanocomposite (most of the Ni particles are in 150 – 200 nm range) exhibits a ferromagnetic behavior; a hysteresis loop with saturation magnetization of 38.9 emu/g and a coercive field of 46 Oe. Large internal stresses in the Ni particles are the main cause for a high coercive field, one order of magnitude larger than for monolithic nickel. Metal / ceramic composite (cermet) acting as a mixed conductor of electrons and oxide ions forms an advantageous anode material of solid oxide fuel cells (SOFC) and temperature and flow sensor applications [62]. The following candidate cermet materials have been proposed: Ni/Y_2O_3-stabilized ZrO_2 (YSZ) [63], Ru/Sm-doped ceria (SDC) [64] Ni/CeO_2 [65], Ni/Gd-doped ceria (GDC) [66]. The electrical properties of the cermet depend on its microstructure of Ni particles in the Ni/YSZ cermet. Different techniques have been developed for preparation of Ni / ZrO_2 cermet. Ni based Ceramic composites exhibiting a broad range of magnetic characteristics are also required for advances in magnetoresistive (MR) sensors [67], magnetic recording and magnetic storage devices [68].

For the electromagnetic device applications, researchers have long been searching for soft-magnetic materials with high saturation magnetization, high permeability, and low energy loss. Ni and its composites are good soft-magnetic materials with both high permeability and low coercivity. But due to their metallic characteristics, the eddy current generation severely limits their applications at high frequencies. It is therefore expected that one may obtain high permeability at high frequencies in magnetic nanocomposite by coating an insulating layer on

the surface. Nanoparticles of transition metals have a great affinity to oxygen, and even spontaneously ignite in air. Therefore, their applications are limited. Coating may provide a protective layer surrounding a magnetic core suitable for enhancing the resistance of core materials to oxidation. Therefore, the process of coating not only provides effective encapsulation of individual nanoparticles, but also controls the growth in size thus yielding a narrow size distribution. Tang et al. [69] report a simple sol–gel combined hydrogen reduction method that is effective and controllable to coat Ni nanoparticles with silica shells. The magnetization of Ni / SiO_2 nanocomposites depends upon the reduction temperature, SiO_2 / Ni ratio and size of the Ni core. The particles treated at higher temperature have a smaller nickel oxide core and exhibit higher magnetization, because nickel oxide has lower magnetization than nickel. Sun et al. [70] discussed magnetic properties of Ni-Ce nanocomposite particles (15 – 50 nm) with NiCe alloy and NiO shell layer. Microstructural analysis showed that microstructural defects exist in large Ni core zone (10–45 nm); the shell layers (3–5 nm) are consisted of innermost NiCe alloy and outermost NiO oxide. Superparamagnetic behavior above average blocking temperature (T_b) 170 K was exhibited; this superparamagnetic relaxation behavior was found to be modified by interparticle interactions, which depend on the applied field and size distribution. In addition, antiferromagnetic order occurred with a Neél temperature T_N = 5 - 11 K. This can be attributed to the appearance of magnetic ordering of Ce ions in the shell layer of Ni–Ce nanocomposite particles. Roy et al. [71, 72] studied the structure and magnetic properties of fine Ni nanoparticles (~ 65 nm diameter with a tetragonal crystal structure) having a spontaneous surface oxide layer. The particles were prepared by the chemical reduction of nickel ions in an aqueous medium, with sodium borohydride as the reducing agent. The M-H loops of the samples show a clear hysteretic behavior but do not saturate, thereby suggesting the existence of both ferromagnetic and paramagnetic components in the magnetization. The magnetization results have been analyzed in correlation with X-ray diffraction and microstructure and satisfactorily explained based on a core-shell model, where each particle as a magnetically heterogeneous system consisting of a ferromagnetic core of Ni and an antiferromagnetic/paramagnetic shell of NiO.

2.3 Summary of literature

The perovskite structure manganites, specifically LCMO and LSMO have been extensively studied due to the simultaneous presence of magnetic and electrical transitions in certain composition ranges. They exhibits colossal magnetoresistance behavior whcih is of interest to magnetic information storage applications. The magnitude of MR which depends

on the amount of external magnetic field applied becomes colossal only at larger fields. The temeprature at which the transitions occur depend critically on the chemical composition. Hence it is found from literature that; to enhance the magnitude of MR at low fields and relatively high temperatures doping, creation of high density of disordered areas such as grain boundaries and distribution of the perovskite manganite in different matrices have been used as attractive approaches.

In the case of metal nanoparticles synthesis, the major problem is oxidation of particles and instability to control the size and shape of the particles. Various techniques such as vapor phase condensation, mechanical attrition, aqueous state reduction and distribution of metal particles in a matrix phase have been used earlier. Another major area of research has been investigation of physical properties such as magnetic behavior and transport in reduced demisionality systems. This helps in tunning the physical properties using physical sizes as the control parameter.

2.4 Objective of the present studies

The main objectives of present studies are:

Synthesis of composite materials consisting of magnetic nanoparticles dispersed in a magnetic or a nonmagnetic insulating matrix and studying their transport and magnetic properties.

The three methods used for the synthesis of nanocomposites are; (a) microwave refluxing, (b) glass-ceramic and (c) aqueous reduction. The first two techniques are used to synthesize nanocrystalline LCMO and nanocomposite of LCMO while the last technique, aqueous state reduction is used to synthesize metal-ceramic nanocomposites. These techniques are known to result in the production of nanocrystalline materials. Also, they promote formation of composites at the nano level, which is one of the primary aims of this thesis. These techniques are highly versatile and can be used for the synthesis of a wide variety of materials. Moreover, synthesis of nanocomposites using these techniques has not been investigated in detail earlier and this forms the objective in using these techniques. In conclusion, it can be mentioned that the three different techniques used are more general in nature and can be used to synthesize a host of different materials. The materials system chosen LCMO, LCMO in Ni-ferrite, LCMO in SiO_2 matrix with nucleating agents, and Ni/NiO or Ni/ZrO_2 are of current topical interest in magnetic materials.

Chapter 3

EXPERIMENTAL WORK

3.1 Introduction

Magnetic – magnetic, magnetic – nonmagnetic and metal – ceramic nanocomposites have been prepared using different techniques such as microwave refluxing, glass-ceramic and chemical reduction routes respectively. Several different characterization techniques have been used to study the properties of these nanocomposite materials. In this chapter, the synthesis and characterization techniques are described in detail.

3.2 Synthesis techniques

3.2.1 Microwave refluxing

Microwaves generally have a frequency between the radio and infrared frequencies of the electromagnet spectrum and occupy a range 0.3 to 300 GHz, corresponding to wavelength of 1 meter to 1 mm. Microwave Ovens, which work at 2.45 GHz frequency and at power levels of about a kW, are in wide use. In microwave heating, unlike conventional heating, heat is generated internally within the material instead of originating from external sources. As a result of internal and volumetric heating, thermal gradients and direction of heat flow in microwave heated materials can be just the opposite of those in conventional methods**.** Fig. 3.1 shows the difference between conventional and microwave-heating methods. It offers a clean, cheap and convenient method of heating often resulting in higher yields and shorter reaction times. [73]

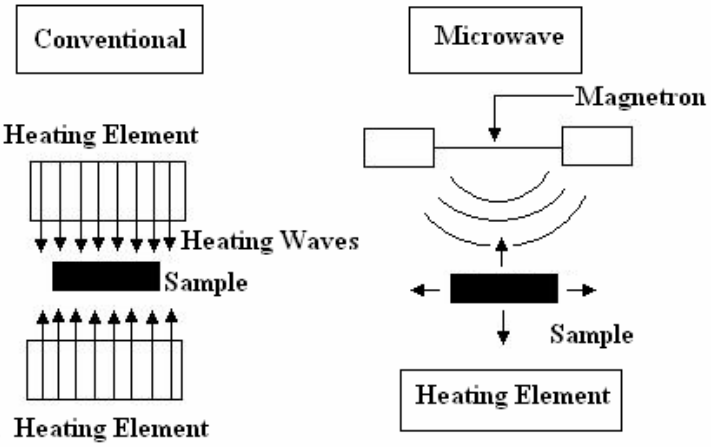

Fig. 3.1: Principle of Conventional and Microwave heating methods [Adapted from Ref 73]

The microwave oven was modified by introducing a refluxing system [74]. The refluxing system contains a round bottomed flask with a water condenser. The experimental details of LCMO nanoparticles and LCMO: NF nanocomposites synthesis by microwave refluxing technique are discussed in experimental section of chapter 4.

3.2.2 Glass-ceramic

LCMO: SiO_2 nanocomposites have been prepared by glass-ceramic process with and without nucleating agents. In this case, the initial raw materials were melted in an alumina crucible. After melting, the molten mass was quenched between two steel plates to form amorphous flakes of the composite. The quenched flakes were powdered and etched with hot acetic acid to remove the borate-containing phase in the composites. The compositions and heat-treatment schedule can control the growth and size distribution of LCMO phase. The experimental details of LCMO: SiO_2 nanocomposites synthesis by glass-ceramic process are discussed in experimental section of chapter 5.

3.2.3 Chemical reduction

Microstructural evolution of metallic Ni nanoparticles and Ni: NiO/ZrO_2 nanocomposites during chemical reduction was studied. These composites have been synthesized by the reduction of aqueous solution of metal salts using $NaBH_4$ as reducing agent. After the reaction, the colloidal solution obtained was centrifuged for several times to remove the borate containing phases. The centrifuged products were dried and heat-treated at different temperatures in air or H_2 atmosphere. The experimental details of Ni nanoparticles and Ni: NiO/ZrO_2 nanocomposites synthesis by chemical reduction process are discussed in experimental section of chapter 6.

3.3 General characterization

3.3.1 X-ray diffraction

Phase formation in different systems was studied using the room temperature powder X-ray diffraction (Cu-Kα radiation) performed with a Phillips X'pert Diffractometer (model: PW 3040/60). Samples are scanned in a continuous mode from 15° – 100° with a scanning rate of 0.02 (degree) / 15 (sec). A Reitveld structural refinement procedure was used to analyze the diffraction patterns using Full Proof software.

The Rietveld method [75] is a powerful technique to extract detailed structural information from powder diffraction data. In contrast to the conventional profile fitting, this method does not use integrated intensities of reflections but employs the entire powder diffraction pattern. In this method, each data point in the digitized intensity versus 2θ curve is an independent observation and during refinement, structure parameters, background parameters and profile parameters are varied in a least squares procedure until the simulated pattern matches well with observed pattern for the proposed structure model [76].

3.3.2 Transmission Electron Microscopy (TEM)

The grain size, particle size and shape were studied in Transmission Electron Microscope (TEM) (model: CM 200, Phillips). For preparation of TEM sample, the powder is dispersed in isopropyl alcohol in a ultra sonication bath (20 kHz, 500 W) for half an hour. One drop of the well-dispersed sample solution is deposited on to a carbon coated copper grid (400 mesh). The dried grid was used for microscopy.

3.3.3 Determination of Mn^{3+} and Mn^{+4} ion concentration in the samples by Iodometric titration method

Principles involved

In presence of concentrated hydrochloric acid (HCl), Mn^{3+} and Mn^{4+} (which is present in the samples) gets reduced to Mn^{2+} and chlorine is produced as per the following reaction,

$$2\ Mn^{3+} + 2\ Cl^{1-} \rightarrow Cl_2 + 2\ Mn^{2+} \qquad 3.1$$

$$2\ Mn^{4+} + 2\ Cl^{1-} \rightarrow Cl_2 + Mn^{2+} \qquad 3.2$$

The in situ generated chlorine reacts with the iodide and iodine is formed:

$$Cl_2 + 2\ I^{1-} \rightarrow 2\ Cl^{1-} + I_2 \qquad 3.3$$

This iodine is titrated with a standard volumetric solution of sodium thiosulphate ($Na_2S_2O_3$) until a clear and colorless solution is obtained. The reaction involved is as follows.

$$2\ S_2O_3^{2-} + I_2 \rightarrow 2I^{1-} + S_4O_6^{2-} \qquad 3.4$$

From the known volume and strength of the thiosulphate solution Mn^{3+} and Mn^{4+} percentage were calculated.

Procedure

The iodometry method used is described in Vogel [77]. Weighed quantity of potassium dichromate ($K_2Cr_2O_7$) was taken in a 500 cc volumetric flask and was dissolved in distilled water. Finally the volume was made upto the mark. Weighed quantity of sodium thiosulphate ($Na_2S_2O_3$) was taken in a 500 cc volumetric flask and was dissolved in distilled water. The volume was made upto the mark. The solution was finally transferred in a 500 cc amber colored bottle and was kept in a dark place. Weighed quantity of potassium iodide (KI) was taken in a beaker and was dissolved in distilled water to make it strength of 10 % w/v. Finally, the solution was kept in a 500 cc amber colored bottle and the bottle was kept in a dark place.

Since $Na_2S_2O_3$ is a secondary standard, it was titrated with a standard $K_2Cr_2O_7$ solution to final out its actual strength. In order to do that 20 ml $K_2Cr_2O_7$ was taken in a 250 cc Stoppard conical flask. 10 ml 10% KI solution and 3 ml concentrated HCl was added to it and the whole mixture was kept in a dark place for 15 minutes with occasional stirring. After 15 minutes the lid and the inside wall of the conical flask was rinsed with distilled water to take the liberated I_2 into the solution and whole mixture was titrated with $Na_2S_2O_3$ taken in burette. When the end point was approached three drops of 1 % (w/v) freshly prepared starch solution were added in order to observe the color change better. Finally, the end point reached from blue violet to a colorless solution just with one drop of $Na_2S_2O_3$. The volume of $Na_2S_2O_3$ (V_2) was noted. The strength of $Na_2S_2O_3$ (S_2) was calculated as follows.

$$V_1S_1 = V_2S_2 \qquad 3.5$$

Where, V_1 is the volume of $K_2Cr_2O_7$ taken = 20 ml

S_1 is the strength of the $K_2Cr_2O_7$ solution = 0.02 (N)

V_2 is the volume of $Na_2S_2O_3$ required to titrate 20 ml standard $K_2Cr_2O_7$ solution

A weighed amount of the sample powders was dissolved in a stirred mixture of 8 – 9 ml 10 % KI solution and 2.5 ml concentrated HCl in a 250 cc stopper conical flask. The conical was kept in a dark place for 20 minutes with occasional stirring. After 20 minutes the

lid and the inside wall of the conical flask was rinsed with distilled water to take the liberated I_2 into the solution and whole mixture was titrated with $Na_2S_2O_3$ taken in burette. When the end point was approached three drops of 1 % (w/v) freshly prepared starch solution were added in order to observe the color change better. Finally, the end point reached from blue violet to colorless solution just with one drop of $Na_2S_2O_3$. The volume of $Na_2S_2O_3$ was noted. From the known volume and strength of $Na_2S_2O_3$ solution, Mn^{+4} was calculated as follows.

In order to calculate the Mn^{3+} and Mn^{4+} weight percentage three assumptions were made, (i) La and Ca maintain the initial stoichiometric ratio 2:1, (ii) La and Ca have oxidation state of 3+ and 2+ respectively, and (iii) Mn can be present in oxidation states of 3+ and 4+.
If x be the moles of Mn present in the sample and y [= ($V_{thiosulphate}$× $S_{thiosulphate}$)/1000] be the moles of total Mn^{3+} and Mn^{4+} titrated for the sample, then the fraction of total (Mn^{3+} + Mn^{4+}) to total Mn present in the system = y/x. If all the Mn is present in the system as Mn^{3+}, then y/x should be equal to 1. So the excess amount, [(y/x)-1]× 100 (= z say) is the amount of Mn^{4+} present in the sample and the amount of Mn^{3+} is (100 – z). So from the known volume ($V_{thiosulphate}$) and strength ($S_{thiosulphate}$) of the thiosulphate solution, required to titrate the sample solution, Mn^{3+} and Mn^{4+} concentration is calculated.

3.3.4 Thermogravimetric analysis (TGA)

Thermogravimetrical (TG) measurements of the as prepared LCMO sample (synthesized by microwave refluxing) are performed using Thermowaage L 81 (Germany) up to 1173 K in atmospheric air. The heating rate was in the range of 5-10 K/min. Weight loss of the sample in the heating process is recorded. The difference in weight measured at different temperatures is considered as an estimate of the content of volatile / decomposable molecules.

3.3.5 Electrical transport and magnetoresistance

The temperature dependence of electrical resistivity ρ(T) of samples was measured by standard four-probe dc technique in the temperature range 20 – 300 K. A closed cycle refrigerator and Si-diode sensor have been used for cooling the sample and monitoring the temperature, respectively. Magneto-resistivity measurements have been carried out on the same samples from 300 to 80 K using a liquid N_2 gas-flow cryostat. An electromagnet was used to produce the magnetic field of 0.85 Tesla. In the presence of field, the temperature was monitored using a Pt sensor. The samples were mounted on a sample holder with the help of

G-burnish, a low temperature epoxy. The electrical contacts of the current and voltage lid of the samples with the probes were made by means of good quality Ag paint. The samples were dried under an IR lamp to ensure proper contacts. The entire measurement system, comprising of a 181 Keithley nanovoltmeter, a 1271 Datron multimeter, a 224 Keithley current source and a 330 auto tuning Lakeshore temperature controller, was interfaced with a PC for automatic data acquisition.

3.3.6 Magnetization

3.3.6.1 Vibrating sample magnetometer (VSM)

The principle of VSM is the measurement of the electromotive force induced by magnetic sample when it is vibrated at a constant frequency in the presence of a static and uniform magnetic field. The magnetic measurement of sample in the temperature range from ambient temperature upto 1100 K is done by VSM (Lake Shore, Model-7410) in our laboratory. A small part of the pellet (10-40 mg) is weighed and make tight to avoid movements inside the sample holder. High temperature magnetic measurement is performed by flowing an inert gas (argon) into the sample chamber.

The VSM is operated up to 3 T at a vibration frequency of 82 Hz. It is calibrated in magnetic moment and sample temperature. The magnetic moment calibration is carried out using a Ni standard (sphere) with known magnetization (Ms=6.92 emu at 5 kOe). The temperature calibration is performed using a Ni standard having a Curie temperature of 627 K.

3.3.6.2 SQUID magnetometer

The low temperature as well as room temperature magnetization measurement was performed using a SQUID Magnetometer (Quantum Design) MPMS-XL7 at Tata Institute of Fundamental Research, TIFR, Mumbai.

The procedure for zero field cooled (ZFC) and field cooled (FC) measurement is as follows. The sample is cooled initially to low temperature in the absence of magnetic field. At low temperature, the field is applied and measurement is performed upto room temperature. This is called Zero field cooled (ZFC). Again, the sample is cooled in the presence of that magnetic field from room temperature to low temperature and data was taken. This is called Field cooled (FC). The Curie temperatures (T_C) are estimated from the plot Magnetization (emu/g) vs. Temperature (K), by extrapolation of linear sections of M (T) up to the intersection with T-axis or from the dM / dT plot.

3.3.7 Particle size measurement

There are number of particle sizes that arise depending on the measuring technique discussed below.

Physical size (D_P): This refers to the true size of the particles and is usually obtained with transmission electron microscopy (TEM).

Hydrodynamic size (d_h) and polydispersity: The hydrodynamic size of a particle is usually determined using photon correlation spectroscopy (PCS). This indicates the diameter of a particle including the fluid molecules around the electrostatic double layer.

The measurement is done by PCS using Zeta Plus (Brookhaven Instrument Corporation, USA). The size and polydispersity is analyzed by Zeta plus Software. In this technique, random intensity fluctuations arising from the Brownian motion of colloidal particles are analyzed by autocorrelation to give either a simple mean size or polydispersity (distribution width) or more complete distribution data even for multimodal distributions. For measurement of size and polydispersity, adequate diluted samples are taken in a clean plastic cuvette and put into the sample holder. Temperature, medium of suspension, number of runs and duration of each run are specified before running of the samples. The data are taken accordingly.

Crystallite size (D_X): The size corresponds to the mean value of the crystalline domain size of the particles is determined from the X-ray line broadening using Scherrer formula with correction factor as given below,

$$D_x = \frac{0.9\lambda}{\beta \cos\theta} \qquad 3.6$$

Where D_X is average crystalline size, λ is the X-ray wavelength used, β the angular line width of half maximum intensity and θ the Bragg's angle in degree.

RESULTS AND DISCUSSION

Chapter 4

Magnetic – Magnetic Nanocomposite

This chapter describes the synthesis and characterization of CMR, $La_{0.67}Ca_{0.33}MnO_3$ (LCMO) nanoparticles and their distribution in a magnetic, insulating $NiFe_2O_4$ (NF) matrix.

4.1 Structural, transport and magnetic studies of LCMO nanoparticles prepared using microwave refluxing process

4.1.1 Introduction

The manganites ABO_3 exhibit a wide variety of magnetic, ferromagnetic to paramagnetic, and electrical, insulating to metallic, behaviors depending on the composition and temperature. The different methods used for enhancing the colossal magnetoresistance (CMR) property are substitution either in A or B site [27], grain size reduction [26], and distribution of the manganite grains in a non-magnetic or magnetic insulating matrix [32]. Hence, in the present work, the effect of grain size reduction and/or distribution in a magnetic insulating matrix on the CMR property in manganites has been studied in detail.

Nanocrystalline $La_{0.67}Ca_{0.33}MnO_3$ (LCMO) material has been prepared from organic precursor solutions with different pH and annealed at different temperatures to study their effect on structure, transport and magnetic behavior.

4.1.2 Experimental details

The $La_{0.67}Ca_{0.33}MnO_3$ (LCMO) powder was prepared by a combination of soft chemistry and microwave refluxing from organic precursors. The flow chart used for the preparation of $La_{0.67}Ca_{0.33}MnO_3$ (LCMO) manganite nanopowders is shown in Fig. 4.1. Stoichiometric equivalents of La-acetate, Ca-acetate and Mn-acetate were mixed with ethylene glycol and this mixture is used as a precursor. This precursor solution was kept at 353 K under constant stirring condition. The solution was found to be slightly acidic with a pH of ~ 5.8 and also turbid. The pH of this acidic precursor solution was increased by addition of KOH solution. The initially turbid solution becomes clear at a pH of ~ 10.5 indicating the dissolution of the precursors. Increasing the pH to 11.5 reduces the clarity and induces cloudiness due to gel formation. Gel formation increases with increasing pH and the pH was increased up to 12.5 in the present work. Hence three precursor solutions with pH of 10.5, 11.5 and 12.5 corresponding to clear solution, start of gel formation and gelation respectively were taken for further processing by microwave refluxing. A commercial microwave generator operating at 2.5 GHz and 980 Watts was used to heat the precursor solution to > 473 K, boiling point of ethylene glycol. This was later condensed by refluxing with circulating water and recycled. The solution was subjected to microwave heating and refluxing for a period of 1hour and the precipitate obtained was washed thoroughly with distilled water for

15-20 times, each time separating the precipitate by centrifuging at 4000 rpm. The precipitate was dried and calcined at 973 K for 1hour. The calcined powder was pelletized and annealing was done at three different temperatures (973 K for 1hour, 1123 K for 30 minutes and 1473 K for 4hours). Structural, transport and magnetic properties of these annealed samples have been studied in detail.

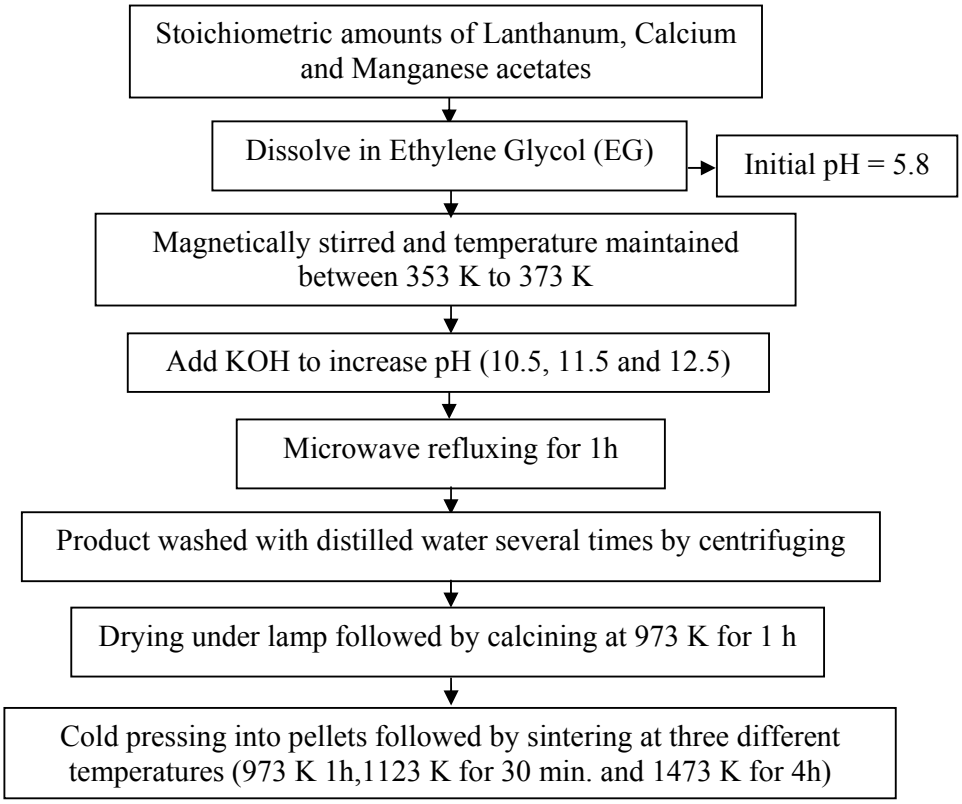

Fig. 4.1: Schematic flow chart for preparation of nanograined $La_{0.67}Ca_{0.33}MnO_3$ (LCMO) system

The structural analysis was performed using a combination of x-ray diffraction with Rietveld analysis and TEM. Thermal analysis was performed by Thermal Gravimetric Analysis (TGA). The chemical composition of LCMO, defined in terms of Mn^{4+} content, prepared from different precursor solutions and annealed at different temperatures was determined by iodometric titration technique [77]. An external magnetic field of 0.85T was used to determine the magnetoresistance as a function of temperature. The magnetic behavior was studied using vibrating sample magnetometer (VSM, LakeShore).

4.1.3 Results and discussion

Thermal Gravimetric Analysis (TGA) was done to determine the calcination temperature of the as prepared powders. TGA was performed up to 1173 K at a rate of 10 K/min. Fig. 4.2 shows the weight loss as a function of temperature of the as prepared LCMO powders prepared using microwave refluxing technique. Three distinct regions (< 500 K, 500 K to 850 K and 980 K) of weight loss are observed. The weight loss around 973 K is observed to saturate compared to other regions. Hence, 973 K is chosen as the minimum calcination temperature for these LCMO powders. After calcination at 973 K for 1 hour, these samples were annealed at three different temperatures (973 K for 1hour, 1123 K for 30 minutes and 1473 K for 4hours) to study their structural, electrical and magnetic properties.

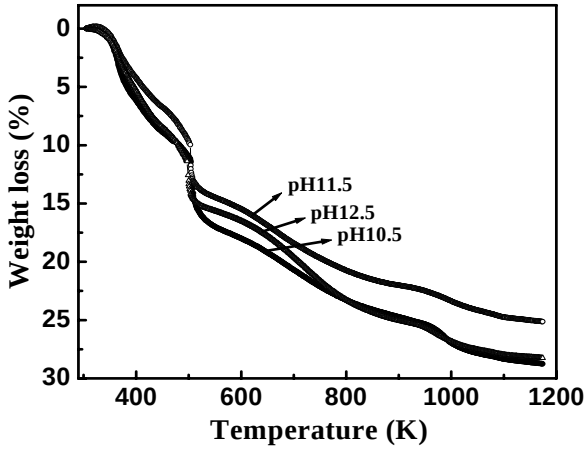

Fig. 4.2: Weight loss as a function of temperature of the as prepared LCMO powders

4.1.3.1 Structure and microstructure

The presence of various phases and crystallite size were determined from the X-ray diffraction pattern. Figs. 4.3 (a), (b) and (c) show the X-ray diffraction pattern of LCMO annealed at 973 K, 1123 K and 1473 K respectively. The peaks are at identical positions in all the cases. All peaks of sample annealed at 973 K and 1123 K are indexed with orthorhombic form where as the sample annealed at 1473 K is indexed with monoclinic form of LCMO. The transformation of orthorhombic (higher symmetry) to monoclinic (lower symmetry) form may be due to decrease of Mn^{4+} concentration which is a strong function of pH and heat treatment temperature [78]. A Rietveld refinement of orthorhombic and monoclinic form of LCMO is performed based on Pnma and I2/a space group respectively, to determine the lattice parameter accurately. The crystallite size of LCMO is calculated using the Debye Scherrer relation and is given in Table 4.1. The crystallite size of LCMO does not vary when the

temperature increases from 973 K to 1123 K. However, it increases when the temperature increases to 1473 K.

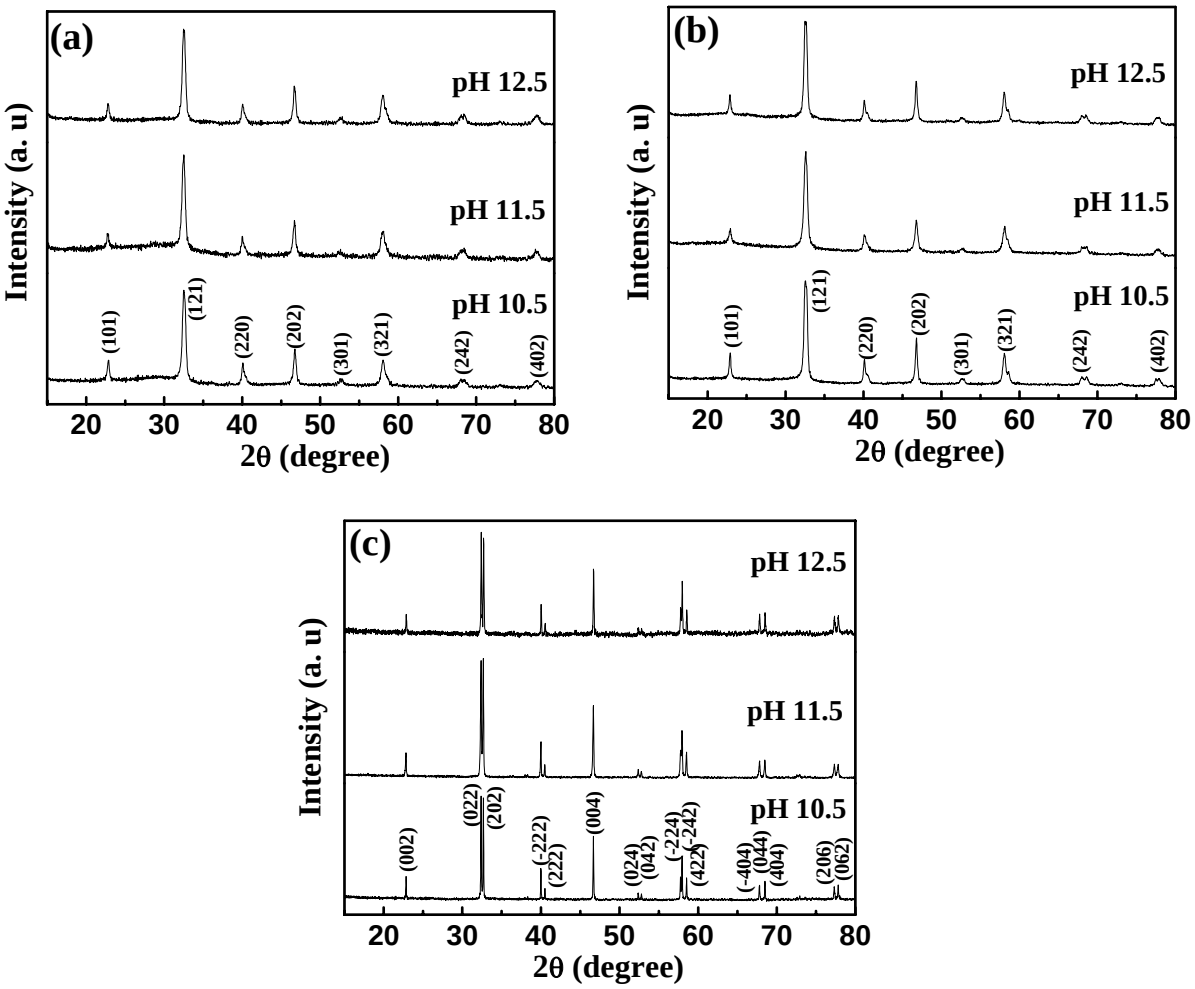

Fig. 4.3: X-ray diffraction patterns of LCMO sintered at (a) 973 K, (b) 1123 K and (c) 1473 K.

Fig. 4.4 (a), (b) and (c) show the Rietveld analysis fit for the most intense peak of LCMO prepared from 11.5 pH precursor and annealed at 973 K, 1123 K and 1473 K respectively. For sample annealed at 973 K and 1123 K, a Rietveld refinement is performed based on Pnma space group of orthorhombic form of LCMO. The lattice parameters (a, b and c) are found to increase slightly as the annealing temperature increases from 973 K to 1123 K. The lattice parameters of these samples are in close agreement with the lattice parameters of bulk LCMO indicating the formation of near equilibrium phase in the microwave-assisted synthesis with no lattice distortions. As the temperature increases to 1473 K, the orthorhombic

form of LCMO changes to monoclinic form. The Rietveld refinement is performed based on I2/a space group of monoclinic phase of LCMO. The unit cell parameters obtained from the Rietveld refinement of all the LCMO samples are given in Table 4.1.

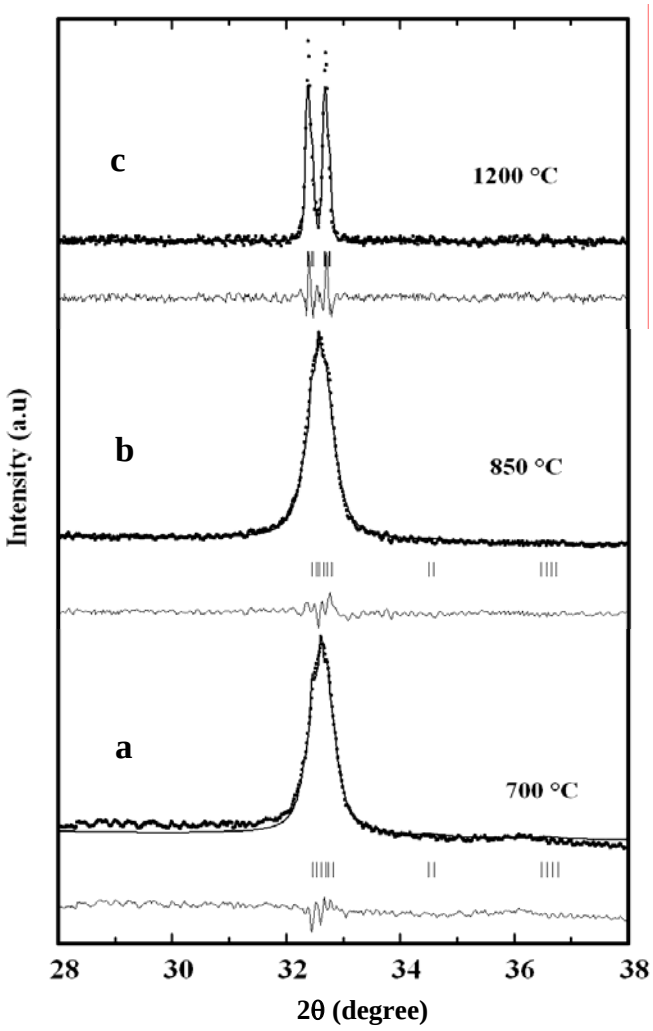

Fig. 4.4: Rietveld analysis of the most intense peak of pH 11.5, LCMO sintered at (a) 973 K (b) 1123 K and (c) 1473 K.

The average particle size of these annealed LCMO samples is also determined by TEM and is given in Table 4.1. Fig. 4.5 (a), (b) and (c) show the TEM micrographs of LCMO annealed at 973 K, 1123 K and 1473 K respectively. From the TEM micrographs, the average particle size is found to be 30 - 70 nm for the samples annealed at both 973 K and 1123 K. The particle size of these two samples is nearly same and it is independent of the annealing temperature, duration and pH of the precursor solution indicating a strong resistance to crystal growth even at elevated temperatures. As the temperature increases to 1473 K, the particle size grows and increases to 200 – 500 nm range as seen in Fig. 4.5 (c).

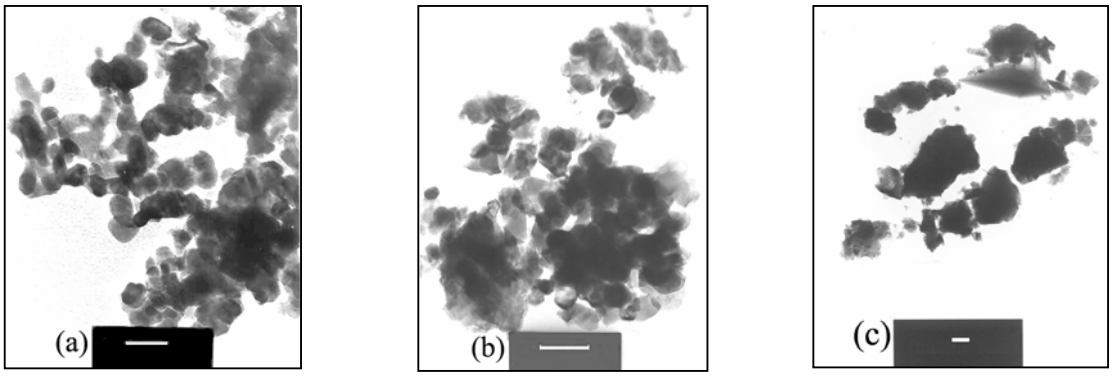

Fig. 4.5: Transmission electron micrographs of LCMO powders annealed at (a) 973 K, (b) 1123 K and (c) 1473 K. Scale corresponds to 100 nm in all cases.

4.1.3.2 Chemical analysis

The concentration of Mn^{4+} in the LCMO affects the transport and magnetic properties of the manganite and hence it was determined by iodometric titration [77]. Mn^{4+} concentration is a strong function of pH and heat-treatment schedule. The Mn^{4+} concentration obtained by iodometric titration of LCMO samples prepared from different pH precursors and sintered at different temperatures is given in Table 4.1. Fig. 4.6 shows the Mn^{4+} concentration of all the sintered samples. The results indicate that Mn^{4+} concentration is highest for a precursor solution with pH of 11.5 in all the cases, sintered at 973 K, 1123 K and 1473 K and lowest for a pH of 10.5. In case of the sample sintered at 1473 K, the Mn^{4+} concentration for all pH values is less compared to others. Decrease of Mn^{4+} concentration leads to a simultaneous deficiency of Ca ion in LCMO. This decrease in Ca^{2+} concentration leads to a congruent change in crystal structure from orthorhombic to monoclinic form [79]. The XRD pattern shown in Fig. 4.3 confirms this crystallographic transformation.

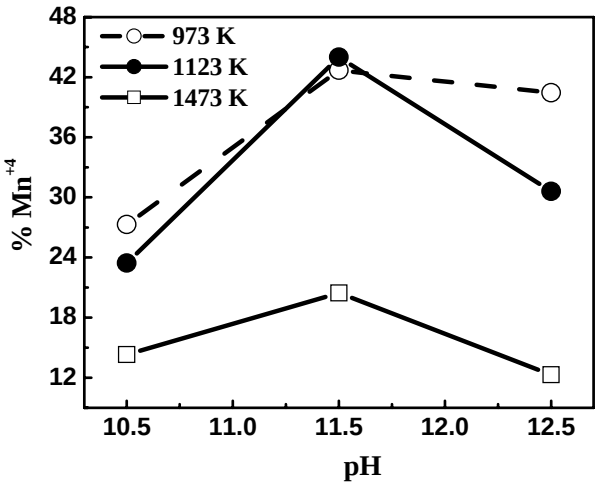

Fig. 4.6: The Mn^{4+} concentration varies as a function of pH of the precursor solution and sintering temperature.

Table 4.1: Phases present and size obtained from XRD as well as TEM for all LCMO samples. The unit cell parameters (a, b and c are the three unit cell length) obtained by Rietveld refinement from the XRD patterns. Percentage of Mn^{4+} in LCMO sample obtained from iodometric titration is also given.

973 K	Phases and structure	Lattice parameters, Å 'a'	'b'	'c'	Angle 'β'	Crystallite size (nm) from XRD	Particle size (nm) from TEM	% Mn^{+4}
pH 10.5	LCMO (O)	5.508(6)	7.762(1)	5.461(3)	---	16	30 - 70	27.3
pH 11.5	LCMO (O)	5.512(3)	7.755(7)	5.464(9)	---	18		42.7
pH 12.5	LCMO (O)	5.506(9)	7.763(7)	5.463(1)	---	17		40.5
1123 K								
pH 10.5	LCMO (O)	5.515(7)	7.776(2)	5.472(8)	---	18	30 - 70	23.5
pH 11.5	LCMO (O)	5.513(1)	7.771(2)	5.471(1)	---	18		44
pH 12.5	LCMO (O)	5.516(9)	7.775(3)	5.471(3)	---	19		30.6
1473 K								
pH 10.5	LCMO (m)	7.780(7)	5.522(6)	5.473(1)	89.29	75	200 - 500	14.3
pH 11.5	LCMO (m)	7.784(8)	5.520(2)	5.479(3)	89.25	78		20.5
pH 12.5	LCMO (m)	7.784(2)	5.523(4)	5.474(3)	89.27	79		12.3

Note: O stands for Orthorhombic and m stands for monoclinic phase of LCMO

4.1.3.3 Electrical transport

Fig. 4.7 (a), (b) and (c) show the electrical resistivity as a function of temperature for samples sintered at different temperatures. In all the cases, a clear insulator- to- metal transition can be seen on cooling except for the samples annealed at 1473 K. In case of sample sintered at 973 K and 1123 K, the metal-insulator transition temperature, T_{MI}, however is shifted to lower temperatures when compared to ~ 265 K for bulk sample (see Table 4.3). The lowering of transition temperature for the LCMO prepared at pH 10.5 however is the largest ~ 88 K and ~138 K for sintering at 973 K and 1123 K respectively. In the case of sample sintered at 1473 K, the resistivity shows an insulating behavior with two peaks at ~ 180 K and ~ 83 K for precursor pH of 10.5 and 12.5. However, pH 11.5 sample sintered at 1473 K shows

two broad transitions, the first at ≈ 250 K while the second transition is at T < 200 K. The first transition is the typical insulator-metal transition T_{MI} observed in bulk LCMO while the second transition is possibly due to an interplay between bulk and surface phases [80].The absolute resistivity at room temperature of LCMO sintered at 973 K in general is higher, > 10^2 Ωcm compared to that of LCMO sintered at 1123 K, < 10^2 Ωcm. The resistivity of samples prepared from precursor solutions with pH of 11.5 and 12.5 is lower compared to that prepared from the precursor solution with a pH of 10.5. An interesting behavior to note is the 'upturn' in resistivity for T ≤ 45 K in all the cases, independent of precursor solution pH and the sintering temperature. This phenomenon is observed in nanocrystalline manganites and has been attributed to 'Coulomb blockade' of charge carriers at the disordered grain boundaries [81]. The lowering of resistivity in the presence of external magnetic field is observed at temperatures higher than T_{MI} as seen in bulk LCMO.

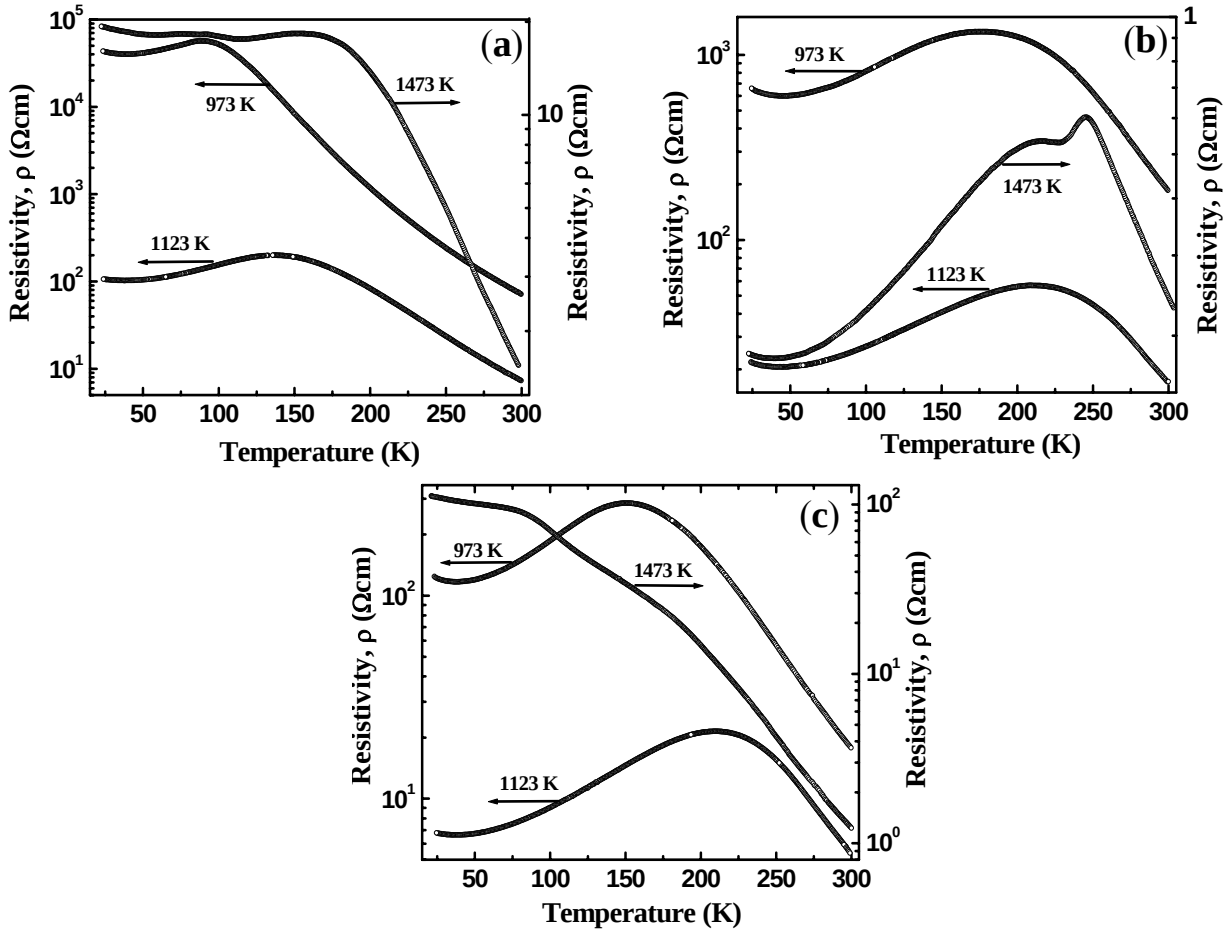

Fig. 4.7: Resistivity as a function of temperature of annealed LCMO samples for (a) pH 10.5 (b) pH 11.5 and (c) pH 12.5.

The magneto-resistance (MR) at a field of 0.85 Tesla (T) as a function of temperature for sintered samples prepared at pH = 10.5, 11.5 and 12.5 are shown in Fig. 4.8 a, b and c respectively. Samples sintered at 973 K and 1123 K, show maximum MR at low temperature. In these samples MR decreases continuously with increasing temperature. This phenomenon has been observed in nanocrystalline LCMO and generally referred to as low temperature LFMR [82]. In case of sample sintered at 1473 K, MR is maximum at T_{MI} except for sample prepared at pH 12.5.

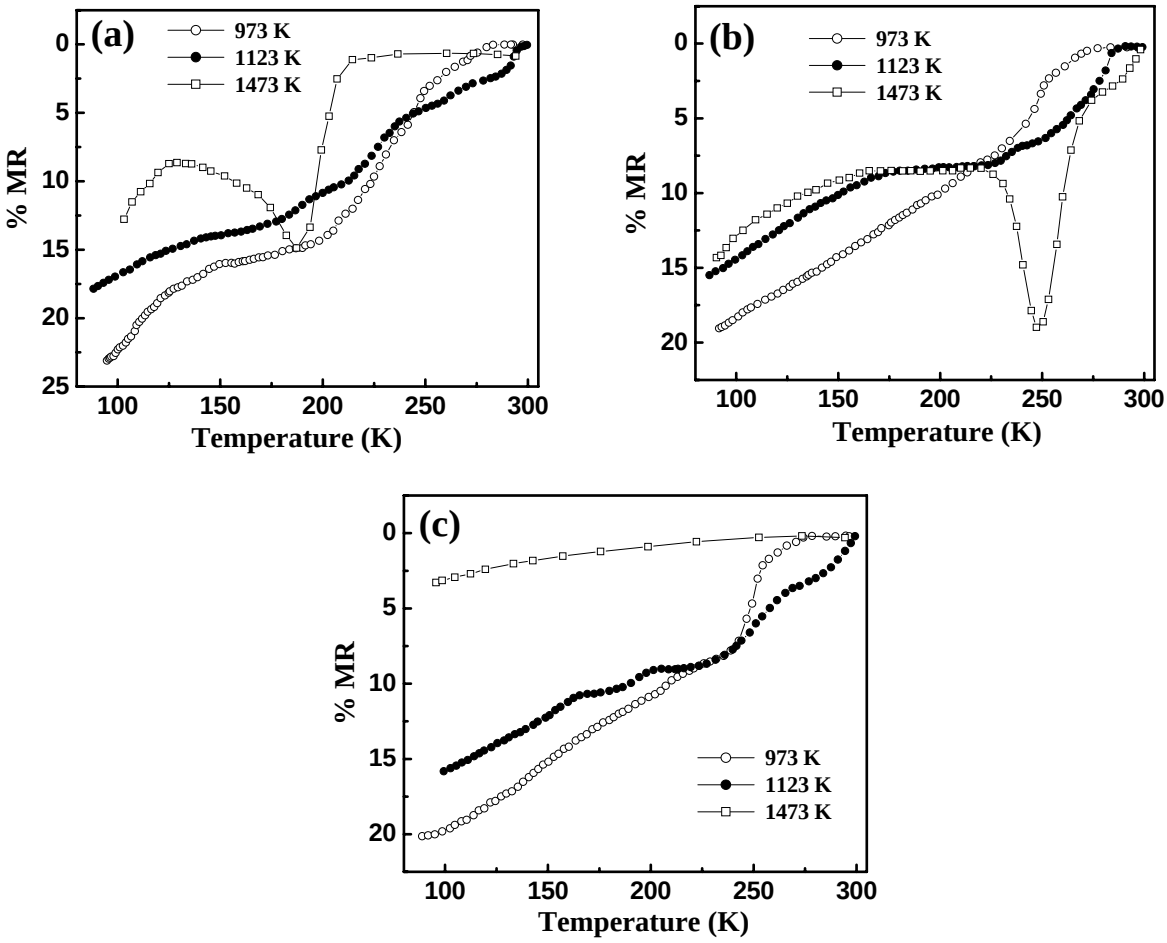

Fig. 4.8: MR variation with temperature of LCMO samples sintered at different temperatures and prepared from (a) pH = 10.5, (b) pH = 11.5 and (c) pH = 12.5. The external magnetic field is 0.85 T in all the cases.

The electronic and magnetic properties including the transformation temperatures T_{MI} and T_c, depend strongly on chemical composition of LCMO - extent of Ca-addition to $LaMnO_3$. The divalent Ca is known to substitute trivalent La and thus lead to the presence of multiple valence states for Mn. Since Mn^{3+} and Mn^{4+} form key components of the double exchange process, the electrical transport is strongly affected by a variation of Mn^{4+} / Mn^{3+} ratio [81, 83]. The transformation temperatures, T_C and T_{MI} exhibit a peak at ~ 3/8 substitution of La with divalent Ca and decrease monotonically for deviations from this composition. The concentration of Mn^{4+}, which is a measure of Ca present in the LCMO, is found to vary with the pH of the precursor solution as shown in Fig. 4.6. The Mn^{4+} content in LCMO prepared from a precursor solution with a pH of 10.5 sintered at 973 K and 1123 K as well as all pH samples sintered at 1473 K have lower value than the optimal Mn^{4+}/Mn^{3+} ratio and hence their transport behavior will not be discussed further.

The electron transport behavior of LCMO is a strong function of chemical composition, intrinsic, but also depends on extrinsic parameters such as the grain size in the case of polycrystalline materials. The absolute resistivity is known to increase by orders of magnitude as the grain size decreases and for sizes below ≈ 40 nm the insulator – metal transition is significantly suppressed with the resistivity increasing continuously as the temperature is decreased, a typical semiconducting behavior. The saturation magnetization also decreases steeply for sizes < 100 nm [84]. The absolute resistivity of nanograined LCMO obtained in the present work is also high compared to bulk values but in all the cases a clear transport and magnetic transition is observed as shown in Table 4.3. These results clearly indicate the robustness of the ferromagnetic, metallic phase in these samples inspite of the grain size being very small, 30 – 40 nm. Hence the electrical transport behavior in the whole temperature range, below and above the transition temperature T_{MI} is analyzed using the different models that have been proposed for the CMR perovskites and half metallic systems.

The electrical transport of manganites in the paramagnetic, insulating state is thermally activated due to the formation of small polarons. The observed temperature dependence however has been reported to vary from that corresponding to adiabatic polaron mediated transport to variable range hopping [85]. The resistivity $\rho_{ht}(T)$ for adiabatic polaron mediated transport is given by the relation;

$$\rho_{ht}(T) = AT\exp(E_g / k_B T) \qquad 4.1$$

where, A is a measure of ideal conductivity at elevated temperatures and depends on the polaron concentration. The activation energy for polaron mediated conduction is given by E_g. The temperature dependence according to this model is mainly due to variation of mobility of the carriers while the carrier concentration remains almost a constant. The resistivity above the transition temperature T_{MI} of all the different LCMO samples in the present work is found to follow this adiabatic transport behavior as shown in Fig. 4.9. The activation energy for transport E_g is found to be ≈ 0.12 eV for all the different nanocrystalline samples. This value is in agreement with polaron mediated transport wherein majority of the hopping energy goes towards creating the lattice distortions required for carrier mobility. The pre-exponential ideal resistivity coefficient of the nanocrystalline powders however was found to be higher by about an order of magnitude compared to the bulk value [86] reflecting the effect of grain size and slight variations in stoichiometry on the transport behavior.

The transport behavior in the ferromagnetic metallic state below T_{MI} is still not very clearly understood. An extension of the high temperature transport behavior to $T < T_{MI}$ indicates that polarons should still be the dominant charge carriers at low temperatures. Accordingly, a transport mechanism wherein correlated polaron tunneling becomes dominant has been proposed [87, 88]. The electrical resistivity according to this mechanism is given by the relation;

$$\rho(T) = \rho_0 + [E\omega_s / \sinh^2(h\omega_s / 2k_B T)] \qquad 4.2$$

where E is a constant proportional to the effective mass of polarons and ω_s the average frequency of the soft optical mode. The transport behavior of $La_{1-x}Ca_xMnO_3$ epitaxial thin films for $T < 80$ K ($T < T_C / 3$) has been found to follow this behavior for $(h\omega_s/k_B) = 86$ K for $x = 0.25$ and 101 K for $x = 0.4$. Since the average Ca-content (Mn^{4+}) in the present work is > 0.3 a value of 100 K for $(h\omega_s/k_B)$ was used to fit the low temperature resistivity data. It was found that the resistivity does not follow this behavior and deviates significantly both at low temperatures and high temperatures, T still far below T_C. This clearly indicates that correlated polaron tunneling does not occur in the presence of a large density of grain boundaries. Also, it has been reported that the magnetic neutron scattering from $La_{0.67}Ca_{0.33}MnO_3$ indicates an equivalent temperature, $h\omega_s/k_B$, for the soft optical modes to be around 250 K, [89] a temperature almost 3 times higher than the value estimated by Zhao, et al**.** [88] Hence the transport behavior of nanocrystalline LCMO in the low temperature ferromagnetic region is analyzed and modeled using conventional processes such as electron – electron, electron –

phonon and electron – magnon scattering. The resistivity in the ferromagnetic, metallic region is given by the relation;

$$\rho_{lt}(T) = \rho_0 + BT^2 + CT^n \qquad 4.3$$

where ρ_0 is the residual resistivity at T = 0, B the electron-electron scattering coefficient and C the electron – phonon or electron – magnon scattering coefficient. The value of n has been predicted to be 5 for electron – phonon scattering while it has a value of 4.5 for electron – magnon scattering [90]. In the present work a value of 4.5 corresponding to electron – magnon scattering was used to understand the low temperature transport behavior as the magnetic behavior in this temperature region is ferromagnetic with magnons as the cause of demagnetization with increasing temperature. A fit of experimental data to equation (3) is shown in Fig. 4.9. It can be clearly seen that the data agrees well with this equation indicating that electron - electron and electron – magnon scattering are the dominant processes in these nanograined LCMO materials. The residual resistivity in all the samples however is far higher than that found either in epitaxial films or bulk samples. The residual resistivity of LCMO annealed at 1123 K is an order of magnitude lower compared to the samples annealed at 973 K possibly due to small variations in oxygen stoichiometry which changes the effective Mn^{4+} concentration.

The transition from low temperature itinerant transport behavior to polaron mediated transport at high temperatures is modeled based on an effective medium approach [91]. This methodology has been used extensively to understand the transport in composites made of metal – insulator mixtures. According to this methodology the phase transition is a competition between the two phases – ferromagnetic metal and paramagnetic insulator/semiconductor. The behavior at any given temperature and magnetic field is decided by the effective volume fraction of each of the phases and an energy is associated with phase transformation. Since thermal energy is the main driving force for phase transformation, Boltzmann distribution is used to estimate the volume fractions at different temperatures. Recent high resolution transmission electron microscopy investigations have clearly shown that many of the mixed valence manganites exhibit a mixture of magnetically different phases at and below the Curie temperature [92, 93]. The presence of mixture of phases leads us to use an effective medium approach to model the transport behavior in the present work. The total resistivity ρ_{total} is considered to be a combination of the paramagnetic, insulating state resistivity ρ_{ht} and the low temperature ferromagnetic, metallic state resistivity ρ_{lt} weighted suitably by the respective volume fractions and is given by;

$$\rho_{total}(T) = m(T)\rho_{lt}(T) + [1 - m(T)]\rho_{ht}(T) \quad 4.4$$

where m represents the metallic volume fraction. The metallic volume fraction at any temperature T is given by the relation;

$$m(T) = 1/[1 + \exp(\Delta E / k_B T)] \quad 4.5$$

where ΔE is the difference between the ferromagnetic, metallic ground state and the paramagnetic, insulating state. The energy difference between the ferromagnetic ground state and the paramagnetic insulating state, ΔE at T = 0 K is E_0. As the temperature increases the energy difference ΔE decreases and at the Curie temperature Tc the energy difference ΔE becomes 0. This temperature dependence of the energy difference between the two states, ΔE can be expressed in the form

$$\Delta E = -E_0\left(1 - \frac{T}{T_c}\right) \quad 4.6$$

so that a continuity across the ferromagnetic metallic and paramagnetic insulating regions is maintained. It is seen from Eqs. (5) and (6) that the metallic volume fraction is nearly 1 at T = 0 K and decreases continuously with increasing temperature. The metallic volume fraction m is 1/2 at the transition temperature T_c and this volume fraction is at the threshold of electrical transport percolation limit, 1/2 for two-dimensional systems and 1/3 for three-dimensional systems. Since the dimensionality of transport in nanocrystalline three-dimensional systems is not very clearly known, this type of volume fraction distribution is valid as a first approximation. For $T > T_c$ the metallic volume fraction decreases below the percolation limit with the paramagnetic insulating phase transport becoming dominant.

The transport behavior of nanocrystalline LCMO powders synthesized at different temperatures was modeled using the above set of equations and the results are shown in Table 4.2 and Figure 4.9. It can be clearly seen that the overall resistivity variation is in agreement with the experimental results in all the cases. The absolute value of resistivity of samples sintered at 973 K is higher compared to that of 1123 K sintered samples and the value of ΔE is also different indicating that both stoichiometry and the grain size play a significant role in transport. The agreement between the modeled resistivity and the data for 1123 K annealed samples is nearly perfect indicating that higher temperature annealing results in a near stoichiometric composition and hence an ideal transport behavior. The ground state energy for the ferromagnetic metallic state is found to be ≈ 0.24 eV, in agreement with the theoretical estimate for the psuedogap formation in mixed phase manganites [94].

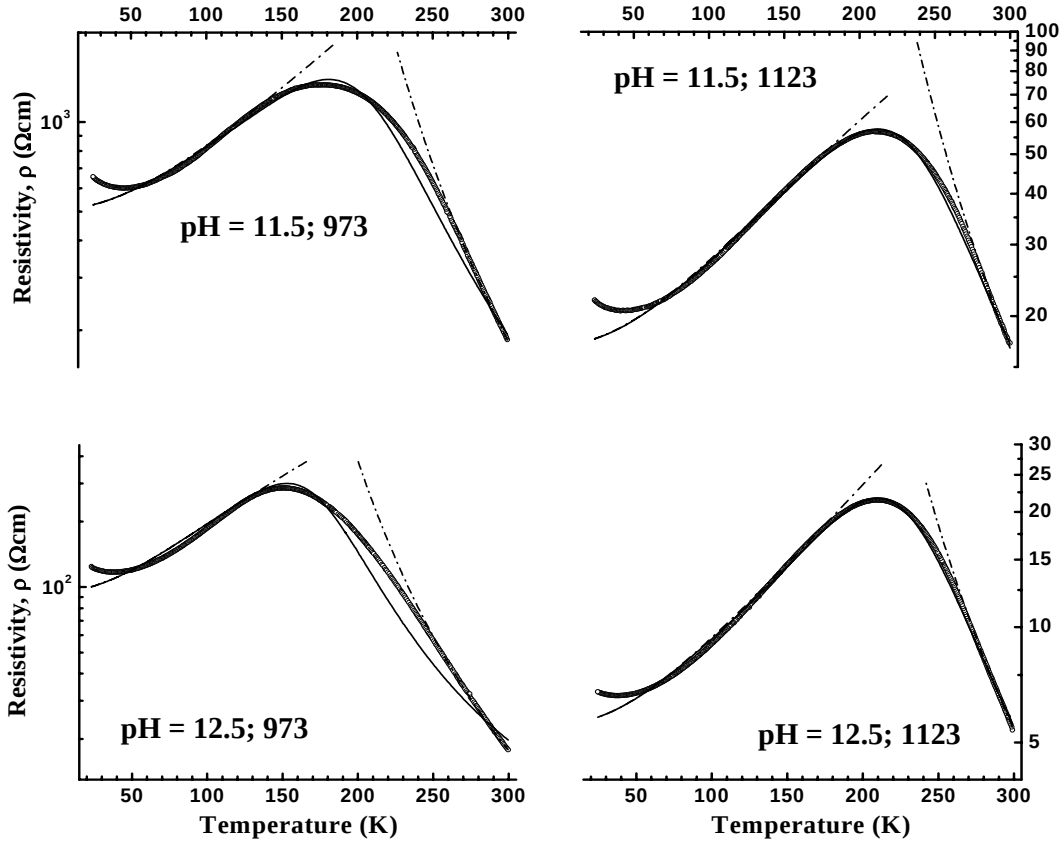

Fig. 4.9: The temperature dependence of electrical resistivity being fitted to different models discussed in the text. Symbols represent experimental data and the lines are fits to low T, high T and complete temperature range.

Table 4.2: The different parameters used to model the electrical transport as described by the equations (1), (3) and (5).

973 K for 1 h.	ρ_0, Ω cm	B, Ω cm K^{-2}	C, Ω cm $K^{-4.5}$	AT, Ω cm K^{-1}	E_g, K	ΔE, K
pH = 11.5	508	3.15×10^{-2}	1.55×10^{-9}	9.995×10^{-5}	1350	2258
pH = 12.5	95	9.92×10^{-3}	1×10^{-9}	3.997×10^{-4}	1083	1928
1123 K for 30 mins.						
pH = 11.5	17	1.011×10^{-3}	1×10^{-10}	2.945×10^{-4}	955	2789
pH = 12.5	5.6	3.69×10^{-4}	1×10^{-11}	1.52×10^{-5}	1828	2765

4.1.3.4 Magnetization

Fig. 4.10 shows the magnetization as a function of pH of the precursor solution at 85 K for LCMO samples sintered at three different temperatures. Inset of Fig. 4.10 shows M-H loop of sample prepared at pH 11.5 sintered at different temperatures. From M-H loop (inset of Fig. 4.10), it indicates that the sample prepared from precursor solution with a pH of 11.5 shows a saturation behavior. The magnetization value at 20 kOe is higher compared to samples prepared with other pH precursors.

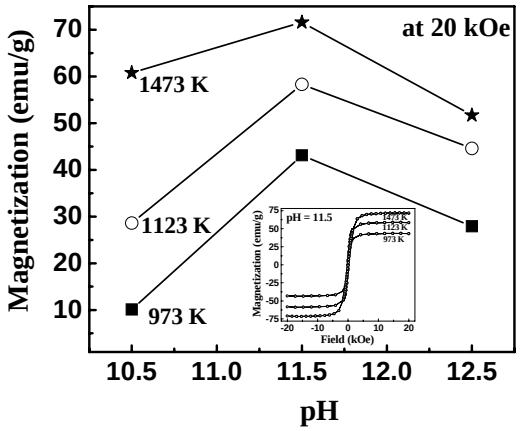

Fig. 4.10: Saturation magnetization at 20 kOe as a function of pH of sintered LCMO samples.

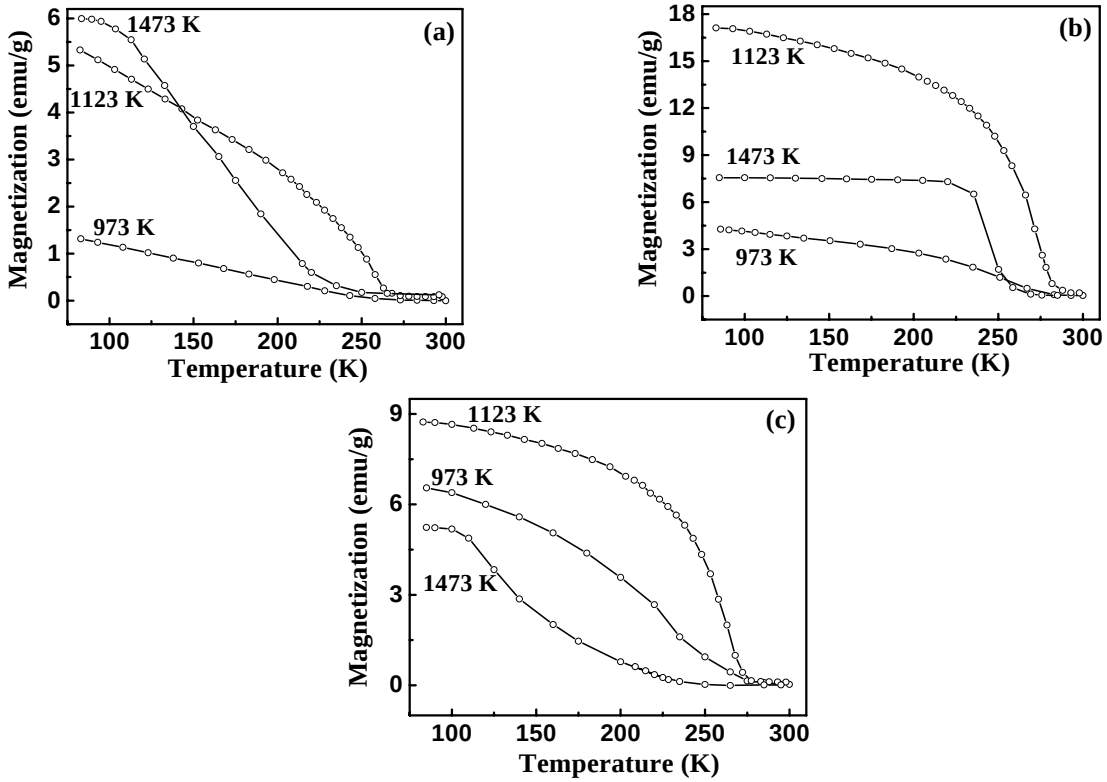

Fig. 4.11: Magnetization as a function of temperature for sintered LCMO samples (a) pH = 10.5, (b) pH = 11.5 and (c) pH = 12.5 at 100 Oe

Fig. 4.11 a, b and c show the magnetization as a function of temperature at a field of 100 Oe for pH 10.5, 11.5 and 12.5 respectively sintered at three different temperatures. The magnetic transition is higher for pH 11.5 samples sintered at 1123 K. The T_c variation as a function of pH is shown in inset of Fig. 4.12. Table 4.3 shows the magnetization value at 20 kOe, coercivity H_c and transition temperature T_c of all samples. From the transport and magnetic properties, it has been observed that for pH 11.5 sintered at 1123 K and 1473 K samples show better CMR properties compared to other pH samples due to an optimal Mn^{4+} concentration and better crystal quality, Fig. 4.3 and Fig. 4.6.

Table 4.3: The experimentally observed property parameters of the $La_{0.67}Ca_{0.33}MnO_3$ nanocrystalline powders prepared using different processing conditions. T_C is the magnetic transition temperature, T_{MI} the electrical transition temperature, ρ the resistivity and MR the magnetoresistance.

973 K	T_C, K	T_{MI}, K	ρ at T_{MI} Ω cm	ρ at 300 K Ω cm	% MR at 90 K	% MR at T_{MI}	H_C (Oe)	M (emu/g) at 20 kOe
pH 10.5	225	88	56827	71.7	23	23	116	10
pH 11.5	251	177	1334	185.7	19	12	94	43
pH 12.5	239	151	285.5	17.8	20	15	131	28
1123 K								
pH 10.5	258	138	199.5	7.3	18	14	92	29
pH 11.5	273	210	56.8	17.1	15	8	93	58
pH 12.5	263	209	21.4	5.8	15	12	122	49
1473 K								
pH 10.5	176	160 / 86	18.3 / 18.1	1.5	12	12	49	61
pH 11.5	250	245 / 213	0.602 / 0.53	0.23	14	19	23	71
pH 12.5	165	160 / 82	29.7 / 86.6	1.27	3.2	1.5	76	52

The percentage of Mn^{4+} is directly proportional to the concentration Ca ion in LCMO. Therefore, variation of T_c with Mn^{4+} concentration is compared with percentage of Ca ion in LCMO [81] as shown in Fig. 4.12. It has been seen that the trend in T_c variation with Mn^{4+} is similar to that reported for LCMO with Ca concentration. The Mn^{4+} concentration in samples sintered at 973 K and 1123 K is in the ferromagnetic, metallic region. However samples sintered at 1473 K (except for pH 11.5) are in ferromagnetic, insulator region as seen from LCMO phase diagram [11] (Fig. 1.4 in the Introduction section). Inset (a) and (b) of Fig. 4.12 show the variation of T_{MI} and T_c as a function of pH of the samples respectively.

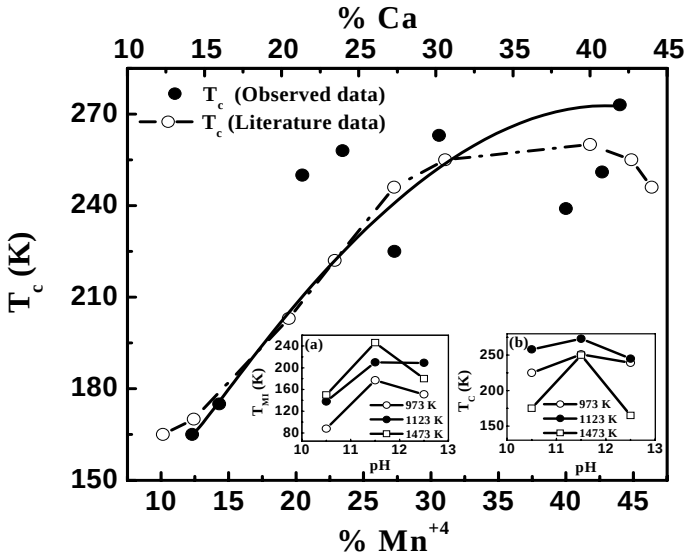

Fig. 4.12: Variation of T_c with Mn^{+4} concentration is compared with percentage of Ca ion (reported from the phase diagram, Fig. 1.4) in LCMO samples. Inset (a) and (b) show the variation of T_{MI} and T_c respectively as a function of pH of the samples. The line through the data point is a guide.

4.1.4 Summary

$La_{0.67}Ca_{0.33}MnO_3$ nanocrystalline powders were prepared by microwave refluxing from organic precursors by changing parameters like precursor solution pH and sintering temperatures. The orthorhombic manganite phase is found to be highly stable upto 1123 K annealing. The resistivity (ρ), magnetoresistance (MR), metal – insulator transition (T_{MI}) and the magnetic transition (T_c) strongly depend on Mn^{4+} concentration, grain size, pH of the precursor solution and annealing temperature. It has been observed that LCMO prepared from a precursor solution with a pH of 11.5, gives better CMR properties.

Hence, this processing condition was used to synthesize LCMO/Ni-ferrite nanocomposite, the results of which are discussed in the next section.

4.2 Structural, transport and magnetic properties of microwave synthesized La-Ca-Manganite – Ni-Ferrite nanocomposites

4.2.1 Introduction

In the present work, composite mixtures of La-Ca-manganite, a CMR perovskite and Ni-ferrite, a magnetic insulator, have been made in-situ using microwave assisted refluxing technique. This technique has the inherent advantage of uniformly distributing the two phases with similar grain size distribution, as they will be subjected to identical processing conditions. This is a novel technique to prepare nanocomposite materials at moderate temperatures when compared with conventional solid-state route. The structure, electrical transport and magnetic transition of these composites are studied to understand the effect of Ni-ferrite addition on the electrical transport and magnetic properties of La-Ca-manganite.

4.2.2 Experimental details

Nanograined composites of (1-x) M $La_{0.67}Ca_{0.33}MnO_3$ (LCMO): x M $NiFe_2O_4$ (NF) where x = 0, 0.01, 0.02, 0.05, 0.10, 0.15, 0.50 and 1, M represents molecular weight, were prepared by precipitation using microwave refluxing. Simultaneously decreasing the concentration of LCMO from 1 molarity and increasing the concentration of NF in solution increases the quantity of NF in the composites. The flow chart for preparation of LCMO: NF composite is shown in Fig. 4.13. Stoichiometric amounts of La-acetate, Ca-acetate, Mn-acetate, $NiCl_2.6H_2O$ and $FeCl_3$ salts were partially dissolved in ethylene glycol to obtain a precursor solution. The pH of this solution was ~ 5.8 for all compositions, except for the case of x = 1 where the pH was 0.9. Initially the salts were not completely soluble in ethylene glycol. Addition of KOH to this solution at ≈ 353 K converts the acetate to hydroxides and the solution becomes clear at a pH of 10.5. Increasing the pH to ~ 11.5 leads to a gel formation in all the cases except for x = 1 where it forms a gel at a pH of ~ 2.5. The gel solution was refluxed at ~ 473 K, boiling point of ethylene glycol, using a microwave heat source (250 GHz, 980 Watts) for a period of 1.0 hr. The precipitate obtained after refluxing was centrifuged and washed with distilled water several times (20). The centrifuged powder was finally dried using an IR lamp. Thermogravimetric analysis was done up to 1173 K at a rate of 283 K min^{-1} to determine the calcination and sintering temperatures. The thermogravimetric analysis shows that in all the cases ~ 30-35 % weight loss occurs below 523 K corresponding to evaporation of ethylene glycol. The weight loss decreases with increasing temperature and

becomes nearly 0 for T > 973 K. Hence, calcination of the powders was done at 973 K for 1 h. The calcined powder was cold pressed into pellets. These pellets were sintered at two different temperatures at 1123 K for 30 minutes and 1473 K for 4 hrs. We have studied the electrical as well as magnetic properties of these composites sintered at two different temperatures.

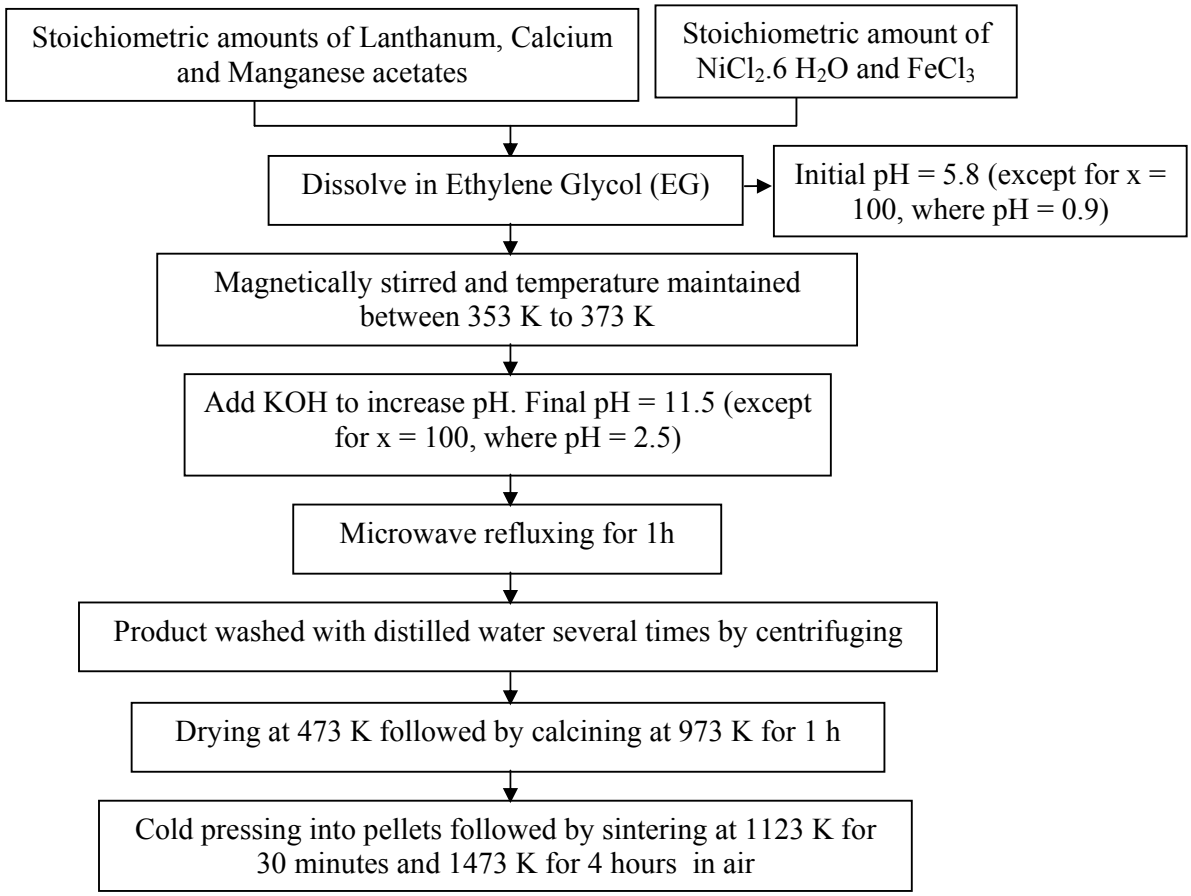

Fig. 4.13: Schematic flow-chart for preparation of nanograined (1-x) M $La_{0.67}Ca_{0.33}MnO_3$ (LCMO): x M $NiFe_2O_4$ (NF) composite.

The structural analysis was performed using a combination of X-ray diffraction with Rietveld analysis and TEM. The electrical transport in the temperature range 20 K – 300 K was studied using the standard dc four probe technique. An external magnetic field of 0.85T was used to determine the magnetoresistance as a function of temperature. The magnetic transition in the temperature range 80 K – 300 K was studied using a Faraday balance in an external field of 0.3 T. The magnetization behavior (M-H loop) and high temperature magnetic transition in the temperature range 300 K – 1000 K was studied using vibrating sample magnetometer (VSM, LakeShore).

4.2.3 Results and discussion

4.2.3.1 Structure and microstructure

The diffraction patterns do not show any clear peaks in the as-prepared condition indicating the absence of either of the crystalline phases LCMO or Ni-ferrite (NF). The crystalline phase formation takes place on calcining at 973 K followed by sintering at two different temperatures (1123 K and 1473 K). The results of phase identification by powder x-ray diffraction of these composites sintered at 1123 K and 1473 K are shown in Fig. 4.14 and Fig. 4.15 respectively.

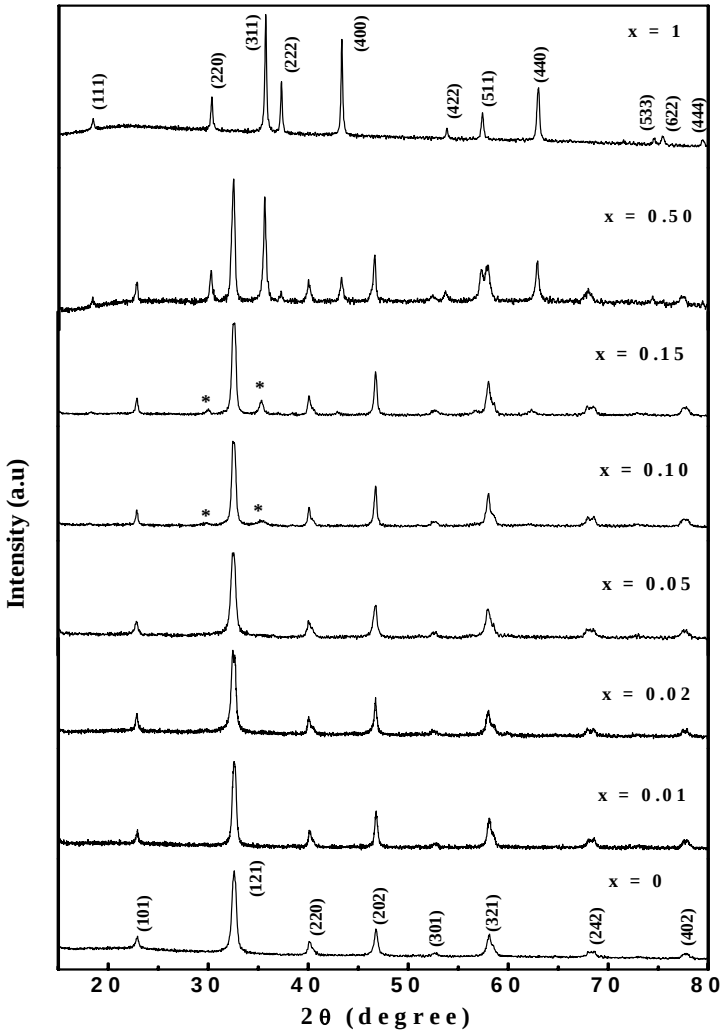

Fig. 4.14: The x-ray diffraction patterns of (1-x) M $La_{0.67}Ca_{0.33}MnO_3$ (LCMO): x M $NiFe_2O_4$ (NF) composites sintered at 1123 K exhibit clear crystalline peaks. The NF phase is observed only in composites with x > 0.10 M. All the peaks could be identified with either LCMO or NF phases. * denote the formation of Ni-ferrite phase in the composite.

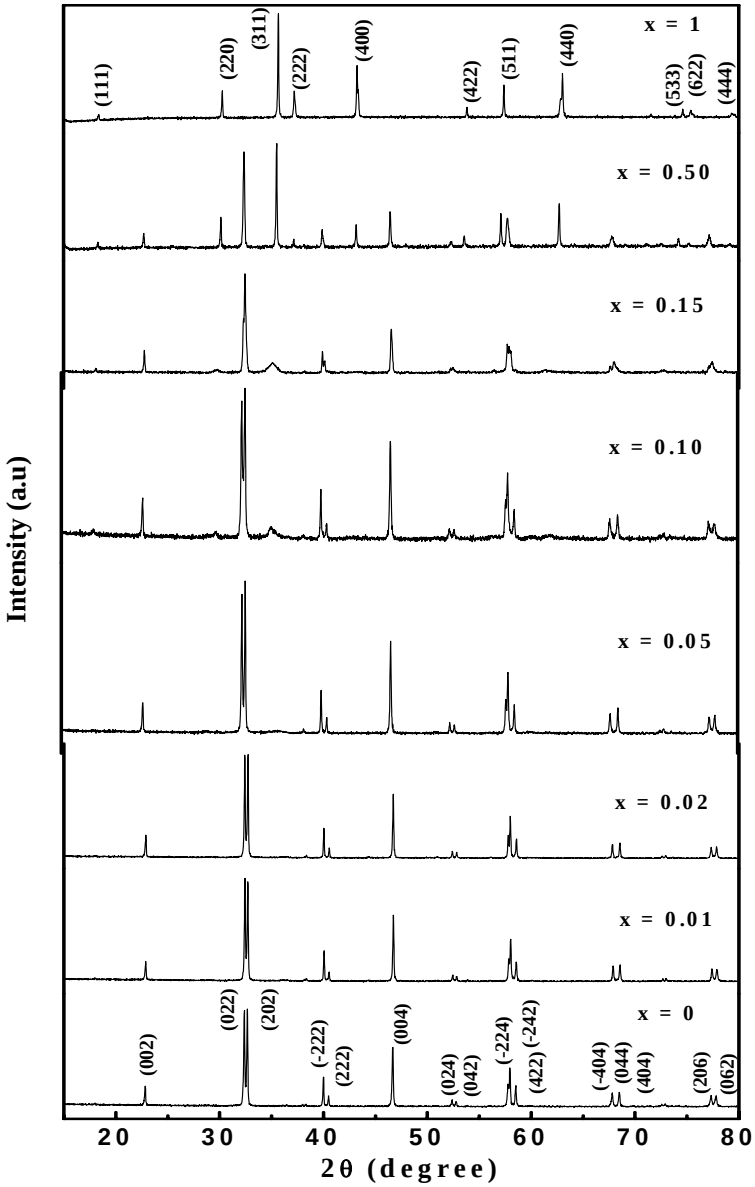

Fig. 4.15: The x-ray diffraction patterns of (1-x) M $La_{0.67}Ca_{0.33}MnO_3$ (LCMO): x M $NiFe_2O_4$ (NF) composites sintered at 1473 K exhibit clear crystalline peaks. The NF phase is observed only in composites with x > 0.10 M. All the peaks could be identified with either LCMO or NF phases. NF phase formation starts above x ≥ 0.10 NF.

In both the cases, in composites with x ≤ 0.05 M NF, the diffraction pattern indicates the presence of only the LCMO phase. Increasing the NF content to 0.10 M results in the appearance of separate NF phase and this grows with increasing concentration. All the peaks in the x-ray diffraction pattern could be identified with either the LCMO phase or NF phase. This clearly shows that the two phases LCMO and NF, form separately with no detectable third phase.

A Reitveld structural refinement procedure was used to analyze the diffraction patterns. Fig. 4.16 and Fig. 4.17 show the Rietveld analysis of LCMO: NF composites sintered at 1123 K and 1473 K respectively for samples x = 0.10, 0.15 and 0.50. For the composites sintered at 1123 K show that the LCMO phase has an orthorhombic crystal structure corresponding to the Pnma space group whereas NF is cubic, space group Fd $\bar{3}$ m. The unit cell parameters, unit cell volume and weight fraction of LCMO and NF phase obtained from Reitveld refinement for composites sintered at 1123 K are given in Table 4.4. The samples sintered at 1473 K show a structural transition from monoclinic form (x ≤ 0.15 M, space group I 2/a) to orthorhombic form of LCMO (x > 0.15, space group P n m a) with increasing NF concentration which may be due to substitution of Mn^{3+} ion (ionic radius 0.66Å) by lower ionic radii of Fe^{3+} (ionic radius 0.64Å). This leads to an increase in the tolerance factor τ, which is responsible for low to high symmetric structure transition. The unit cell parameters, unit cell volume and weight fraction of LCMO and NF phase obtained from Reitveld refinement for the composites sintered at 1473 K are given in Table 4.5.

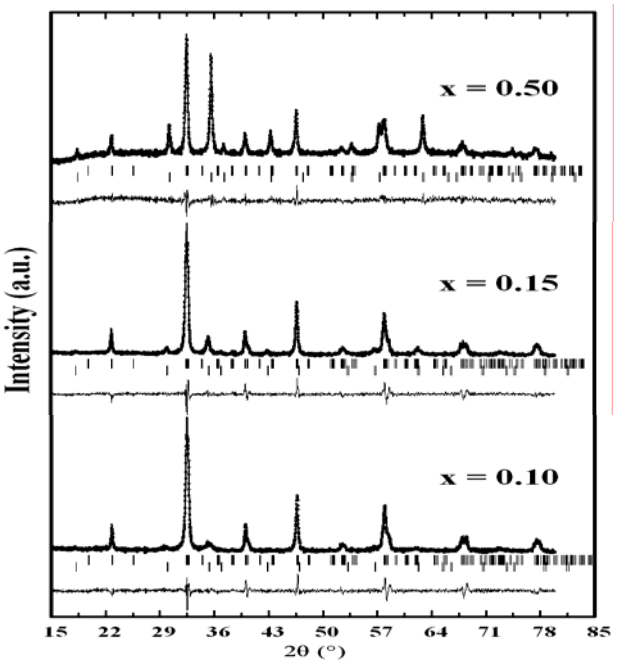

Fig. 4.16: The Rietveld analysis of LCMO: NF composites for samples x = 0.10, 0.15 and 0.50 annealed at 1123 K.

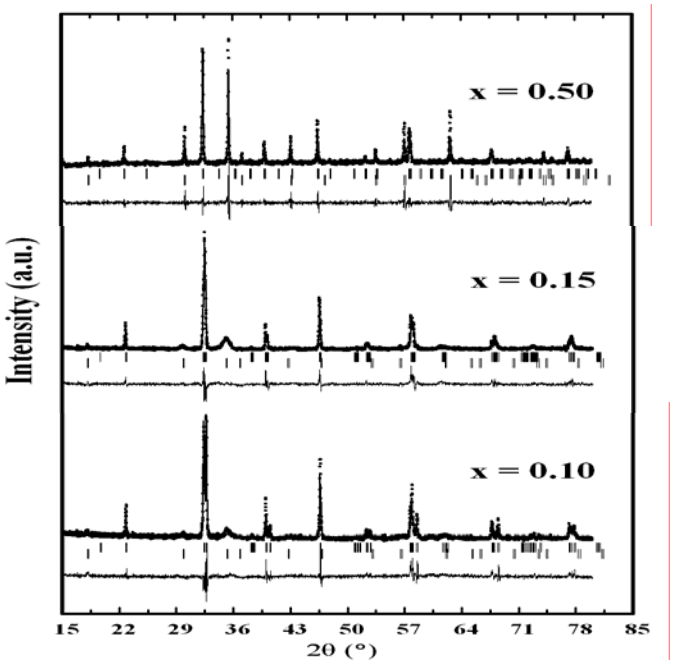

Fig. 4.17: The Rietveld analysis of LCMO: NF composites for samples x = 0.10, 0.15 and 0.50 annealed at 1473 K.

Note: The Reitveld fit is shown by continuous line through the data points (•) and the position of Bragg lines for the two phases is shown by vertical lines, (LCMO - top and NF - bottom) below the data.

Table 4.4: The unit cell parameters (a, b and c), cell volume and weight percentage of different phases obtained by Reitveld refinement from the x-ray diffraction pattern of the composites LCMO: x NF annealed at 1123 K. L represents LCMO phase and NF represents Ni-ferrite phase.

		Lattice Parameter, Å					
L: x NF composite	Phase	a	b	c	wt %	Space group	Cell volume, $Å^3$
x = 0	L (O)	5.507(8)	7.766(9)	5.465(3)	100	P n m a	233.8
x = 0.01	L (O)	5.515(3)	7.769(3)	5.469(5)	100	P n m a	234.3
x = 0.02	L (O)	5.520(6)	7.774(1)	5.471(2)	100	P n m a	234.8
x = 0.05	L (O)	5.521(6)	7.776(3)	5.472(8)	100	P n m a	235.0 600.2
x = 0.10	L (O) NF (C)	5.522(8) 8.434(2)	7.785(8) 8.434(2)	5.476(1) 8.434(2)	88 12	P n m a Fd $\bar{3}$ m	235.4 599.9
x = 0.15	L (O) NF (C)	5.523(2) 8.430(4)	7.781(8) 8.430(4)	5.473(2) 8.430(4)	82 18	P n m a Fd $\bar{3}$ m	235.3 599.1
x = 0.5	L (O) NF (C)	5.524(0) 8.354(6)	7.799(7) 8.354(6)	5.497(6) 8.354(6)	54 46	P n m a Fd $\bar{3}$ m	236.8 583.1
x = 1	NF (C)	8.352(8)	8.352(8)	8.352(8)	100	Fd $\bar{3}$ m	582.7

Note: O represents orthorhombic structure of LCMO and C represents cubic structure of Ni-ferrite.

Table 4.5: The unit cell parameters (a, b and c), cell volume and weight percentage of different phases obtained by Reitveld refinement from the x-ray diffraction pattern of the composites LCMO: x NF annealed at 1473 K. L represents LCMO phase and NF represents Ni-ferrite phase.

		Lattice Parameter, Å						
L: x NF composite	Phase	a	b	c	β (angle)	wt %	Space group	Cell volume, $Å^3$
x = 0	L (m)	7.785(8)	5.519(2)	5.479(3)	89.214	100	I2/a	234.2
x = 0.01	L (m)	7.772(2)	5.514(7)	5.472(5)	89.221	100	I2/a	234.8
x = 0.02	L (m)	7.775(5)	5.518(2)	5.473(3)	89.229	100	I2/a	235.3
x = 0.05	L (m)	7.778(3)	5.521(3)	5.475(8)	89.235	100	I2/a	235.6 600.4
x = 0.10	L (m) NF (C)	7.782(5) 8.453(3)	5.528(2) 8.453(3)	5.477(3) 8.453(3)	89.251	89 11	I2/a Fd $\bar{3}$ m	236.2 600.2
x = 0.15	L (m) NF (C)	7.792(3) 8.428(1)	5.534(7) 8.428(1)	5.489(9) 8.428(1)	89.869	83 17	I2/a Fd $\bar{3}$ m	236.7 599.8
x = 0.5	L (O) NF (C)	5.531(9) 8.372(9)	7.807(1) 8.372(9)	5.520(7) 8.372(9)		52 48	P n m a Fd $\bar{3}$ m	236.9 583.1
x = 1	NF (C)	8.353(2)	8.353(2)	8.353(2)		100	Fd $\bar{3}$ m	582.7

Note: m represents monoclinic and O represents orthorhombic structure of LCMO and C represents cubic structure of Ni-ferrite.

The size of the LCMO and NF grains in the composite was determined from the half width of the diffraction peaks using Scherer relation and is given in Table 4.6. The grain size of the composites sintered at 1123 K ranges from 20 nm to 40 nm. However the grain size increases as the sintering temperature increases to 1473 K by about 5 times.

The size of the particles was determined independently using transmission electron microscopy. The particle size increases and is in the range of 200 nm to 500 nm as the annealed temperature increases to 1473 K. The diffraction patterns of pure LCMO, NF, LCMO: 0.50 M NF and the bright field image of composite with x = 0.50 M NF are shown in Fig. 4.18. The grains are polyhedral in nature and agglomerate into large particles of size ≈ 70 nm. The average grain size is found to be ~ 25 nm, in agreement with the X-ray results. The selected area diffraction pattern from the composite with 0.50 M NF shows several rings which were found to be a superposition of the diffraction patterns from pure LCMO and NF. In addition, the bright field image shows that the two phases, LCMO and NF are present as individual components in the composite with different grain sizes without intermixing. The selected area diffraction patterns however could not be indexed partly due to the complex nature and partly due to a lack of clarity in the patterns.

Table 4.6: The grain size and particle size of LCMO: NF composite sintered at 1123 K and 1473 K with different composition.

	Annealed at 1123 K			Annealed at 1473 K		
L: x NF composite	Crystallite size (XRD), nm		Particle size range (TEM), nm	Crystallite size (XRD), nm		Particle size range (TEM), nm
	LCMO Phase	NF Phase		LCMO Phase	NF Phase	
0	14	*	20 – 40	75	*	200 - 500
0.01	14	*		75	*	
0.02	15	*		77	*	
0.05	16	*		79	*	
0.10	17	11		85	15	
0.15	18	20		89	28	
0.50	25	35		92	74	
1.00	---	38		---	80	

Note: * not detected

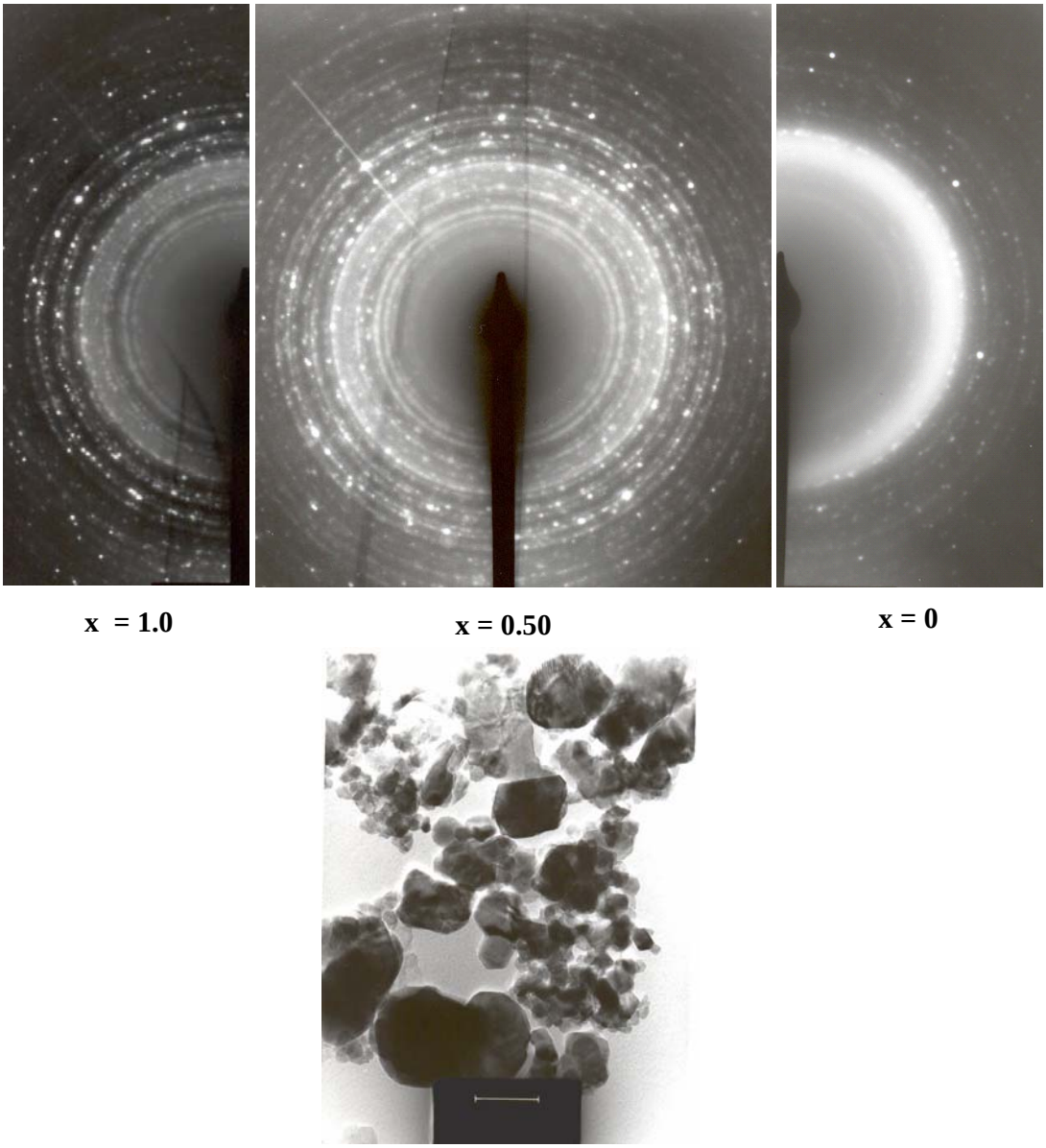

Fig. 4.18: Diffraction pattern of composite with x = 0.50 M NF shows several rings which were found to be superposition of the diffraction patterns from pure LCMO (x = 0 M) and NF (x = 1.0 M). The bright field micrographs of x = 0.50 M composite shows mixture of small and large grains which indicates mixture of two phases. The scale bar corresponds to 100 nm.

Composites of 50 M $La_{0.67}Ca_{0.33}MnO_3$ (LCMO): 50 M $NiFe_2O_4$ (NF) where M represents molecular weight, were prepared through conventional solid-state route. Stoichiometric amount of La_2O_3, $CaCO_3$, Mn_2O_3, NiO, and Fe_2O_3 were mixed in a mortar pestle. The mixed powders were heat-treated at 1123 K for 2 hours. LCMO and NF phase along with impurity phase formation take place at 1123 K as seen from the X-ray diffraction pattern (Fig. 4.19). This clearly shows that LCMO: NF composite can be made only by microwave refluxing at low processing temperature.

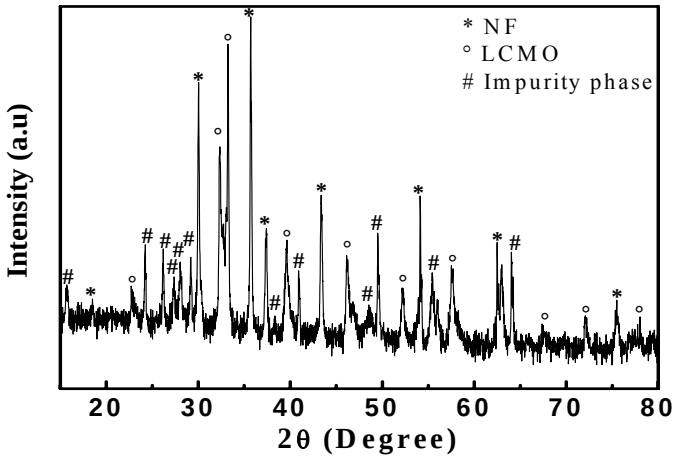

Fig. 4.19: X-ray diffraction pattern of 50 LCMO: 50 NF heat-treated at 1123 K for 2 hours through conventional solid-state route.

4.2.3.2 Electrical transport

The electrical resistivity of LCMO, NF and the composites obtained by sintering at 1123 K and 1473 K were studied in the temperature range 20 K to 300 K and are shown in Fig. 4.20 and Fig. 4.21 respectively. For samples sintered at 1123 K, single phase orthorhombic structure of LCMO, exhibits an insulator – metal transition, T_{MI} (for compositions x = 0 and 0.01 M) on cooling at ~ 215 K, in agreement with earlier results [26]. Samples sintered at 1473 K show two transitions for samples with x = 0 and 0.01 M. The double peaks in resistivity have been seen in many polycrystalline systems and attributed generally to the structure and thickness of grain boundaries or to the non-magnetic regions between LCMO grains [95-97]. In our case, the first sharp transition may be due to intergrain scattering and second broad transition could presumably be due to presence of microscopic or chemical inhomogeneities [33, 98]. In both the cases, addition of NF to LCMO is found to decrease this transition temperature and finally lead to complete suppression for $x \geq 0.05$ M NF. The composites in both the cases exhibit a typical semiconducting or insulating behavior for $x \geq$

0.05 M due to suppression of double exchange with increasing NF content. The absolute resistivity also increases by orders of magnitude with increasing NF in the composites. The resistivity below 90 K for x = 0.05 M, 0.10 M and 0.15 M composites could not be measured accurately as it was higher than 10^6 Ω cm. The resistivity of both pure NF and x = 0.50 composites also could not be measured as it was highly insulating in nature and is beyond of the measurement limit of instrument.

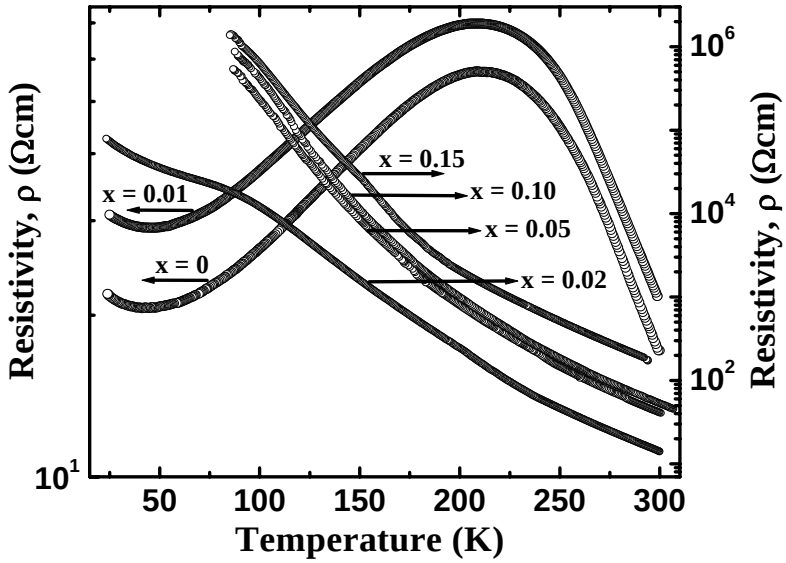

Fig. 4.20: Electrical resistivity as a function of temperature of composite LCMO: NF sintered at 1123 K.

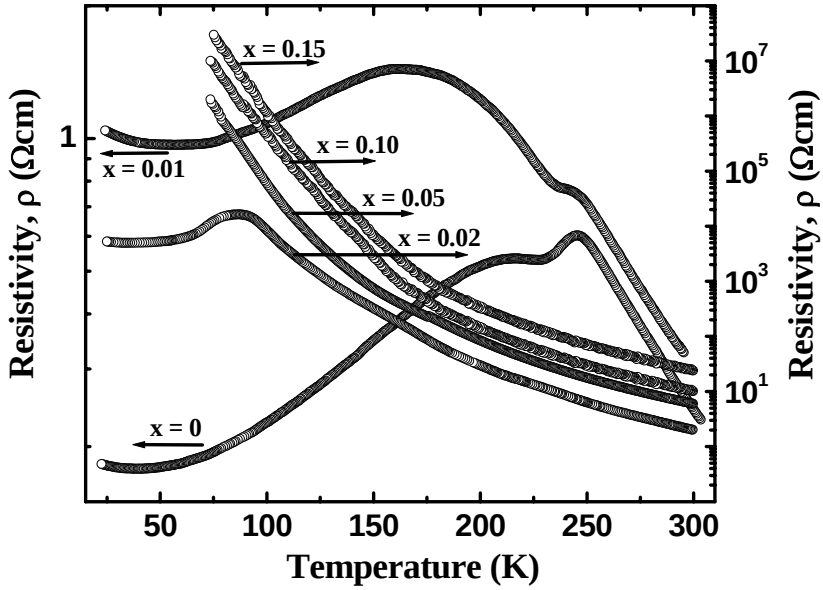

Fig. 4.21: Electrical resistivity as a function of temperature of composite LCMO: NF sintered at 1473 K.

The magnetoresistance measured in a external magnetic field of 0.85 T is shown in Fig. 4.22. In case of 1123 K sintered samples, for $x \leq 0.02$ M NF, the magnetoresistance decreases with increasing NF content. Increase of magnetoresistance as the temperature decreases is possibly due to high grain boundaries in nanocrystalline grains as discussed by Balcells et. al. [99]. However, for samples sintered at 1473 K, for $x \leq 0.02$ M, the magnetoresistance is maximum near the metal – insulator transition temperature (T_{MI}) as also seen by Li et.al [100]. Both composites sintered at 1123 K and 1473 K with $x > 0.02$ M NF exhibit a semiconducting behavior which does not have any negative magnetoresistance. The MR value decreases as the sintering temperature increases whenever negative MR is observed.

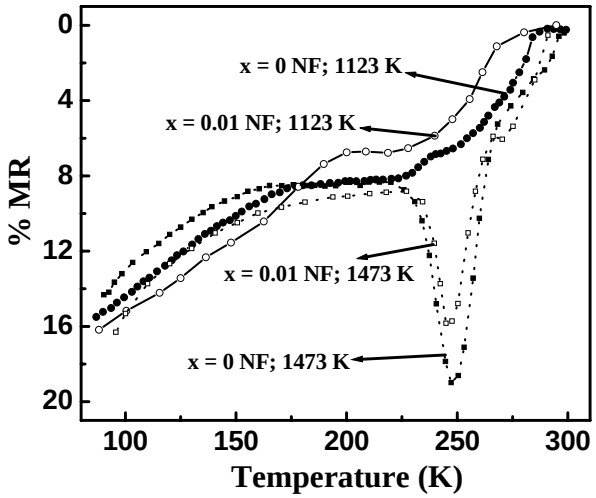

Fig. 4.22: Percentage MR as a function of temperature of composite with x = 0.0 and 0.01 annealed at 1123 K and 1473 K.

4.2.3.3 Magnetization

The variation of magnetic susceptibility with temperature T measured in an external field of 0.3 T in the range 80 K to 300 K for composites sintered at 1123 K and at 1473 K are shown in Fig. 4.23 and Fig. 4.24 respectively. The paramagnetic to ferromagnetic transition on cooling is progressively decreased to lower temperatures with increasing addition of NF to LCMO (see both Table 4.6 and Table 4.7) in both the cases. For composites annealed at 1123 K, the transition temperature T_C of LCMO decreases from ~ 250 K for pure LCMO to ~ 125 K when x = 0.15 M where as for the composites annealed at 1473 K it is 240 K for x = 0 M and 120 K for x = 0.15 M. For composites with > 0.15 M NF the magnetic behavior is dominated by NF which has bulk T_C value of 858 K, well above the room temperature. In both the cases, pure NF and 0.50 M NF composite exhibit a nearly temperature independent susceptibility behavior for T < 300 K consistent with the transition temperature of pure NF.

The lowering of T_C with increasing NF is in qualitative agreement with the electrical transport behavior wherein T_{MI} is found to decrease with increasing NF. The main difference however is that the composites with ≤ 0.15 M NF indicate a magnetic transition T_C below room temperature while the metal - insulator transition T_{MI}, is completely suppressed for NF ≥ 0.05 M. This decoupling of electrical and magnetic transitions shows that the grain boundaries play a significant role in magnetotransport behavior of the composites.

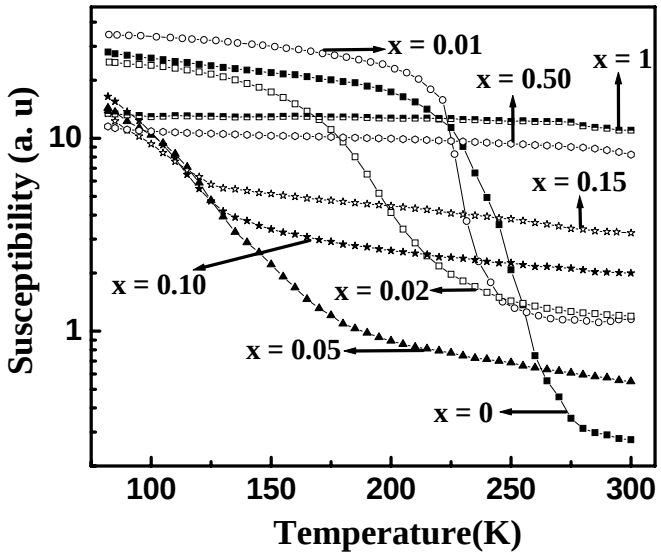

Fig. 4.23: Magnetic susceptibility with temperature T measured in an external field of 0.3 T for composites sintered at 1123 K.

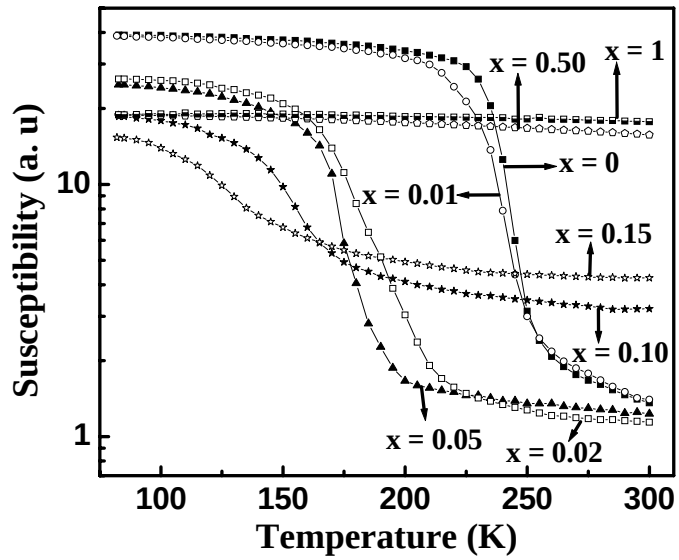

Fig. 4.24: Magnetic susceptibility with temperature T measured in an external field of 0.3 T for composites sintered at 1473 K.

The variation of magnetization with temperature T measured in an external field of 250 Oe in the range 300 K to 950 K for composites ($x \geq 0.10$) sintered at 1123 K and 1473 K are shown in Fig. 4.25 (a) and (b) respectively. The sample x = 1.0 has a T_c of nearly 863 K which corresponds to bulk NF T_c value. The transition temperature T_c of NF decreases with LCMO content in the LCMO: NF composites. This may be due to non-stoichiometric composition of nickel ferrite in the composites.

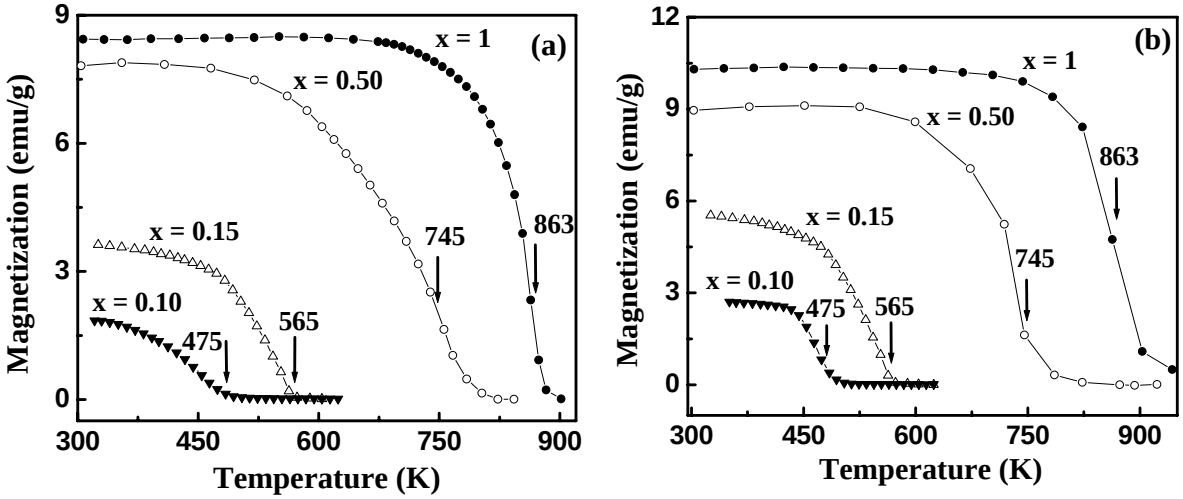

Fig. 4.25: Magnetization with temperature T measured in an external field of 250 Oe for composites sintered at (a) 1123 K and (b) 1473 K.

The magnetization as a function of field at room temperature for composites sintered at 1123 K and 1473 K are shown in Fig. 4.26 and Fig. 4.27 respectively. Room temperature data shows paramagnetic (PM) nature for $x \leq 0.02$ M in both the cases (see inset Fig. 4.26 and Fig. 4.27). For composites with $x > 0.02$ M, magnetization shows non-linear behavior with magnetic moment increasing with x.

The magnetization as a function of field at 85 K for composites sintered at 1123 K and 1473 K are shown in Fig. 4.28 and Fig. 4.29 respectively. For both composites, the saturation magnetization of LCMO decreases as the concentration of NF increases. Table 4.6 and Table 4.7 summarize the electrical as well as magnetic data of the LCMO: NF composite sintered at 1123 K and 1473 K.

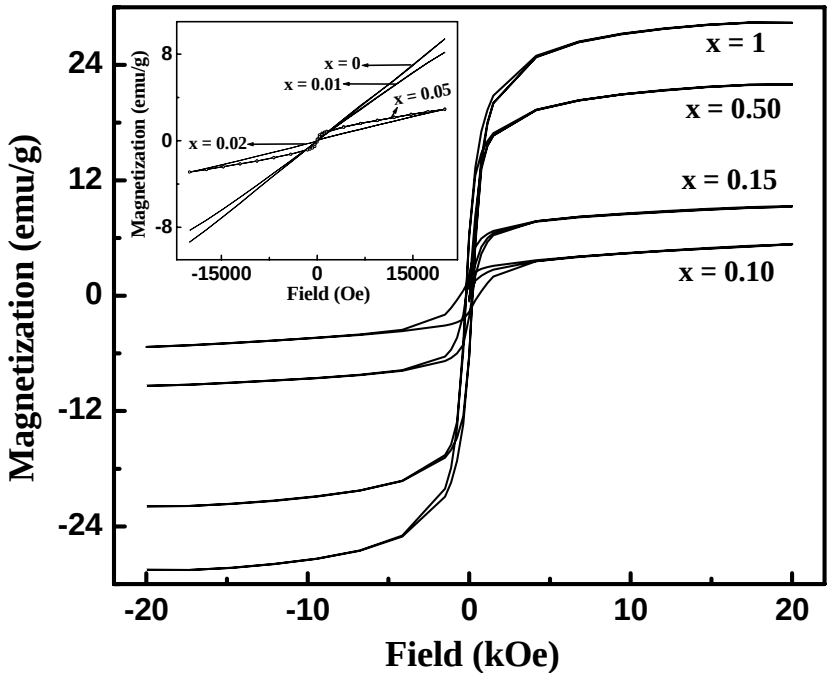

Fig. 4.26: Room temperature M-H plot of LCMO: NF composite ($x \geq 0.10$) annealed at 1123 K. Inset shows M-H loop of composite with $x \leq 0.05$ at room temperature.

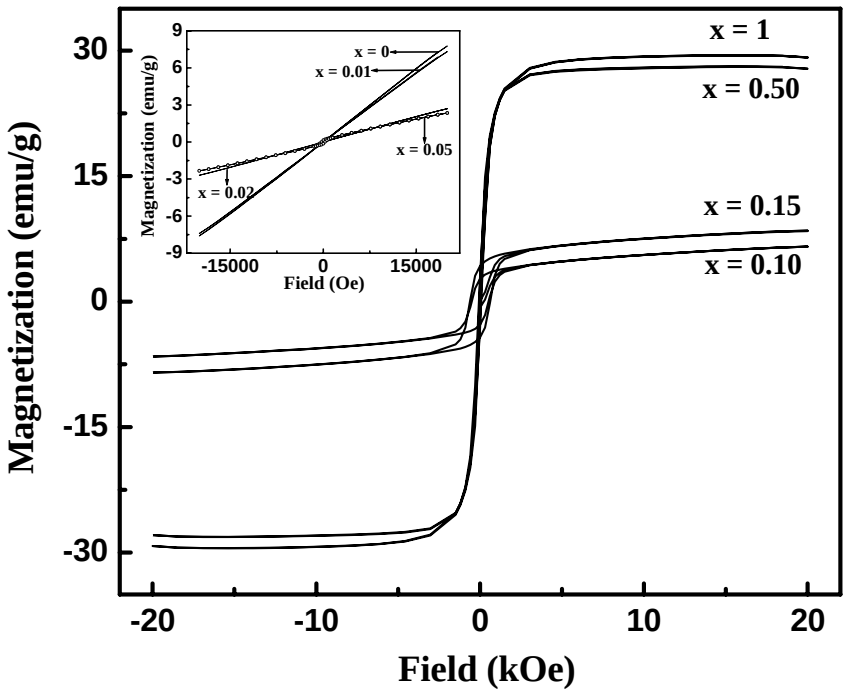

Fig. 4.27: Room temperature M-H plot of LCMO: NF composite ($x \geq 0.10$) annealed at 1473 K. Inset shows M-H loop of composite with $x \leq 0.05$ at room temperature.

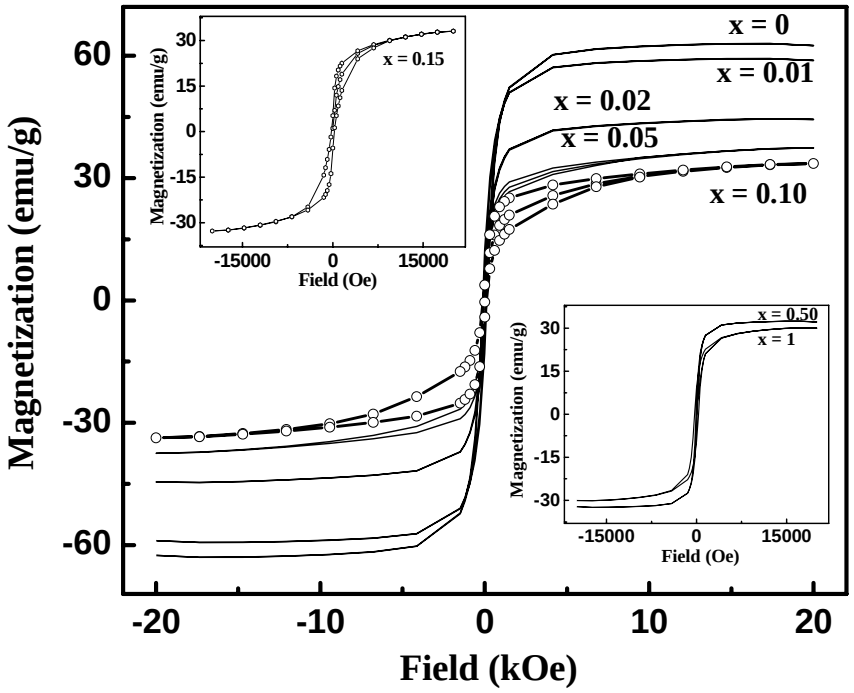

Fig. 4.28: Low temperature (at 85 K) M-H plot of the LCMO: NF composite ($0 \leq x \leq 0.10$) annealed at 1123 K. Inset shows M-H loop of composite with $x \geq 0.15$ at 85 K.

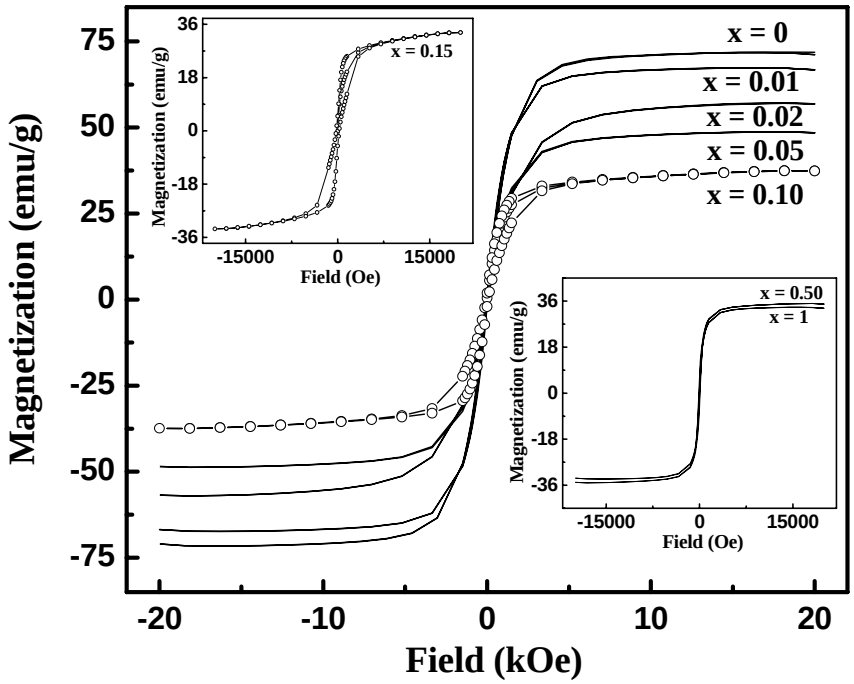

Fig. 4.29: Low temperature (at 85 K) M-H plot of the LCMO: NF composite ($0 \leq x \leq 0.10$) annealed at 1473 K. Inset shows M-H loop of composite with $x \geq 0.15$ at 85 K.

Fig. 4.30 shows the variation of coercivity (H_c) as a function of NF content in the composite LCMO: NF sintered at 1123K and 1473 K. At room temperature as well as low temperature (85 K) the behavior of H_c as a function of NF content is quite same. Both at room temperature as well as low temperature, the coercivity increases up to concentration x ~ 0.10 NF and then decreases. From the Table 4.7 and 4.8, it has been observed that there is a transition from hard (0.05 M ≤ x ≤ 0.15 M) to soft (x > 0.15 M) ferromagnetic behavior with increasing NF concentration at room temperature. At room temperature, the LCMO is paramagnetic while NF is ferrimagnetic. At 85 K, both LCMO and NF are magnetic. Hence, at room temperature LCMO and at low temperature both LCMO and NF play a role for enhancing the coercivity in the composite.

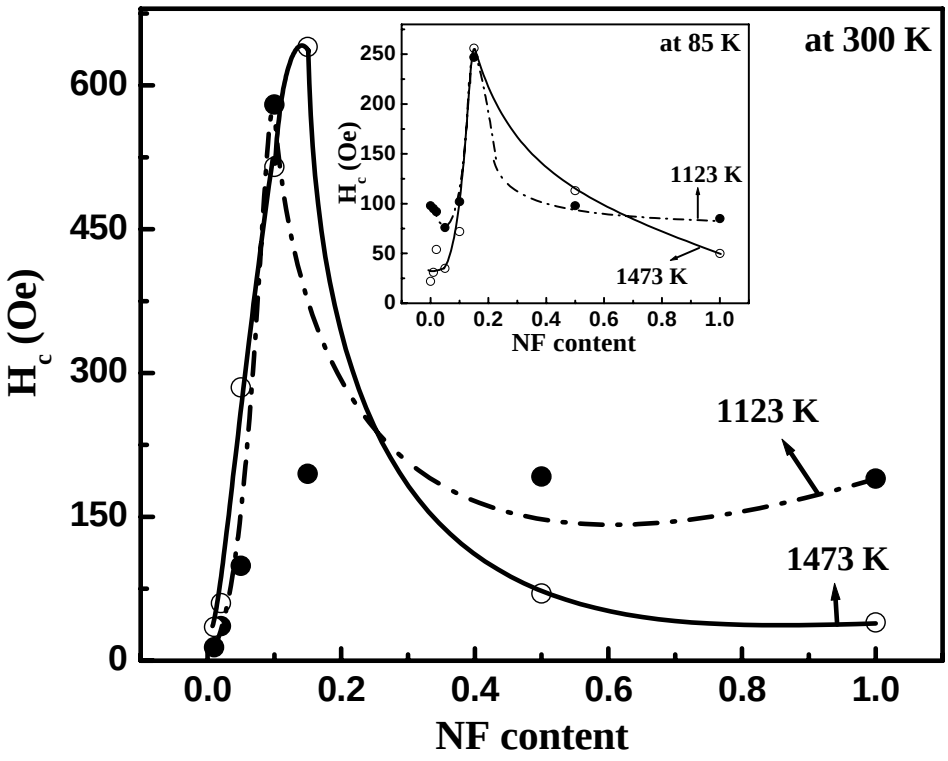

Fig. 4.30: Variation of coercivity (H_c) as a function of NF content at room temperature (300 K) in the composite LCMO: NF sintered at 1123 K and 1473 K. Inset shows H_c as a function of NF content at 85 K of these composites.

Table 4.7: The electrical and magnetic transition parameters of (1-x) LCMO: x NF composites heat treated at 1123 K. T_{MI} and T_C represent the insulator-metal and magnetic transition temperatures respectively.

x M NF	**Magnetization data**				**T_{MI}, K**	**T_{C1}, K LCMO**	**T_{C2}, K NF**
	At 300 K		**At 85 K**				
	M (emu/g) at 20 kOe	H_C (Oe)	M (emu/g) at 20 kOe	H_C (Oe)			
0	---	--	62.4	98	215	250	*
0.01	---	14	58.8	95	210	235	*
0.02	---	36	44.3	92	90	200	*
0.05	2.9	99	37.4	76	**	150	*
0.10	5.3	580	33.5	102	**	130	475
0.15	9.2	195	33.0	247	**	125	565
0.50	21.9	197	32.2	98	**	#	745
1.00	28.3	209	30.0	93	**	#	863

Table 4.8: The electrical and magnetic transition parameters of (1-x) LCMO: x NF composites heat treated at 1473 K. T_{MI} and T_C represent the insulator-metal and magnetic transition temperatures respectively.

x M NF	**Magnetization data**				**T_{MI}, K**	**T_{C1}, K LCMO**	**T_{C2}, K NF**
	At 300 K		**At 85 K**				
	M (emu/g) at 20 kOe	H_C (Oe)	M (emu/g) at 20 kOe	H_C (Oe)			
0	---	---	71.1	22	245.7/210	240	*
0.01	---	35	66.7	31	245/165	235	*
0.02	---	60	56.9	54	87	175	*
0.05	2.35	285	48.8	35	**	170	*
0.10	6.57	515	37.4	72	**	150	475
0.15	8.48	640	33.2	256	**	120	565
0.50	27.8	70	34.8	113	**	#	745
1.00	29.1	40	33.2	50	**	#	863

Note: ** T_{MI} not observed, # T_c of LCMO not observed, * T_c of NF not observed

T_c of LCMO (bulk value): 265 K

T_c of NF (bulk value): 858 K

The grain size reduction of LCMO and its distribution in a magnetic matrix affects the structural, transport and magnetic properties of manganites. The formation of orthorhombic and monoclinic forms of LCMO strongly depends on precursor solution pH and sintering temperatures. Monoclinic to orthorhombic phase transformation has been observed in LCMO: NF composites. The atomic tolerance factor increases with NF content due to substitution of Mn^{3+} ion by Fe^{3+} with lower ionic radii. This is responsible for the crystal structure transition. The volume of LCMO unit cell is found to increase with the addition of NF as seen from the data given in Table 4.4. This is probably due to the large size of Ni^{2+} and Fe^{3+} compared to Mn^{3+} and Mn^{4+} where the substitutions take place. The volume of pure LCMO unit cell in the present work is found to be $\sim$ 233.8 $Å^3$ and LCMO has an average grain size of $\approx$ 14 nm, determined from X-ray diffraction results. This unit cell value is nearly close to that observed for bulk LCMO wherein the grain size is of the order of several microns [105].

The phenomenon of colossal magnetoresistance in manganites is due to a combination of magnetic and electrical properties occurring simultaneously at the transition temperature. The double exchange process, which mediates these transitions, depends on external factors and is highly susceptible to processing conditions and chemical composition. In the case of LCMO (x = 0 M) the double exchange process is due to electron transport *via* Mn^{3+}- O^{2-} - Mn^{4+}. Addition of transition metal ions which substitute either the Mn^{3+} or Mn^{4+} are known to suppress the double exchange process and promote insulating, antiferromagnetic behavior. A double peak feature is observed in the transport behavior in case of LCMO (x = 0 M). Such 'double-peak' (one sharp peak near T_C and another broad peak below T_C) is attributed to the interplay of transport in the bulk and surface phase of doped manganate ceramics [80]. In systems where a nonmagnetic phase exits at the grain boundary surrounding the grains comprising of pure magnetic LCMO phases, the number of charge carriers and their mobility are expected to be determined by tunneling across the grain boundaries. This would account for the existence of the broad peak below T_{MI} [41]. In our case, the peak in ρ vs. *T* near T_{MI} is attributed to the CMR effect inside the grains while the broad peak below T_{MI} may be attributed to scattering at the grain boundary, which also accounts for the low temperature MR observed in these nanocomposites.

Yan et al. [8] and Huang et al. [29] have studied the effect of insulating, ferromagnetic (FM) phase on the magnetotransport and magnetic behavior of La-Sr-Mn-O, a colossal magneto resistive oxide similar to LCMO. They find that the presence of FM phase influences the magneto transport by magnetically coupling to the LSMO grains. The composites however

exhibit an insulator-metal transition even for insulating FM contents as high as 20 to 30 wt. % indicating a strong percolation induced conduction component. The results of the present work however show that lowering of electrical and magnetic transition temperatures is coupled with an increase in absolute resistivity with the addition of NF to LCMO. It clearly shows that the double exchange process in LCMO is severely affected. Ahn et al. [101] and Sun et al. [102] find that systematic substitution of Mn^{3+} by Fe^{3+} induces insulating, antiferromagnetic behavior. A substitutional doping with 0.18 Fe for Mn results in complete suppression of the transitions and an insulating behavior results. In the case of Ni doping a similar behavior, promoting insulating, antiferromagnetic state at the expense of metallic, ferromagnetic state is observed [103, 104]. At relatively low doping levels the ferromagnetic interactions such as $Mn^{3.5+\delta}$ - O^{2-} - $Ni^{2+}(Fe^{3+})$ and Mn^{3+} - O^{2-} - Mn^{4+} account for the weak transitions. At high doping levels, however, the antiferromagnetic super-exchange interactions, Mn^{4+} - O^{2-} - Mn^{4+}, Ni^{2+} - O^{2-} - Ni^{2+} and Fe^{3+} - O^{2-} - Fe^{3+} dominate resulting in an insulating, non-magnetic state. The presence of Ni- and Fe- salts in the precursor solution acts as a source of Ni- and Fe- ions for substituting Mn in LCMO in the present work. The reduction of T_C and T_{MI} observed for this nanometer grain of LCMO is possibly due to the increased surface effect that has been observed earlier but contrary to the enhancement in transition temperatures reported recently [105].

4.2.4 Summary

Microwave refluxing technique results in the formation of uniformly distributed nanograined composite of the two phases: magnetic La-Ca-Mn-O and insulating magnetic Ni-ferrite. It is not possible to make such composites by conventional ceramic or some chemical methods. The La-Ca-Mn-O phase however loses its negative magnetoresistance behavior due to a substitution of Mn with either Ni or Fe or both. The electrical transition is suppressed for $x > 0.02$ M NF while the magnetic transition is observed till $x = 0.15$ M NF. The nanograin size of the LCMO exhibits a significantly high grain boundary scattering, which leads to enhanced resistivity and a reduction in the temperature range of metallic behavior. This result in a lower critical value of Ni-ferrite for insulator-metal transition compared to the magnetic transition. These results clearly show that Mn substitution by Ni and Fe is more favored compared to the formation of pure La-Ca-Mn-O when all the cations are present. Above $x = 0.10$ M, however, the Ni-ferrite phase forms separately together with substituted La-Ca-Mn-O phase which is insulating and antiferromagnetic.

Chapter 5

Magnetic – Nonmagnetic Nanocomposite

This chapter describes the synthesis and characterization of CMR, $La_{0.67}Ca_{0.33}MnO_3$ (LCMO): SiO_2 (nonmagnetic insulator) nanocomposites prepared by glass-ceramic process with and without the addition of nucleating agents.

Structural, transport and magnetic properties of $La_{0.67}Ca_{0.33}MnO_3$ (LCMO): SiO_2 nanocomposites by glass-ceramic process

5.1 Introduction

Glass-ceramics are polycrystalline materials made by the controlled crystallization of glass. The materials normally have a crystalline content between 50 and 90 % by volume, the remainder being a residual uncrystallized glass phase [106]. An important feature of glass-ceramic is their fine-grained microstructure achieved by the inclusion of a nucleating agent and by control of the crystal growth process [107]. Therefore most important step in the synthesis of glass-ceramics is controlled crystallization and this involves the subjection of glass to a carefully regulated heat-treatment cycle. Selection of glass composition is crucial to ensure that a high rate of internal, rather than surface, nucleation occurs and that crystal growth takes place at a sufficient rate to avoid deformation of the material during heat treatment.

The chemical compositions glass-ceramics are chosen to ensure precipitation of crystal phases that will confer desired properties to the final glass-ceramic. Control of the crystallization process is achieved first by the inclusion of nucleating agent, to ensure that crystallization is initiated throughout the whole volume of the glass, and secondly by the inclusion of certain minor constituents which favorably modify crystal growth rates. Nucleating agents that are employed include Sb_2O_3, Cr_2O_3, TiO_2, ZrO_2, P_2O_5 or in some cases mixture of these. Crystal growth rate modifiers include alkali-metal oxides, alkaline-earth oxides and boric oxide.

In the present work, the glass-ceramic technique is used to engineer the microstructure to produce a manganite ($La_{0.67}Ca_{0.33}MnO_3$) / non-magnetic insulator (silicates / SiO_2) composite. The size and volume fraction of the ferromagnetic manganite phase is controlled by nucleation with different nucleating agents. In order to enhance glass formation in the as-prepared state, B_2O_3 which is known to promote glass formation has been used. Sb_2O_3 and Cr_2O_3 have been used as effective nucleating agents in a variety of systems ranging from ferrites to high temperature superconductors. Hence, about 1 mole % of these oxides have been used in the present work to study their effectiveness in preferentially nucleating the LCMO phase. The magnetic and electrical properties of the resulting nanocomposites have been studied as a function of temperature and external magnetic field. These results are discussed in relation to the microstructure of the composites.

5.2 Selection of composition

The initial composition is crucial because it should be able to form a glass on simple quenching of the melt and at the same time should have all the elements needed to form the LCMO phase on heat treatment. Hence, the initial raw materials chosen are as follows: high purity La_2O_3, $CaCO_3$, Mn_2O_3, SiO_2, and B_2O_3 powders together with or without the nucleating agents, Sb_2O_3 and Cr_2O_3. The exact compositions selected for preparing the manganite ($La_{0.67}Ca_{0.33}MnO_3$) / non-magnetic insulator (silicates / SiO_2) composite in the present work are given in Table 5.1.

Table 5.1: Compositions selected for preparing LCMO: SiO_2 nanocomposite by the glass-ceramic process. (All compositions are in mol %)

Material	**Composition I**	**Composition II**	**Composition III**	**Composition IV**	**Composition V**
LCMO (Equivalent)	45	54	55	60	70
SiO_2	5	10	5	5	5
B_2O_3	49	35	39	35	25
Nucleating agent (NA)	1 (Sb_2O_3)	1 (Sb_2O_3 or Cr_2O_3)	1 (Sb_2O_3)	---	---
Holding temperature (K)	1523	1523	1523 and 1723	1523	1523

5.3 Experimental details

The glass-ceramic composite, $La_{0.67}Ca_{0.33}MnO_3$: SiO_2, was prepared by a two step process. In the first step high purity La_2O_3, $CaCO_3$, Mn_2O_3, B_2O_3 and SiO_2 powders together with or without the nucleating agents as per compositions in Table 5.1 were thoroughly mixed mechanically for several hours and melted. After melting, the molten mass was quenched between two steel plates to form flakes of the composite. The quenched flakes were powdered and the powder was treated with hot acetic acid to remove the glass forming borate

component and thus enrich the manganite component. In the second step, the resulting LCMO: SiO_2 composite powder was pressed into pellets and heat-treated in air at different temperatures.

The microstructural characterization was done using a combination of x-ray diffraction and transmission electron microscopy. The magnetization as a function of temperature T and external magnetic field H was studied using a vibrating sample magnetometer. The d.c. electrical resistivity of the composites was measured in the temperature range 80-300 K using the standard linear array four probe technique.

5.4 Results and discussion

Among the five different compositions selected in the present work, Table 5.1, it was observed that compositions IV and V formed a high viscosity low fluidity melt at 1523 K. This is because of the amount of B_2O_3, the low melting oxide, was very low and LCMO equivalent compounds were high compared to other compositions. So composition IV and V are not discussed any more in this work. To get a high fluidity, low viscosity melt, a high holding temperature of 1723 K was used to process composition III. The composites without nucleating agent and with Sb_2O_3 and Cr_2O_3 as nucleating agent is denoted as LCM, LCM Sb and LCM Cr respectively in this work.

5.4.1 Structure and microstructure

The presence of various phases in the composites at different stages of processing was determined by X-ray diffraction. Fig. 5.1 (a) shows the X-ray diffraction pattern of as prepared composite of composition I.

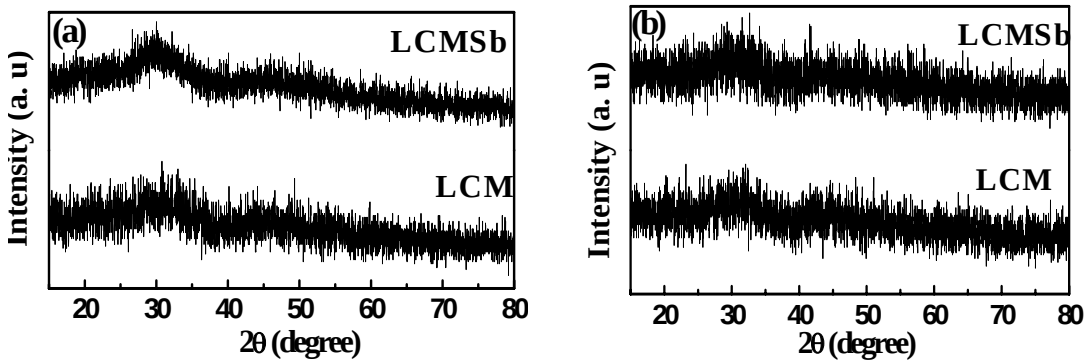

Fig.5.1: X-ray diffraction pattern of (a) the as prepared glass and (b) after etching with hot acetic acid for both LCM and LCM Sb sample of composition I.

The powder of the as prepared samples of composition I was etched with hot acetic acid to remove the glass forming borate component. The etching was done for 15 minutes each time and for three times. A total of about 30 - 40 % weight loss was observed after three etching cycles. Fig. 5.1 (b) shows the X-ray diffraction pattern of as prepared glass powder of composition I after etching with hot acetic acid. In both the cases before and after etching, the composite samples indicate the presence of glassy phase in the composite.

After etching, the composition I was heat-treated at different temperatures to nucleate the LCMO phase from the glassy matrix. Fig. 5.2 (a), (b) and (c) show the X-ray diffraction patterns of composition I heat-treated for 2 hours at 773 K, 873 K and 1073 K respectively.

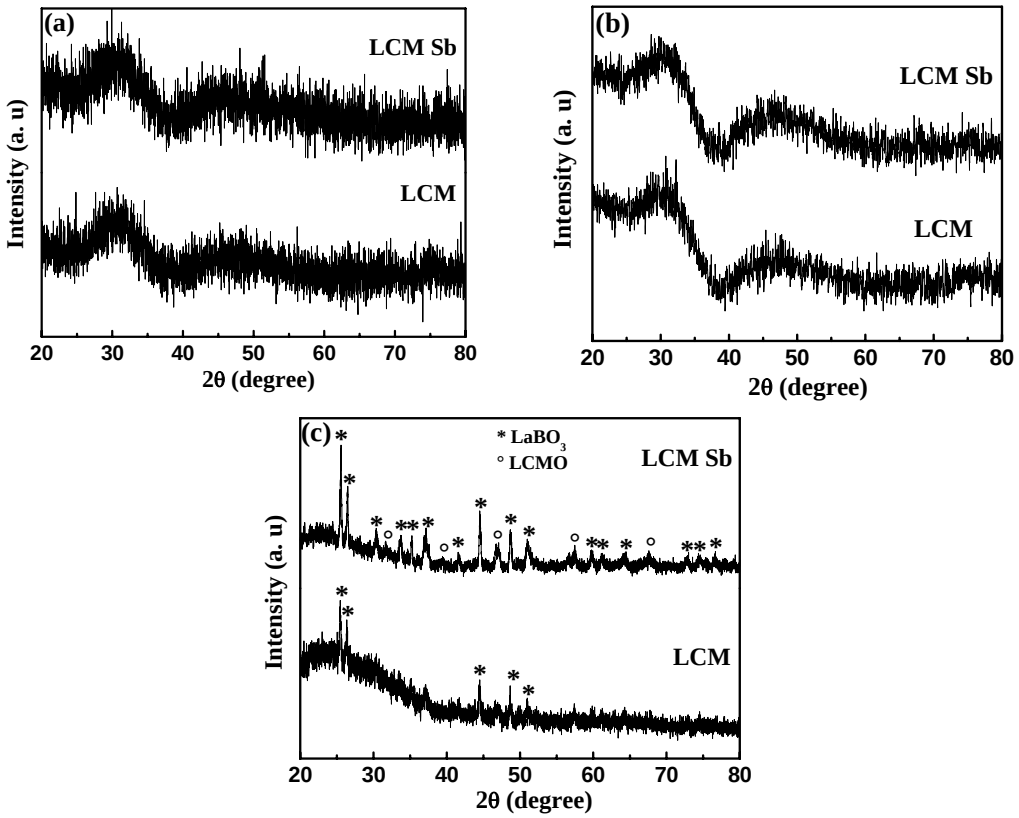

Fig. 5.2: X-ray diffraction pattern of composition I (after etching) heat-treated at (a) 773 K (b) 873 K and (c) 1073 K for 2 hours.

From the XRD pattern, it was observed that LCMO phase does not crystallize up to 873 K. At a higher temperature (at 1073 K), $LaBO_3$ phase is formed due to reaction of LCMO equivalent compounds with higher amount of B_2O_3. It is also seen that at this temperature small amount of LCMO is formed with the addition of nucleating agent Sb_2O_3, which helps in nucleating the LCMO phase by suppressing the secondary $LaBO_3$ phase. Hence, composition

II and III are chosen for further studies for preparation of this composite where the amounts of LCMO equivalent materials have been increased compared to composition I.

Fig. 5.3 (a) shows the X-ray diffraction pattern of the as prepared composite of composition II. In the case of LCM, the as prepared composites contain LCMO phase with very small amount of secondary phase, $LaBO_3$ where as in the case of LCM Sb and LCM Cr the XRD clearly shows the presence of only crystalline LCMO phase in a glass matrix.

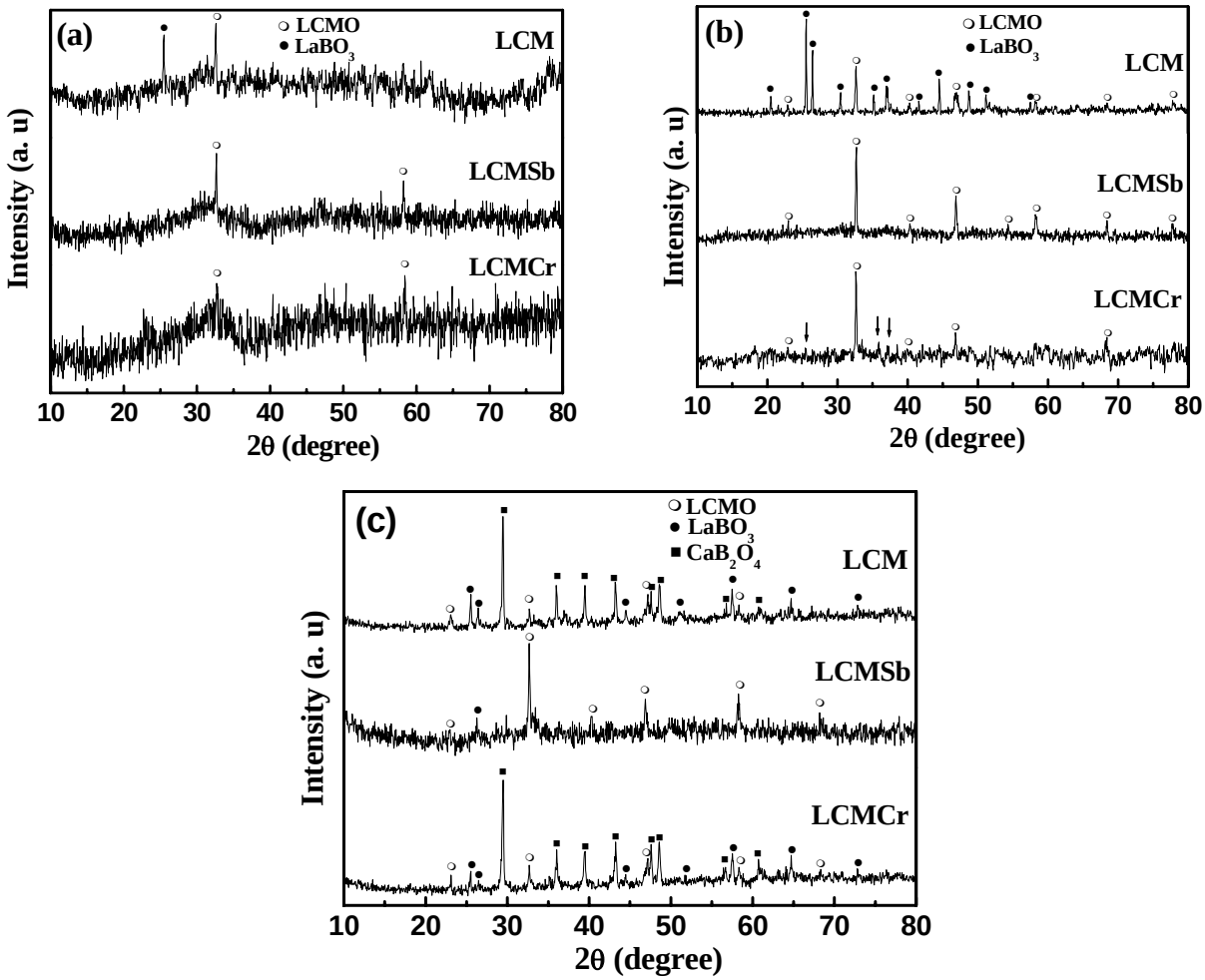

Fig. 5.3: The x-ray diffraction pattern from as-prepared composites of composition II, (a) shows the presence of crystalline peaks together with the amorphous phase. After etching the B_2O_3 based phase, (b) and annealing the resulting powder at 1173 K for 8h, (c) the crystalline fraction increases considerably. Arrow indicates the position of $LaBO_3$ phase.

The three composites LCM, LCM Sb and LCM Cr show the formation of glass-ceramic in the as prepared state itself. After Etching with hot acetic acid however the volume fraction of LCMO phase increases in all the composites. The composition without the nucleating agent and with Cr_2O_3 as nucleating agent show the presence of $LaBO_3$ phases

together with LCMO after etching while in Sb_2O_3 nucleated sample only the LCMO phase is seen, Fig. 5.3(b). These results clearly show that Sb_2O_3 is a good nucleating agent for the LCMO phase when compared to Cr_2O_3. It can be said that Sb_2O_3 primarily suppresses the formation of other secondary phases leading to preferential nucleation the LCMO phase. Annealing the etched powder at 1173 K for 8 hours results in the nucleation and / growth of other crystalline phases, excepting the case where Sb_2O_3 was used as nucleating agent, Fig. 5.3(c). These heat-treated samples were characterized further to study the electrical and magnetic properties.

In this composition II, formation of glass-ceramic instead of glass in the as-quenched state itself indicates a low nucleation barrier. Hence, composition III is chosen where the glass-forming component B_2O_3 was increased. For better homogeneity of the LCMO phase in the glassy matrix in this composite, the initial batch of composition III was melted and quenched from a higher temperature (at 1723 K).

Fig. 5.4 (a) and (b) show the X-ray diffraction pattern of the as prepared composite of composition III melted and quenched from 1523 K and 1723 K respectively. A higher holding temperature of 1723 K gives more homogeneity, low viscosity and high fluidity melt. Hence, the glassy phase is more in the composite prepared from melt at higher temperature, which can be seen from Fig. 5.4 (b). The composites show LCMO and glassy phase in both the case with no secondary phase of $LaBO_3$.

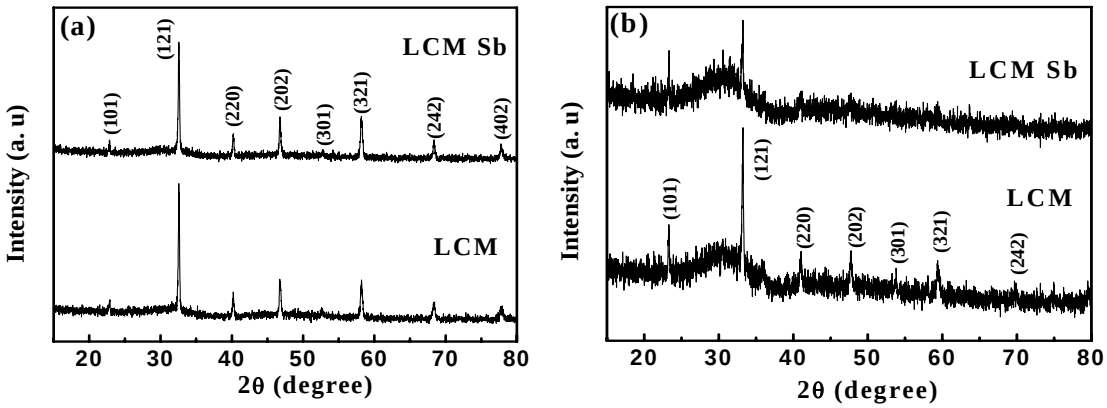

Fig. 5.4: X-ray diffraction pattern of as prepared composite of composition III melted and quenched from (a) 1523 K and (b) 1723 K.

After etching with hot acetic acid, the volume fraction of LCMO phase increases due to decrease of borate containing phase. Fig. 5.5 (a) and (b) show the X-ray diffraction pattern of composites (after etching with hot acetic acid) of composition III melted and quenched

from 1523 K and 1723 K respectively. There is still high amount of glassy phase present for composites melted and quenched from 1723 K.

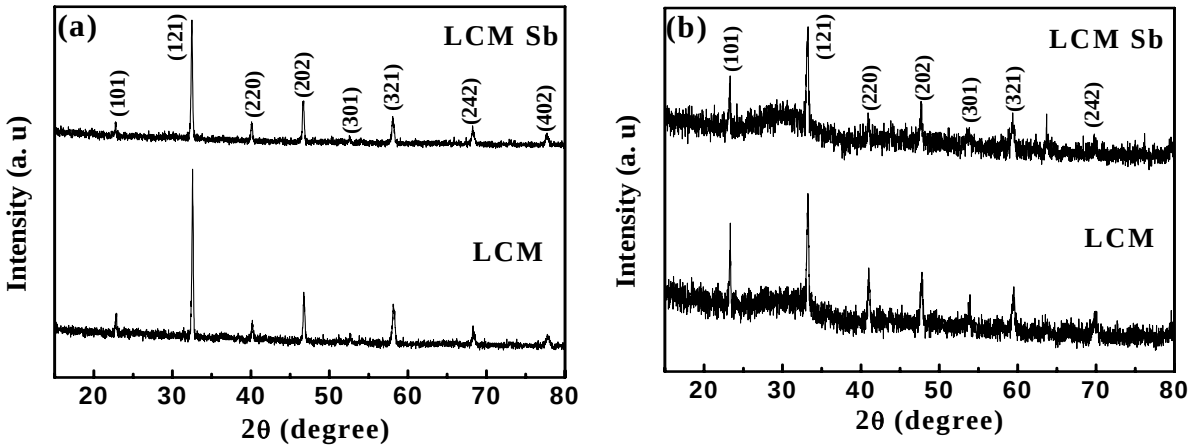

Fig. 5.5: X-ray diffraction pattern of as prepared composite after etching with hot acetic acid of composition III melted and quenched from (a) 1523 K and (b) 1723 K. The indices corresponding to LCMO phase.

Heat-treatment of composites of composition III was done at different temperatures so that growth of LCMO phase should take place. Fig. 5.6 (a) and (b) show the X-ray diffraction pattern of composites (heat-treated at 923 K for 2 hours) of composition III melted and quenched from 1523 K and 1723 K respectively. The electrical and magnetic properties of these samples were studied in detail.

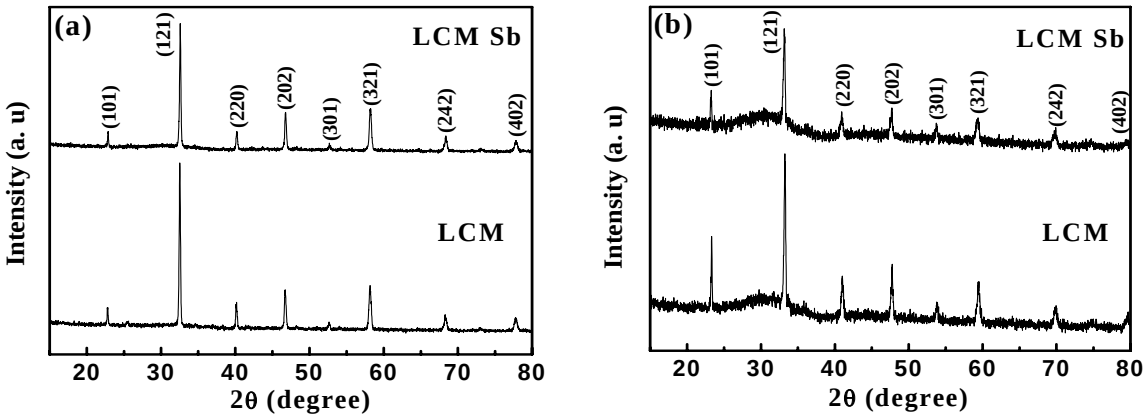

Fig. 5.6: X-ray diffraction pattern of composite (heat-treated at 923 K for 2 hours) of composition III melted and quenched from (a) 1523 K and (b) 1723 K.

At higher annealing temperature of 1123 K, the composite of composition III has LCMO phase along with secondary phase of $LaBO_3$ as seen from the X-ray diffraction pattern in Fig. 5.7. It has been observed that LCM Sb sample shows negligible amount of $LaBO_3$

phase compared to LCM sample. This shows that the nucleating agent Sb_2O_3 suppresses the secondary phase and simultaneously helps in nucleation of the LCMO phase in the composite.

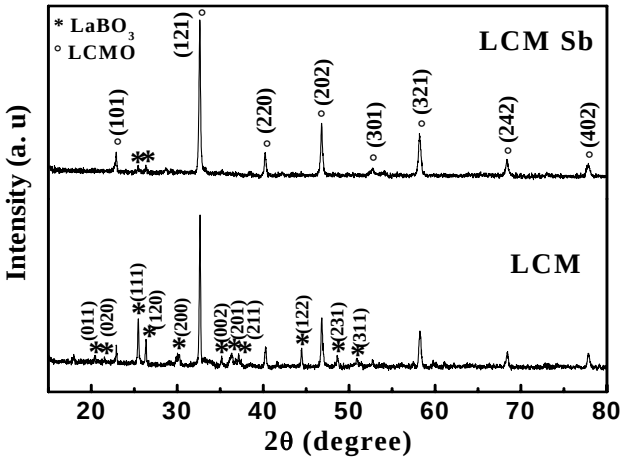

Fig.5.7: X-ray diffraction pattern of LCM and LCM Sb samples of composition III (melted and quenched from 1523 K) heat-treated at 1123 K for 1hour.

The grain size of LCMO in the composites was determined from FWHM of different peaks using the Scherer relation and is found to be in the range 30 nm – 50 nm prior to annealing treatment. At higher annealing temperature (at 1173 K), the grain size was not found to increase significantly indicating a resistance to grain growth. This is plausibly due to the limited diffusional kinetics available to the system to effect long range rearrangement of several elements, required for significant grain growth to occur for the LCMO phase.

Transmission electron microscopy together with selected area diffraction of the etched powders of composition II show a glass-ceramic two phase structure in all the cases, with and without the nucleating agent. A typical bright field image together with the diffraction pattern is shown in Fig. 5.8. The diffraction pattern shows a diffuse ring superimposed with the crystalline pattern indicating the presence of a glass-crystalline two phase structure both before and after etching the powders. The crystalline diffraction pattern becomes clear after etching the powder with acetic acid clearly showing that the etching process removes the borate based glassy phase. The silicate rich glassy phase however cannot be removed with acetic acid etching and remains with the LCMO crystals as a non-magnetic constituent.

The grain size is found to be < 100 nm, in agreement with the grain size determined from X-ray diffraction peaks. The X-ray diffraction and electron microscopy results show that LCMO crystalline phase has a low nucleation barrier and hence is difficult to suppress its formation in the as-quenched stage. However, it has a significant resistance to grain growth

due to long range diffusional constraint of several elements. The liquid mixture has a strong chemical segregation behavior prior to liquid quenching which leads to the formation of a multi-phase composite structure in the solid state except when Sb_2O_3 is present as a nucleant.

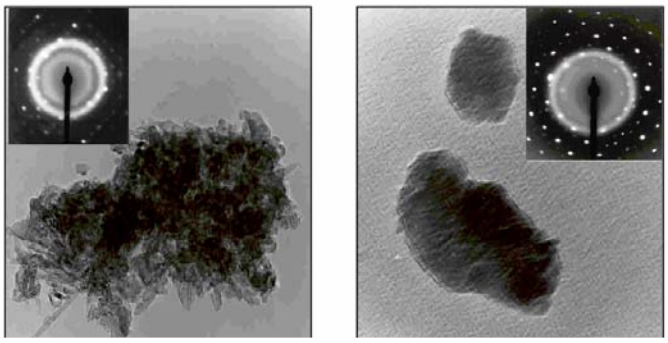

Fig. 5.8: Bright field transmission electron micrograph of the composite powder of composition II before (a) and after (b) etching the B_2O_3 based phase shows a mixture of crystalline and glassy phase. The amount of glassy phase after etching however is decreased revealing the crystalline pattern clearly. The inset shows the selected area diffraction pattern from the composite.

Fig. 5.9 (a) and (b) show the dark field TEM micrographs of LCM and LCM Sb sample respectively for composite of composition III heat-treated at 923 K, where LCMO phase with no secondary phase is observed (see Fig. 5.6). TEM micrographs show that the LCMO crystalline phase is embedded in a glassy phase. From the dark field image, the grain size of LCMO is found to be in the range of 15 to 30 nm, which is an agreement with the XRD results. The phases present and grain size obtained from the XRD as well as TEM results for all composites with different compositions are given in Table 5.2.

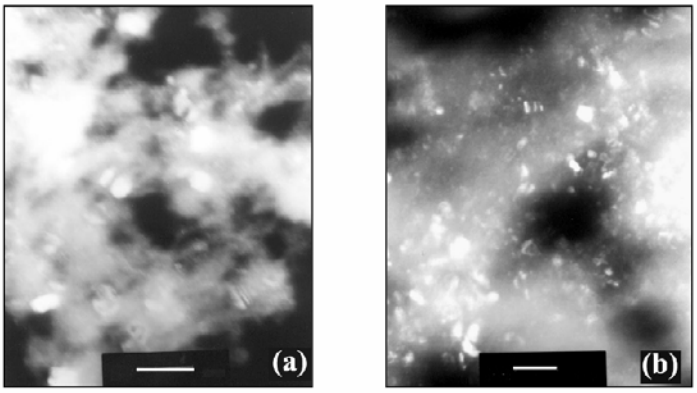

Fig.5.9: Dark field TEM micrographs of (a) LCM and (b) LCM Sb sample of composition III heat-treated at 923 K. Scale corresponds to 100 nm in all the cases.

Table 5.2: Phases present and grain size obtained from XRD as well as TEM for samples of all compositions.

Samples	**Phases Present**			**Size (in nm) after heat-treatment**	
	As prepared	After Etching	After heat-treatment	XRD	TEM
Composition I			Amorphous Up to 923 K		
LCM	Amorphous	Amorphous	Major $LaBO_3$ + minor LCMO phase at 1073 K	----	----
LCM Sb	Amorphous	Amorphous	Major $LaBO_3$ + minor LCMO phase at 1073 K		
Composition II					
LCM	LCMO + $LaBO_3$	LCMO + $LaBO_3$	LCMO + $LaBO_3$ + CaB_2O_4	Grain size: 30 to 50	Particle size around 100
LCM Sb	LCMO	LCMO	LCMO + $LaBO_3$		
LCM Cr	LCMO + $LaBO_3$	LCMO + $LaBO_3$	LCMO + $LaBO_3$ + CaB_2O_4		
Composition III Melted and quenched from 1523 K (Both LCM and LCM Sb sample)	LCMO + less amount of glassy phase	LCMO	LCMO phase upto 923 K LCMO + $LaBO_3$ phase at 1123 K	Grain size: 30 to 50	Grain size: 15 to 30
Composition III Melted and quenched from 1723 K (Both LCM and LCM Sb sample)	LCMO + more amount of glassy phase	LCMO + glassy phase	LCMO + glassy phase upto 923 K	----	----

5.4.2 Electrical transport

The electrical resistivity (ρ) of the etched and heat treated composites of composition II was studied in the temperature range 80 K – 300 K in zero external magnetic field and the results are shown in Fig. 5.10.

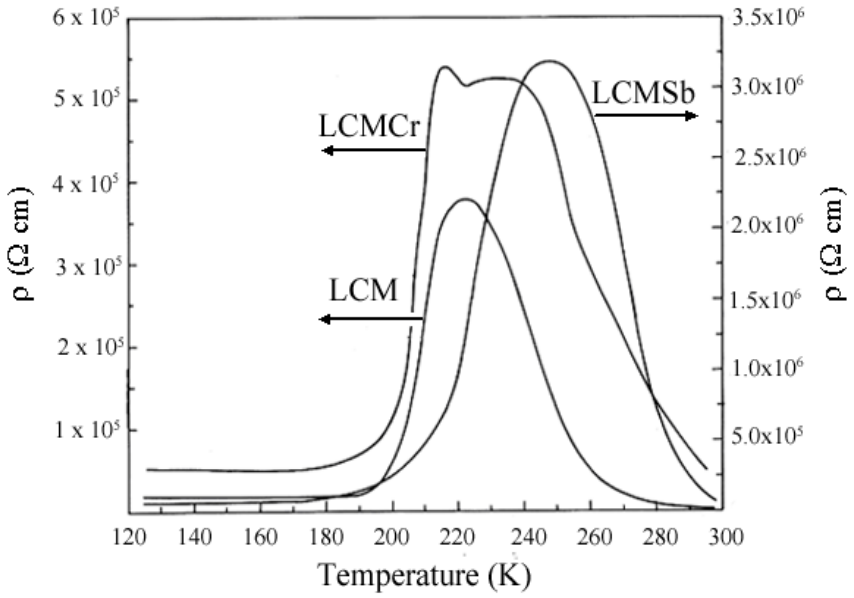

Fig.5.10: The electrical resistivity of composition II shows a clear metal-insulator transition in spite of the composite nature of the microstructure. The absolute value of the resistivity however is high compared to bulk LCMO.

In all the cases, a clear metal to insulator transition occurs at a transition temperature T_{MI}. The T_{MI} in all the cases again is lower compared to pure, bulk LCMO which has a T_{MI} of 270 K and the width of the transition is also found to be large. The absolute resistivity is found to be higher by about 5 orders of magnitude compared to bulk LCMO. The high resistivity, low and broad transition temperatures are in agreement with the microstructural results, which show the presence of nanocrystalline multi-phases [108]. An interesting feature observed in the present work is the presence of a double peak in the resistivity at ≈ 230 K and 215 K in Cr_2O_3 nucleated LCMO. Such behavior has been observed earlier in Cr substituted La-Ca/Sr-Mn-O and has been attributed to two double exchange processes – Mn^{4+}-O-Mn^{3+} and Mn^{4+}-O-Cr^{3+} taking place in these substituted systems [109, 110]. The presence of this feature shows that Cr_2O_3 acts as a substitutional addition and not just a nucleating agent. The resistivity data of composites II are given in Table 5.3.

The resistivity of the composites of composition III could not be measured due to high resistance at room temperature of the order of 10^6 Ωcm. The resistance is high due to the presence of well separated LCMO phase distributed in a glassy matrix as seen from the TEM micrographs (Fig. 5.9). Also from the XRD pattern, it was observed that glassy phase is not completely removed from the composites even after etching with hot acetic acid. From these microstructural results, it can be concluded that the glassy phase of borate or silicate has an insulating behavior, which leads to a lack of electrical conductivity between the metallic LCMO grains.

5.4.3 Magnetization

The variation of magnetization M with external field H of heat-treated composites of composition II was studied at 5 K up to 6.0 T and the results are shown in Fig. 5.11 (a)-(c).

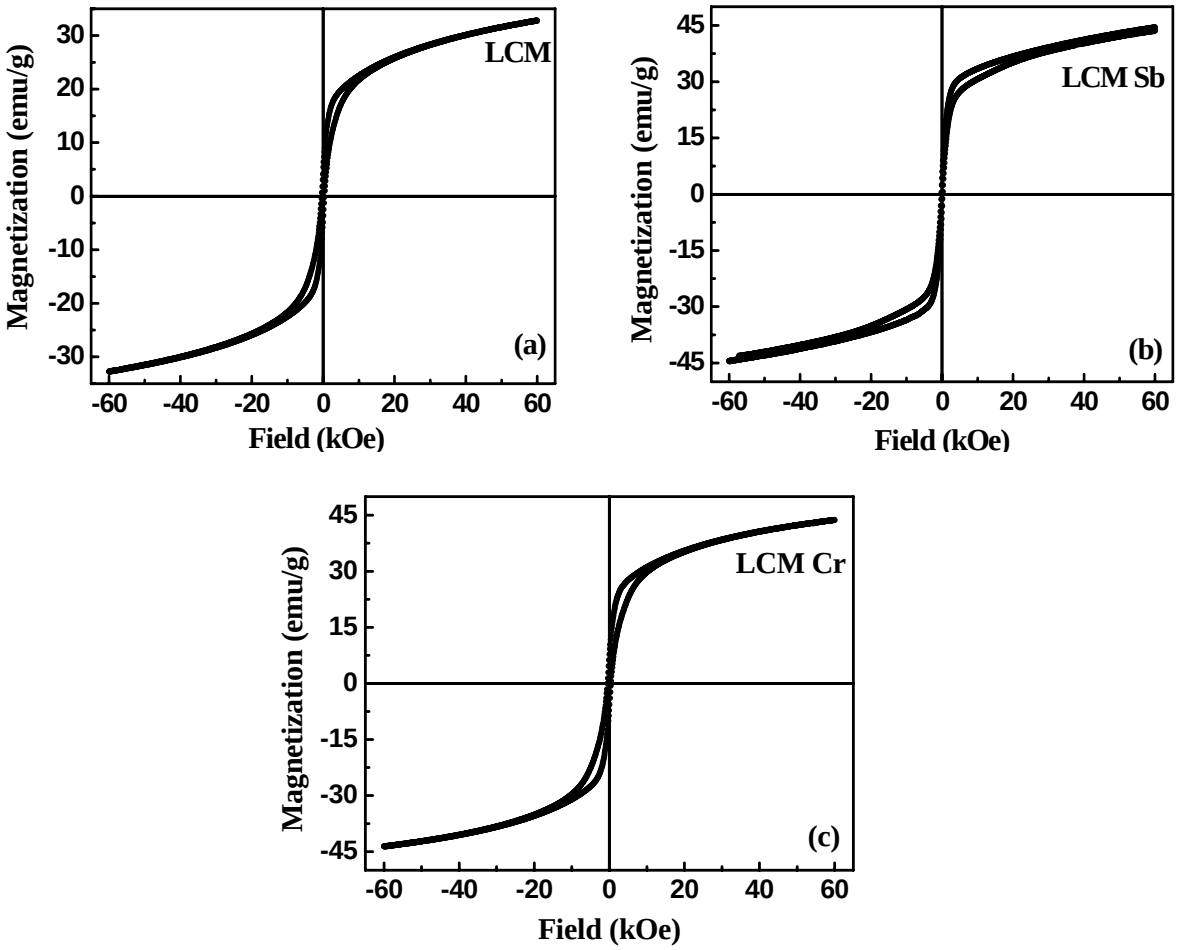

Fig. 5.11: The magnetic hysteresis at 5.0 K shows a typical soft magnetic behavior with low coercivity in the composites without (a) and with (b) and (c) the nucleating agents Sb_2O_3 and Cr_2O_3 respectively for samples of composition II. Note that the magnetization does not reach saturation in all cases even at 6.0 T field.

All the three samples (with and without nucleating agents) do not show true saturation even at external fields of the order of 6.0 T, an indication of the presence both paramagnetic and ferromagnetic behavior. These non-saturating behaviors are due to the presence of LCMO nanocrystals distributed in a borate or silicate glassy matrix in the composites as seen from the microstructural results. However, coercivity and remanence are observed which would indicate that the composites behave as a ferromagnetic material at 5 K. The H_c and M_r values are found to be lowest when LCMO was nucleated by Sb_2O_3, 200 G and 4.3 emu g^{-1} while they were highest for Cr_2O_3 nucleation, 400 G and 6.85 emu g^{-1}, respectively. These values are higher compared to the values for bulk monophasic LCMO [111]. This type of behavior is observed when the magnetic disorder is high. The magnetic disorder provides sites for pinning which result in increasing the coercive fields, H_c.

The variation of magnetization M with temperature T of heat-treated composites of composition II in an external field of 0.5 T shows a typical ferromagnetic behavior in all the cases and is shown in Fig. 5.12. The non-magnetic to magnetic transition temperature, T_C is found to be different and smeared compared to pure LCMO and is given in Table 5.3. The LCMO phase nucleated by Sb_2O_3 has the lowest T_C of 210 K while it is 244 K and 265 K respectively for the Cr_2O_3 nucleated and the base composition. These values are lower than ≈ 270 K reported for the pure bulk LCMO phase and also the transition range is large in the present case. It is worth noting here that although Sb_2O_3 nucleation leads to the formation of only the LCMO phase the T_C value for this is the lowest at 210 K compared to bulk LCMO determined from magnetization studies. Another feature in the magnetization M is a kink with an upward turn at T ≈ 50 K.

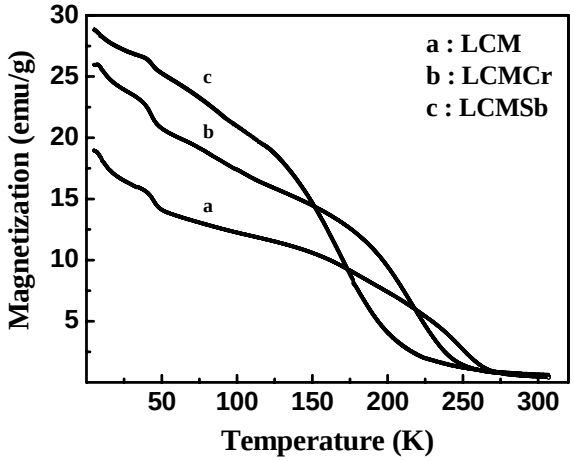

Fig. 5.12: The variation of magnetization M with temperature T for composition II sample in the presence of 0.5 T field shows a clear non-magnetic to magnetic transition independent of the presence of nucleating agents. The magnetization has an upward turn for T < 50 K in all the cases and is discussed in the text.

Fig. 5.13 (a) and (b) shows the variation of magnetization M with external field H at 85 K of heat-treated composites of composition III melted and quenched from 1523 K and 1723 K respectively. Composites quenched from 1523 K show a soft magnetic behavior with nearly saturating behavior. Both LCM and LCM Sb composites show a magnetization value of 42 emu /g and 47 emu /g respectively at 85 K and 20,000 Oe. The magnetization values are less compared to bulk LCMO value and are due to the presence of insulating glassy phase in these composites. When the composites are quenched from 1723 K, the non-saturating behavior increases and shows paramagnetic nature with very small ferromagnetic behavior. As seen from the XRD pattern (Fig. 5.6), the glassy phase is more when the melt is quenched from 1723 K when compared with a quenching temperature of 1523 K. Due to this glassy insulating phase, the magnetization values of LCM and LCM Sb samples are an order of magnitude lower than the composites quenched from 1523 K.

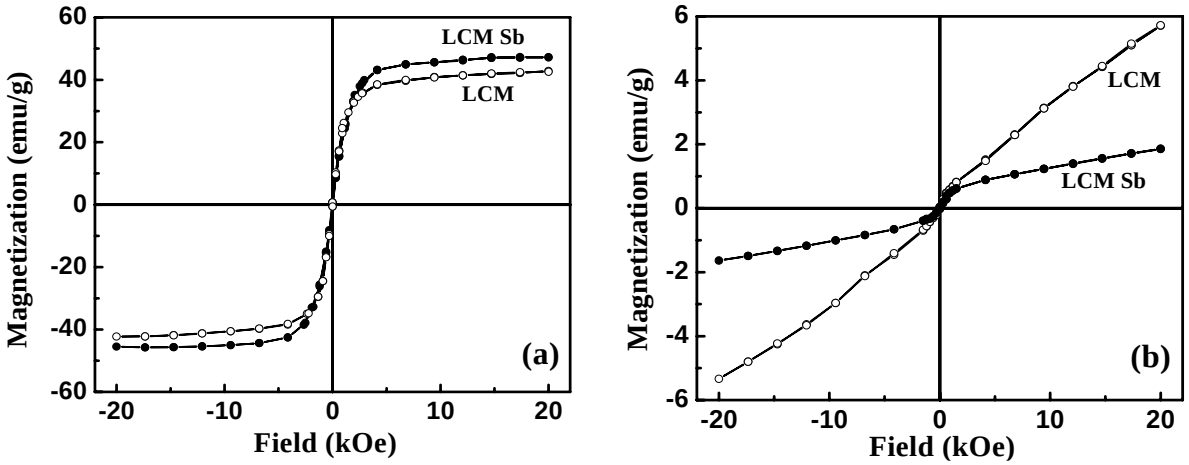

Fig. 5.13: The magnetic hysteresis at 85.0 K shows a typical soft magnetic behavior with low coercivity in the composites of composition III melted and quenched from (a) 1523 K and (b) 1723 K for two samples LCM and LCM Sb

Fig. 5.14 (a) and (b) show the variation of Magnetization M with temperature T (with an external field of 100 Oe) of heat-treated composite of composition III melted and quenched from 1523 K and 1723 K respectively. Composite LCM and LCM Sb (Fig. 5.14 a) show a smooth transition from ferromagnetic to paramagnetic state at around 250 K and 225 K respectively. In this case, LCM sample shows a broad transition compared to LCM Sb sample. Whereas, composites LCM and LCM Sb (Fig. 5.14 b) obtained after quenching from 1723 K, show two sharp transitions at around 250 K and 180 K. The two transitions may be indicating the presence of two-phase magnetic system in the composite. However, there is no other

phases present except LCMO phase in this composite as seen from the microstructural studies. The magnetization data of these composites are given in Table 5.3.

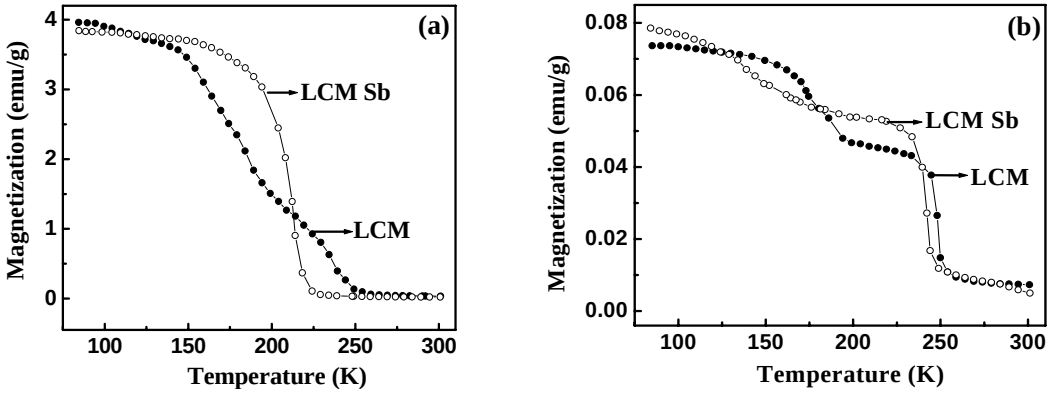

Fig.5.14: Variation of Magnetization M with temperature T at 100 Oe of heat-treated composites of composition III melted and quenched from (a) 1523 K and (b) 1723 K.

Table 5.3: The electrical and magnetization data of heat-treated composites with composition II and III. T_c is the magnetic transition temperature, H_c the coercive field, M is the magnetization, T_{MI} the electrical transition temperature and ρ the room temperature resistivity. LCM, LCMSb and LCMCr are compositions without nucleating agent, with Sb_2O_3 and Cr_2O_3 as nucleating agents respectively.

Composition	Sample	T_c (K)	H_c (Oe)	M (emu/g) at 5 K, in a field of 5000 Oe	T_{MI} (K)	ρ (Ωcm) at 300 K
II	LCM	265	391	19	223	4.8×10^3
	LCM Sb	210	207	29	253	7.2×10^4
	LCM Cr	244	451	26	215 / 228	8.6×10^4
				M (emu/g) at 85 K in a field of 20 kOe		
III (melted and quenched from 1523 K)	LCM	250	18	43	---	---
	LCM Sb	225	21	47	---	---
III (melted and quenched from 1723 K)	LCM	250 / 180	27	6	---	---
	LCM Sb	250 / 180	35	2	---	---

The electron transport and magnetic behavior of LCMO depends critically on factors such as oxygen concentration, substitutional doping, absolute grain size and the presence of non-magnetic, insulating phases [112, 113]. For the first time Müller et. al. [30, 31] prepared (LaSr)MnO_3 powders with perovskite structure in the basic system MnO_2–SrO–La_2O_3–B_2O_3 by a modified glass crystallization method. The magnetic properties of the powders are comparable with the properties of LSMO single crystals. They have however not studied the effect of any nucleating agent on these manganites. The presence of an efficient nucleating agent, the determination of the temperature and time of nucleation and growth acquire particular importance in the formation of glass-ceramic composite.

In the present work, the effect of nucleating agents e.g. Sb_2O_3 and Cr_2O_3 on the structural, transport and magnetic properties of LCMO: SiO_2 nanocomposites have been studied through glass-ceramic route. From the X-ray diffraction, it has been observed that LCMO phase formation takes place in the as quenched state itself indicating, a low nucleation barrier. It indicates that Sb_2O_3 and Cr_2O_3 play a more active role than merely aiding the process of nucleation of the crystalline phase. In the present work, the effect of nucleating agents, Sb_2O_3 and Cr_2O_3 on the transport and magnetic properties is remarkable as compared with non-nucleated LCMO. Sb_2O_3 is found to inhibit the nucleation of crystalline phases other than LCMO while Cr_2O_3 has no effect on the nucleation behavior of the various phases. The microstructural results show that LCMO phase is well distributed in the glassy matrix in all the composites. Due to lack of connectivity between LCMO grains, the composites show high resistivity (~10^5 Ωcm) at room temperature. Highest T_{MI} and T_c are found in case of Sb_2O_3 nucleated sample compared with Cr_2O_3 and non-nucleated LCMO. Form the structural, transport and magnetic properties, it is found that LCMO phase is highly disordered in the glassy matrix.

The absolute amount of LCMO phase to be present in the various samples can be determined from a simple mass balance approach and according to this after etching away the glass forming B_2O_3 phase the LCMO phase fraction is found to increase from 54 % to 84 %. The theoretical value of magnetization corresponding to this amount of LCMO phase should be ≈ 75 emu g^{-1}. In the present work, however the maximum value of magnetization is found to be only ≈ 29 emu g^{-1} for Sb_2O_3 nucleated sample for composition II where as for composition III, the magnetization is 47 emu/g. These results clearly show that the equivalent volume of LCMO phase is about ≤ 30 and ≤ 50 % for compositions II and III respectively and the rest comprises of non-magnetic SiO_2 or borate based phase. Similar LCMO: SiO_2

composites made by sol-gel technique however do not show a decrease in T_c but a slightly reduced magnetization [41] indicating that the nature of magnetic disorder in the present liquid quenched composites is very different. The presence of a kink in the magnetization (Fig. 5.12) at T < 50 K has been observed in composites of LCMO with $SrTiO_3$ and substituted LCMO [23]. This behavior has been attributed to the presence of disordered grain boundaries and covering of the LCMO grains by a non-magnetic insulating phase. Such disorder leads to canting of the Mn-spins at the surface, which also causes a reduction in M and T_c, and broadening of the transition [114], observed in the present work also. The presence of non-magnetic insulating phase should also result in a variation of the electrical transport behavior since the samples now consist of manganite / insulator mixture. Petrov et al. [23] found that the room temperature resistivity of LCMO/$SrTiO_3$ manganite/insulator mixture increases by about 4 orders of magnitude to ~ 10^2 Ωm when the LCMO fraction decreases to < 0.3. The room temperature resistivity in the present work is found to be in the range 10^1-10^2 Ωm, clearly supporting the magnetization results of manganite phase dilution and also in agreement with the results of Petrov et al [23].

5.5 Summary

An important factor for making composites through glass-ceramic process is the selection of glass compositions. In this work, three compositions (Composition I, II and III in Table 5.1) were chosen for making the LCMO: SiO_2 composites via glass-ceramic process using nucleating agents. All the composites show that LCMO phase formation takes place in the as-quenched state itself, indicating a low nucleation barrier. The role of nucleants on the formation of crystalline LCMO phase in the glassy matrix has also been studied. Sb_2O_3 is found to inhibit the nucleation of crystalline phases other than LCMO while Cr_2O_3 has no effect on the nucleation behavior of the various phases. The microstructural results show that LCMO phase is well distributed in the glassy matrix in all the composites. Due to lack of connectivity between LCMO grains, the composites show high resistivity of the order of 10^5 Ωcm at room temperature. The magnetization and electrical transport studies show that the LCMO phase is highly disordered in all the cases.

Chapter 6

Metal – Ceramic Nanocomposite

This chapter describes the microstructural evolution of Ni nanoparticles and structural, transport and magnetic behavior of Ni: NiO/ZrO_2 nanocomposites prepared by a chemical reduction process.

Microstructural evolution of Ni nanoparticles and structural, transport and magnetic behavior of Ni: NiO/ZrO_2 nanocomposites

6.1 Introduction

Among the various synthesis techniques, chemical reduction method is widely used for producing nanoparticles of metal, their alloys and nanocomposite materials with relatively narrow size distribution. A reduction of the transition metal salts by a reducing agent such as sodium borohydride ($NaBH_4$), yields metal, metal oxides and metal borides depending on the reaction conditions as seen from the literature [54, 55].

In the present work Ni nanoparticles and Ni: NiO/ZrO_2 nanocomposites have been prepared by using a chemical reduction process to study their effect on structure, transport and magnetic behavior.

6.2 Experimental details

6.2.1 Synthesis

Ni nanoparticles and Ni: NiO/ZrO_2 nanostructures were synthesized from an aqueous solution of nickel chloride and zirconium oxychloride by a two-stage reduction process. The first stage involves nucleation of the Ni particles in an aqueous salt solution from nickel chloride and zirconium oxychloride by a reducing agent ($NaBH_4$). In the second stage, these powders were heat treated at two different temperatures under a flow of pure H_2 gas or in an air atmosphere.

6.2.2 Reduction reaction by $NaBH_4$

An aqueous solution of 1 M $NiCl_2.6H_2O$: x M $ZrOCl_2.8H_2O$ (where x = 0, 0.01, 0.05, 0.10, 0.15, 0.20 and 0.50 M, M is molar concentration of Zr-salt) and 2 M $NaBH_4$ were prepared separately in 250 ml beakers. The $NiCl_2$ solution (1 M conc.) had an initial pH of 5.1 while a 1 M $ZrOCl_2$ solution was highly acidic with a pH of 1.3. The 2 M $NaBH_4$ solution on the other hand had a starting pH of 9.7. Mixing the $NiCl_2$ and $ZrOCl_2$ solutions results in an acidic solution with a pH of ~ 1.2 and addition of $NaBH_4$ solution increases the pH to 5-6 depending on the concentration of Zr-salt solution. $NaBH_4$ solution is added drop wise to the beaker containing aqueous solution of $NiCl_2.6H_2O$ and $ZrOCl_2.8H_2O$. After the reaction, a black powder precipitates due to an instantaneous reduction of $NiCl_2$ with $NaBH_4$ in absence of Zr-salt. When reduced in the presence of Zr-salt, $ZrO(OH)_2$ gel formation takes place. The

exothermic reaction occurs in successive steps depending on the initial concentration of precursor solutions, the local temperature during the reaction, and other experimental conditions. The reduction reaction was allowed to progress for different durations of time before the precipitate was extracted by centrifuging. The reaction in a simple form can be expressed as follows.

$$2\ NiCl_2.6\ H_2O + 4\ NaBH_4 \rightarrow\ Ni +\ NiO + 4\ NaCl + 2\ B_2O_3 + 5\ H_2O + 15\ H_2\uparrow \qquad 6.1$$

$$ZrOCl_2.8H_2O + 2\ NaBH_4 \rightarrow\ ZrO\ (OH)_2 + 2\ NaCl + B_2O_3 + 3\ H_2O + 8\ H_2\uparrow \qquad 6.2$$

The precipitate was thoroughly washed with distilled water by repeated centrifuging in order to remove completely the water soluble reaction products. The centrifuged product was dried under lamp. Pellets were made from the as-prepared powder at a constant pressure of 75 kg/cm^2. The density and porosity of pellets was determined using standard ASTM technique [115]. Structural studies of the reduced powder were done by X-ray diffraction, transmission electron microscopy. The resistivity was measured using the standard four - probe technique and the magnetization was studied using vibrating sample magnetometer (VSM, LakeShore).

6.2.3 Heat treatment

The as-prepared Pellets were annealed in H_2 or in an air atmosphere at two different temperatures. The annealing temperature was chosen based on the phase transformation temperature of amorphous to crystalline ZrO_2 prepared by chemical reduction process as described below.

Aqueous solutions of 1 M $ZrOCl_2.8H_2O$ and 2 M $NaBH_4$ were prepared separately in 250 ml beakers. The solution of $NaBH_4$ is added drop wise to the beaker containing aqueous solution of $ZrOCl_2.8H_2O$. After the reaction, the precursor solution was centrifuged in distilled water and finally dried under lamp. The as-prepared $ZrO\ (OH)_2$ has an amorphous structure and crystalline ZrO_2 forms on annealing in air atmosphere at different temperatures.

Fig. 6.1 shows the X-ray diffraction pattern of as-prepared $ZrO\ (OH)_2$ powders and from the powder obtained after subsequent heat-treatments at different temperatures for 1 hour in an air atmosphere. It has been observed that ZrO_2 powders have an amorphous structure up to 723 K of annealing in air atmosphere. Tetragonal structure of ZrO_2 forms when the as-prepared $ZrO\ (OH)_2$ powder was annealed at 873 K. The tetragonal ZrO_2 is stable from 873 K to 923 K as seen from the X-ray diffraction pattern. At higher temperature of 973 K, the formation of monoclinic phase of ZrO_2 is seen along with tetragonal phase. The

transformation of tetragonal form to monoclinic form of ZrO_2 is observed at 1073 K. The phases and grain size obtained from the XRD pattern of heat-treated ZrO_2 powders are given in Table 6.1.

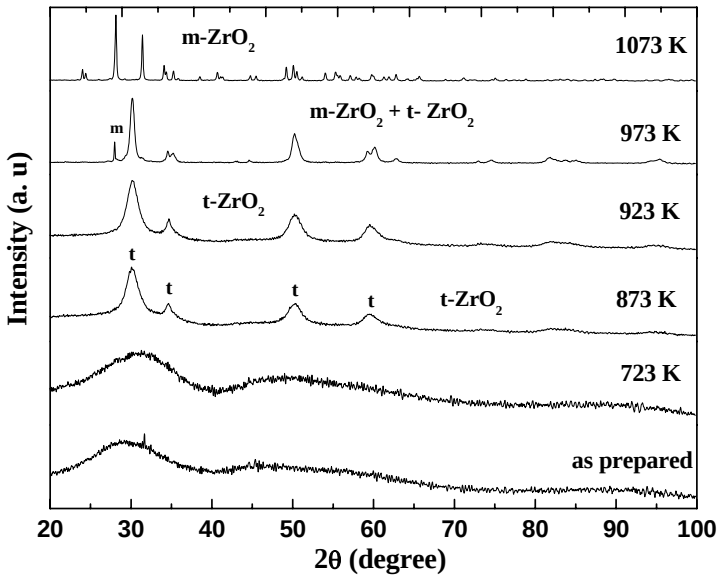

Fig. 6.1: X-ray diffraction pattern of as-prepared ZrO_2 powder heat-treated at different temperatures.

Table 6.1: Phases formed and the grain size obtained from the XRD pattern of the as-prepared as well as heat-treated ZrO_2 samples.

ZrO_2 powder	Phases formed	Approximate grain size (nm) estimated from XRD
As-prepared	Amorphous	---
723 K	Amorphous	---
873 K	Tetragonal ZrO_2	4 (t-ZrO_2)
923 K	Tetragonal ZrO_2	5 (t-ZrO_2)
973 K	Tetragonal (t) ZrO_2 + monoclinic (m) ZrO_2	14 (t-ZrO_2)
1073 K	monoclinic ZrO_2	40 (m-ZrO_2)

The as-prepared ZrO_2 powder shows an amorphous structure up to 723 K where as it converts to tetragonal form of ZrO_2 at 923 K. Hence, in the present work, two heating temperatures 723 K and 923 K have been chosen for heat treatment of Ni: NiO/ZrO_2 nanocomposite powders in air as well as in H_2 atmosphere.

In H_2 atmosphere, NiO present together with Ni is reduced to Ni metal whereas in an air atmosphere Ni gets further converted to NiO. Hence, in this present work, two atmospheres are chosen to study the structural, transport and magnetic behavior of Ni nanoparticles and Ni: NiO/ZrO_2 nanocomposites. A schematic diagram, Fig. 6.2, shows the procedure for heat-treatment of these nanocomposites.

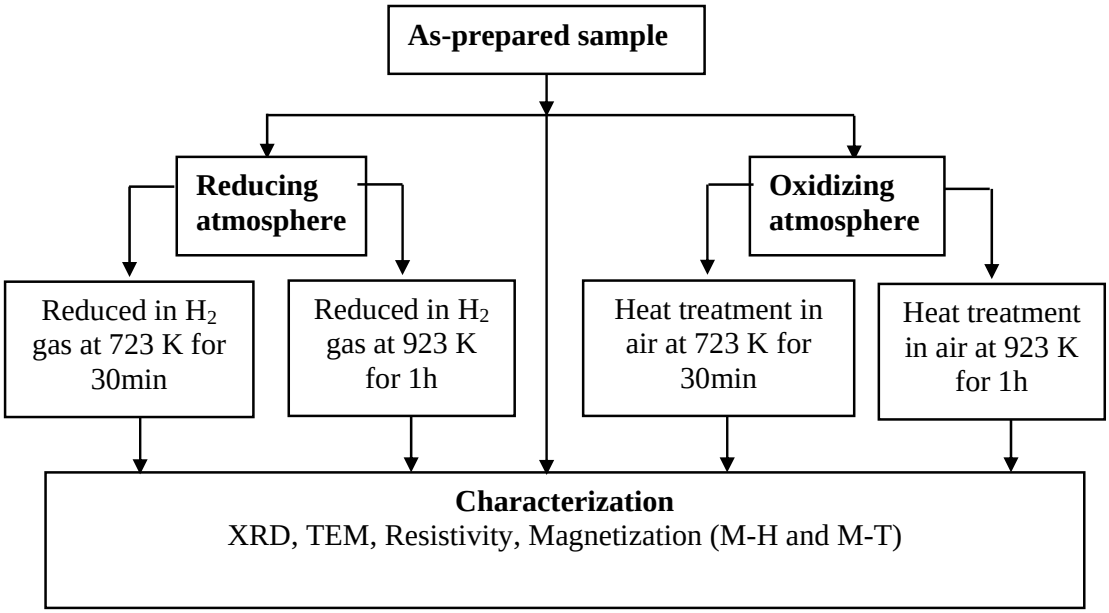

Fig. 6.2: Schematic diagram showing heat treatment procedure of Ni: NiO/ZrO_2 nanocomposites

6.3 Results and discussion

6.3.1 Structure and microstructure

After the addition of $NaBH_4$, the precursor solution of different compositions was kept for two days at room temperature for completion of the reaction. Two days for reaction has been chosen for the following reasons. The formation and evolution of Ni crystals is studied as a function of reaction time with and without the addition of 0.10 M $ZrOCl_2$ solution to $NiCl_2$ solution. The influence of 0.1 M $ZrOCl_2$ addition on the evolution of Ni crystals formation can be seen clearly from the X-ray diffraction patterns shown in Fig. 6.3 (a) and (b). In absence of Zr-salt, Ni crystals formation is incomplete even after 120 hours and the samples show the presence of NiO together with Ni. The Ni peak corresponding to the (111) planes at ~ 45° 2θ is weak and broad. Addition of 0.1 M $ZrOCl_2$ solution to the initial reaction

mixture changes the Ni phase formation kinetics significantly. Clear peaks corresponding to the two planes (111) and (200) can be seen immediately after the addition and the peaks grow with time in intensity as well as sharpness. The addition of Zr-salt however does not prevent completely the formation of an oxide, NiO coating on the Ni crystal clusters. Weak, broad peaks corresponding to the NiO phase can still be seen in the diffraction pattern. The size of the crystalline Ni clusters has been determined from the width of the peaks and is shown in Fig. 6.4. The size of the clusters in the absence of Zr-salt is ~ 2 nm and it increases by about seven fold to 14 nm with the addition of 0.1 M $ZrOCl_2$ solution.

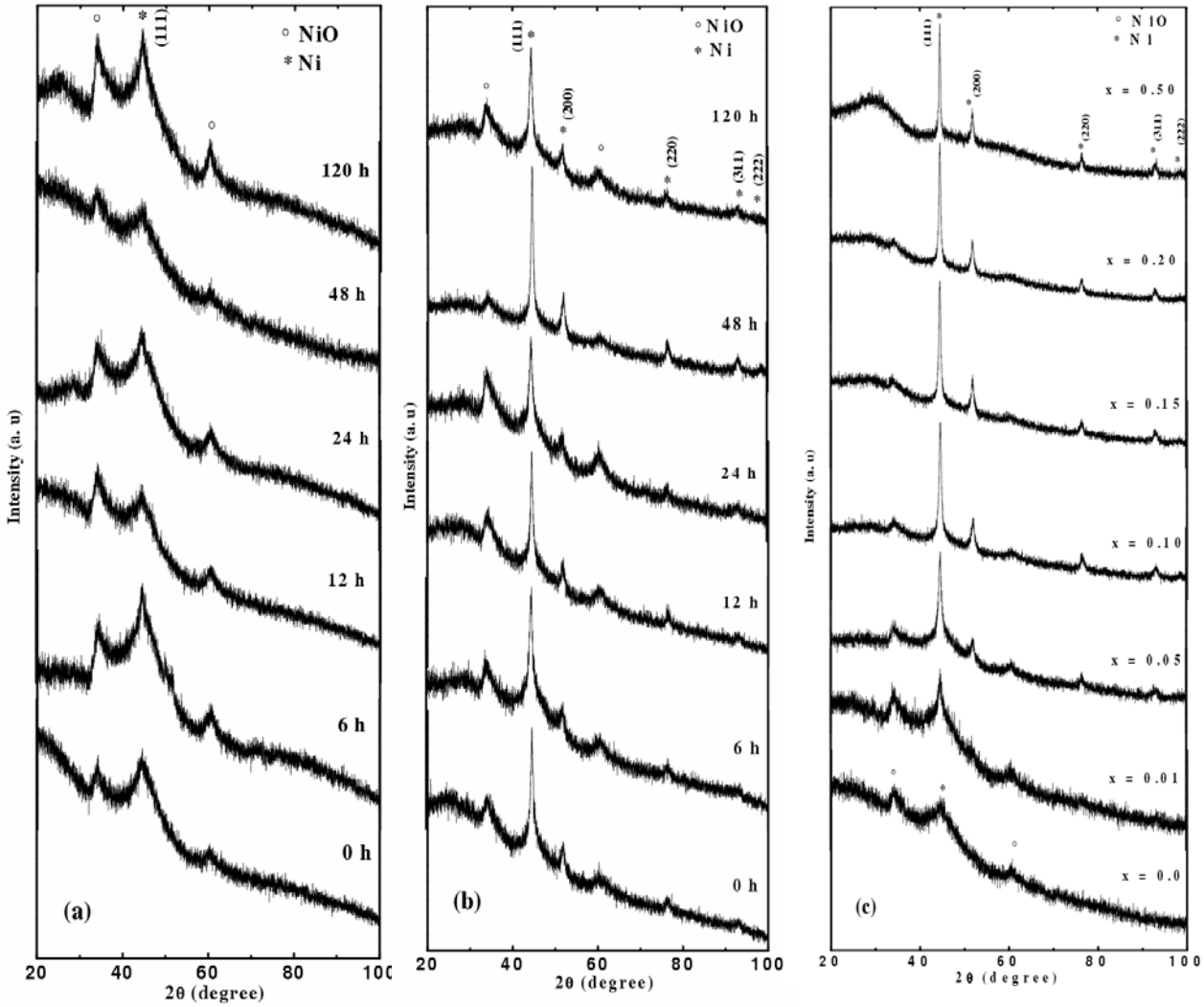

Fig. 6.3: X-ray diffraction pattern from composite Ni powder shows that crystallinity and size are affected by the addition of $ZrOCl_2$ during liquid state reaction. (a) without addition of $ZrOCl_2$, (b) with addition of 0.1 M $ZrOCl_2$ and (c) addition of different concentrations of $ZrOCl_2$.

The crystalline cluster size is found to have a very weak time dependence in both the cases and significant growth was not observed even after prolonged durations. However after 48 hrs the X-ray diffraction peaks show a slight decrease in intensity of the (111) peak indicating the formation of thick NiO coating on the Ni clusters. Hence, in order to study the effect of increasing $ZrOCl_2$ concentration on microstructural evolution in Ni, the reaction was allowed to take place for 48 hrs before extracting the Ni composite powder from the reaction mixture. The results of X-ray diffraction are shown in Fig. 6.3 (c). The weak crystalline peaks become strong with increasing concentration of $ZrOCl_2$ and the NiO peaks decrease progressively. The volume fraction of Ni metal increases progressively and Ni (111) peak become stronger for composition $x > 0.05$. At a concentration of 0.10 M $ZrOCl_2$, the NiO peaks are replaced by a broad hump at $\approx 30\ ^\circ\ 2\theta$ corresponding to the amorphous ZrO_2 phase. The size of the crystalline Ni clusters increases steadily from 2.0 nm to 26 nm for the addition of 0.5 M $ZrOCl_2$ solution, Fig. 6.4. These results clearly indicate the effect of $ZrOCl_2$ addition to the reaction mixture in controlling the size of Ni crystalline clusters. The role played by $ZrOCl_2$ in Ni crystals formation is two fold: (1) Zr-gel formation promotes aggregation of small Ni crystals into a large grain by reducing the effective internal energy and (2) formation of transient low oxidation states of Zr, which aid the reduction of Ni-salt. The lower oxidation states of Zr are known to be less stable compared to the Zr^{4+} state [54] and these intermediate stage lower oxidation states can increase the efficiency of Ni-salt reduction.

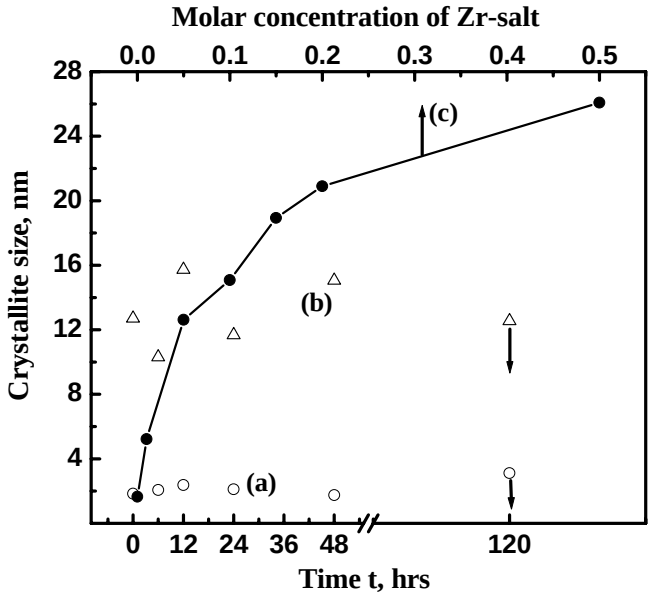

Fig.6.4: Variation of the crystalline Ni cluster size as a function of time t in the absence of $ZrOCl_2$ (a), with addition of 0.1 M $ZrOCl_2$ (b) and (c) as a function of $ZrOCl_2$ concentration. The line through the data points is only a guide.

The X-ray diffraction pattern of as-prepared composites annealed at 723 K in pure H_2 atmosphere is shown in Fig. 6.5. In the presence of H_2 atmosphere, NiO is reduced to Ni metal and the volume fraction of Ni increases compared to as-prepared composites. From the XRD pattern, a broad amorphous NiO peak and crystalline Ni (111) peak is observed in case of sample, x = 0 no addition of Zr-salt to reaction mixture. All the structures clearly show the presence of Ni crystalline peaks, which grow in intensity with increasing Zr-salt content. Similar behavior is observed for the as-prepared samples (see Fig. 6.3 c), where the broad amorphous NiO peak progressively disappears and Ni crystalline peaks become stronger. In case of annealed composites for x = 0.10, only Ni peaks could be observed and for $x \geq 0.20$, a broad amorphous peak corresponding to ZrO_2 is seen. It clearly shows that this is the range of composition over which a transition from NiO shell to ZrO shell takes place. The grain size increases with the addition of Zr content in these nanocomposites and is given in Table 6.3.

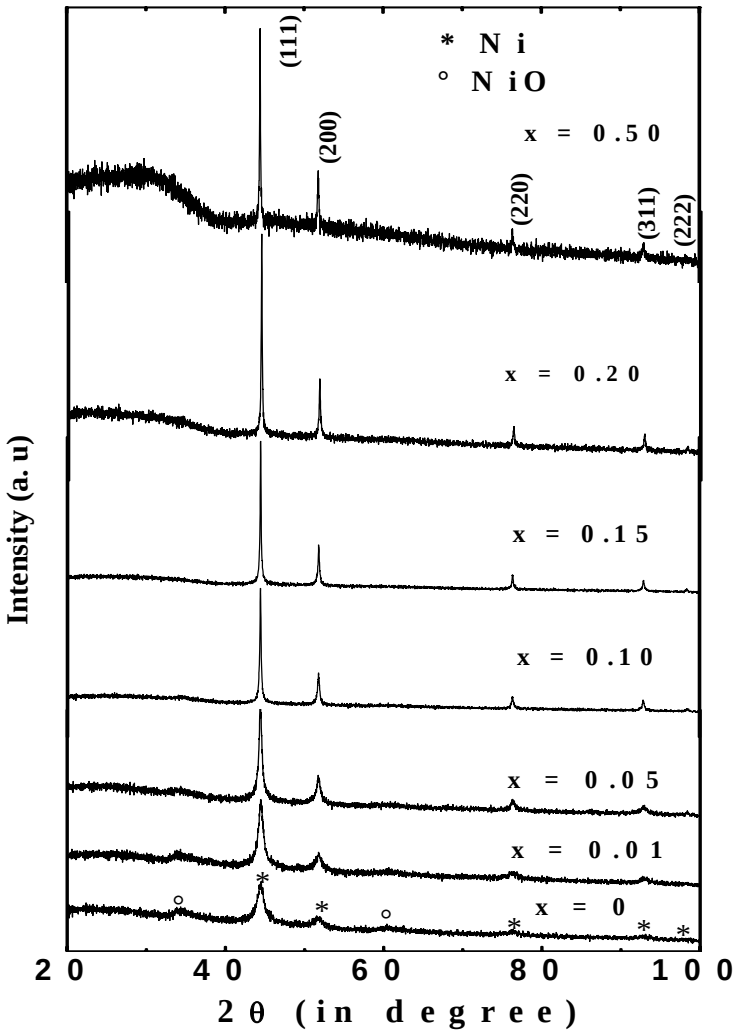

Fig. 6.5: X-ray diffraction pattern of Ni: x M ZrO_2 composite annealed at 723 K in H_2 atmosphere. Ni (111) peak increases with increasing Zr-salt content and also becomes sharp.

In the above two cases, (as-prepared and annealed at 723 K in H_2 atmosphere) nano grain Ni particles were embedded in an amorphous NiO/ZrO_2 matrix. The as-prepared composites were annealed at 923 K, temperature at which a-ZrO_2 transforms to t-ZrO_2 in H_2 atmosphere. Here, nanograin Ni particles are embedded in a tetragonal ZrO_2 matrix, which could be seen from XRD pattern. Fig. 6.6 shows the X-ray diffraction patterns of composites annealed at 923 K in H_2 atmosphere.

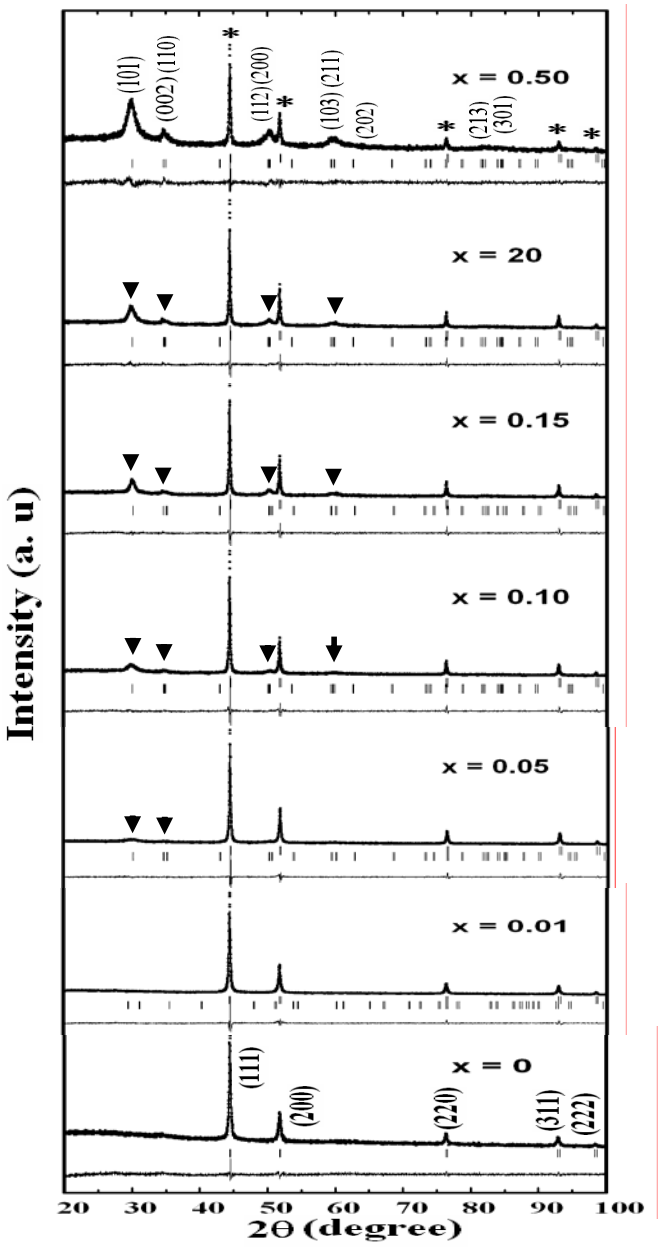

Fig. 6.6: X-ray diffraction pattern of Ni: x M ZrO_2 nanostructure reduced at 923 K in H_2 atmosphere. Arrow mark indicates the position of t-ZrO_2 in these composites. The Rietveld fit assuming Fm-3m of Ni FCC structure and P42/nmc of tetragonal ZrO_2 is shown by continuous line and the position of Bragg lines for the Ni and tetragonal ZrO_2 phase are shown by vertical lines below the data.

In this case, both the volume fraction of Ni increases as well as transformation of amorphous ZrO_2 to crystalline t- ZrO_2 takes place. From the XRD pattern, all the structures clearly show the presence of either crystalline Ni peaks or t-ZrO_2 peaks which appear for composition $x \geq 0.05$ in this nanostructure. Structural analysis was done by Rietveld refinement and is shown in Fig. 6.6. A Rietveld refinement of all the diffraction patterns was performed considering a space group $Fm\bar{3}m$ for Ni and space group P42/nmc for t-ZrO_2 to determine the lattice parameter of individual phases accurately. The Rietveld fit is shown by continuous line and the position of Bragg lines for the Ni and t-ZrO_2 phase are shown by vertical lines below the data in the Fig. 6.6.

To understand the stability of Ni particles in presence of oxygen, the as-prepared composites were annealed at 723 K and 923 K in air atmosphere. Fig. 6.7 (a) and (b) show the X-ray diffraction pattern of the composites annealed at 723 K and 923 K respectively in air atmosphere.

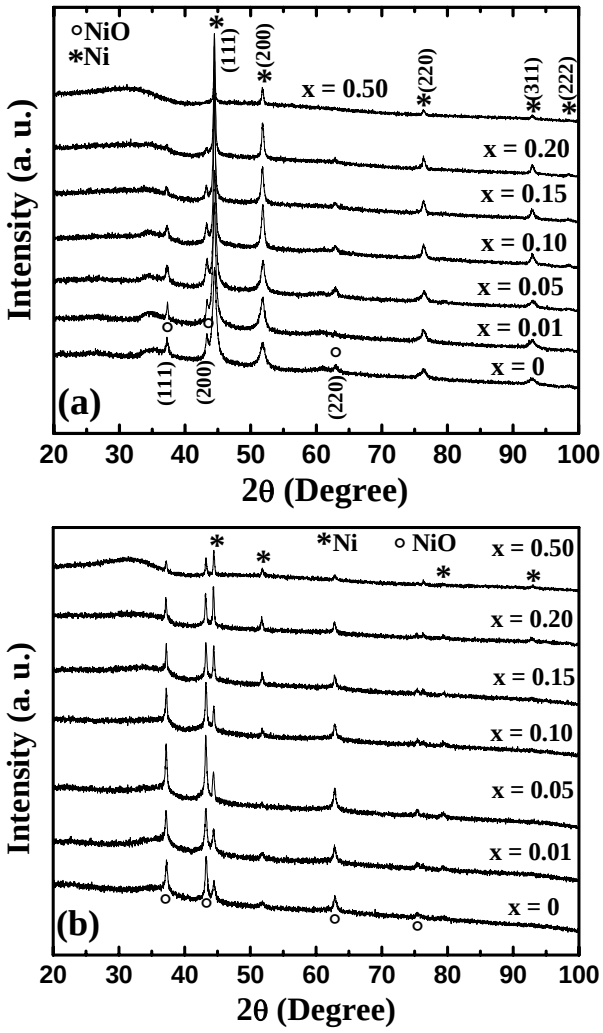

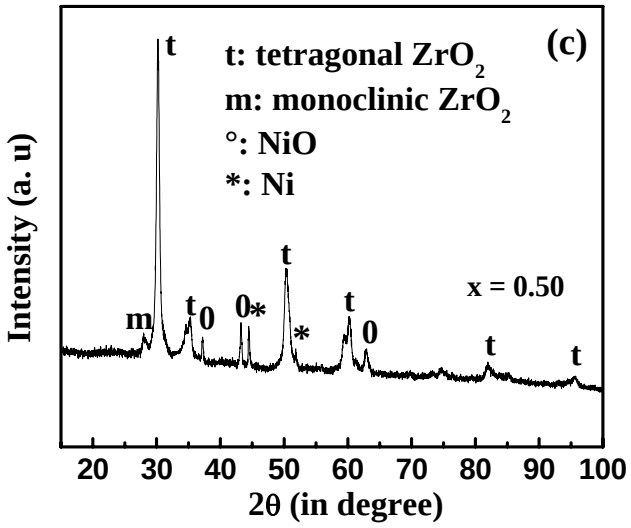

Fig. 6.7: X-ray diffraction pattern of Ni: x Zr-O nanostructure annealed at different temperatures in air atmosphere: (a) at 723 K (b) at 923 K (c) for sample x = 0.50 at 1023 K. In these nanostructures, the formation of t-ZrO_2 is observed at about 1023 K in air atmosphere.

In the absence of Zr-salt (x = 0), the composite shows major amount of Ni phase with minor NiO phase at 723 K. The minor NiO phase decreases progressively with the addition of ZrO_2 as seen from Fig. 6.7 (a). The presence of only crystalline Ni phase with negligible NiO phase is observed for composites with $x \geq 0.20$. The NiO phase increases for x = 0 when the composite is heat-treated at 923 K in air atmosphere. At 923 K, all the composites show both crystalline phases of Ni and NiO with no ZrO_2 phase (as seen from Fig. 6.7 b). As seen from Fig. 6.1, the as-prepared amorphous ZrO_2 transform to tetragonal ZrO_2 at 923 K in air atmosphere. In the presence of crystalline Ni or NiO phase in the composite, the ZrO_2 phase remains amorphous (in Fig. 6.7 b) up to 923 K. The composites show crystalline Ni and NiO phase with tetragonal phase of ZrO_2 after heat-treating at 1023 K in air atmosphere. Fig. 6.7 (c) shows X-ray diffraction pattern of composite (composition, x = 0.50) heat-treated at 1023 K in air atmosphere. The average grain size of Ni particles for all composites can be determined from the half width of the peaks using the Debye Scherrer relation and is given in Table 6.3.

The microstructural characterization of all the composites has been done using transmission electron microscopy (TEM). It gives an idea about how nanosize Ni particles are distributed in an amorphous or crystalline NiO/ZrO_2 matrix. Fig. 6.8 (a) and (b) show the TEM micrographs of as-prepared composites x = 0 and x = 0.10 respectively and (c) and (d) are the diffraction patterns of their respective samples. The micrograph (Fig. 6.8 a), indicates

that amorphous NiO encloses the Ni cluster for composite x = 0. The diffuse ring in Fig. 6.8 (c) agrees with the presence of amorphous nature of Ni or NiO in the composite x = 0. As the Zr-salt content increases (for the composite x = 0.10), the diffuse ring converts to a mixture of sharp ring of Ni (FCC) with diffuse ring of NiO / ZrO_2 in the composite as shown in Fig. 6.8 (d). Due to the decrease of amorphous NiO and simultaneous increase of volume fraction of Ni phase gives an agglomerated nature of the Ni particles in the composite x = 0.10 (shown in Fig. 6.8 b). The size of Ni particles of the as-prepared composites is < 100 nm from the TEM micrographs. All these microstructural results agree with the X-ray diffraction pattern of as-prepared composite as shown in Fig. 6.4 (c).

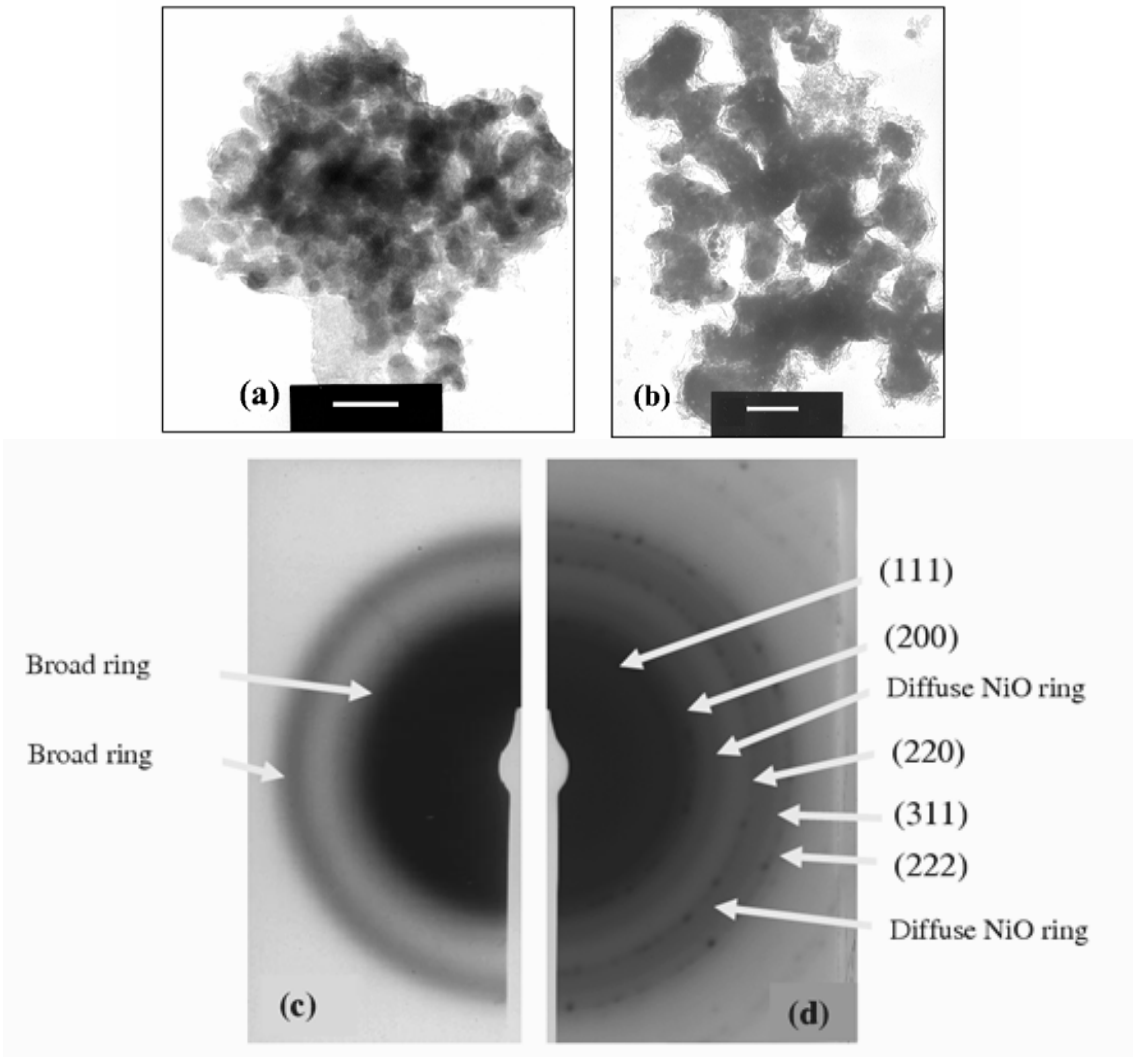

Fig. 6.8: TEM micrographs of the as-prepared composites showing presence of amorphous NiO encapsulate on amorphous Ni nanoparticles for composite x = 0 (a), whereas for x = 0.10 (b), it decreases and Ni crystallinity increases. Diffraction pattern indicates the diffuse NiO ring (c), which is replaced by sharp rings of Ni (FCC structure) for 0.10 Zr-O (d). Scale corresponds to 200 nm

Fig. 6.9 shows the high magnification TEM micrograph of as-prepared composite without the addition of Zr-salt. It shows clearly the Ni clusters enclosed in either NiO or ZrO_2 matrix. Pure Zr-salt solution when reduced with $NaBH_4$ gives an amorphous oxide which on annealing at 873 K for 1 hour is found to give tetragonal ZrO_2. Hence it can be concluded that in the as-prepared state the Ni crystals are distributed in an amorphous ZrO_2 matrix phase.

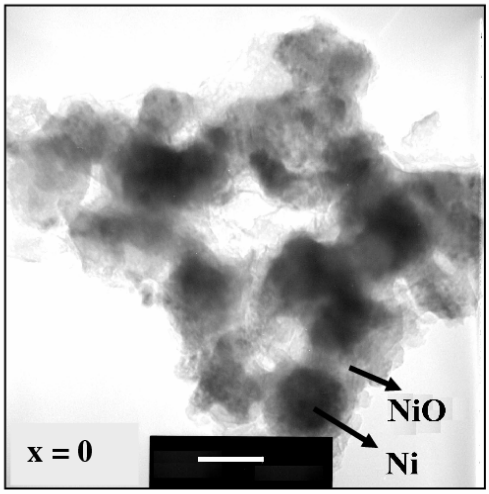

Fig. 6.9: Higher magnification TEM micrograph of the as-prepared composite (composition x =0) shows that NiO covers the Ni particle. Scale corresponds to 50 nm.

Fig. 6.10 shows the TEM micrographs and the diffraction patterns of composites (x = 0 and x = 0.10) annealed at 723 K in H_2 atmosphere. The micrograph (Fig. 6.10 a) and the diffraction pattern (Fig. 6.10 c) indicates that Ni nanograins are embedded in a NiO matrix for composite x = 0 (absence of Zr-salt). The NiO phase decreases and a thin layer of NiO/ZrO_2 covers the Ni particles in the composite x = 0.10 (Fig. 6.10 b). The diffuse ring from amorphous NiO (Fig. 6.10 c) is absent for composite x = 0.10 (Fig. 6.10 d), supporting the X-ray diffraction results.

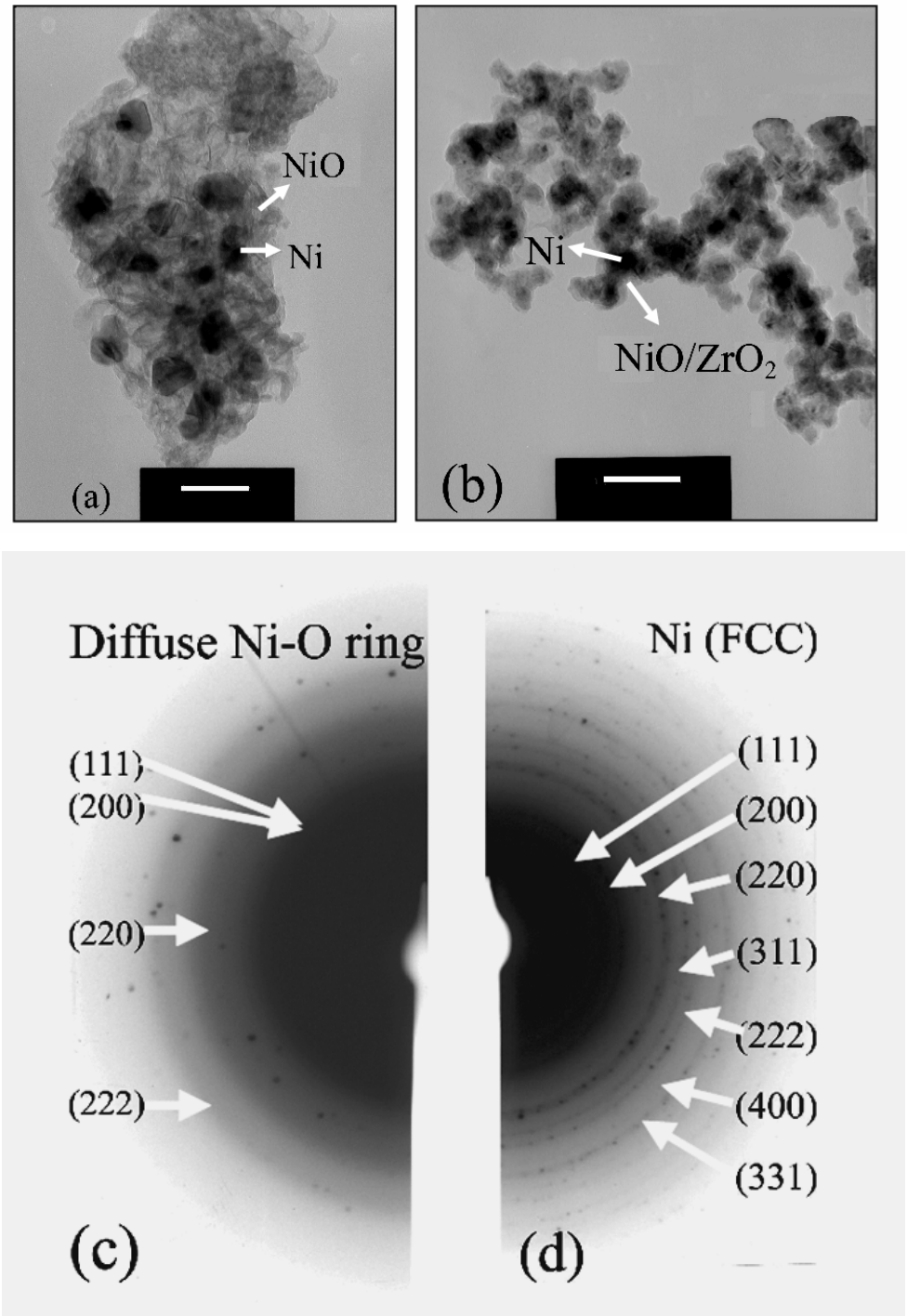

Fig. 6.10: TEM micrographs of composite annealed at 723 K in H_2 atmosphere showing the presence of amorphous NiO encapsulate on Ni nanoparticles for sample x = 0 (a), where as for x = 0.10 (b), it decreases. Diffraction pattern indicates the diffuse NiO ring (c), which is replaced by sharp rings of Ni (FCC structure) (d) for 0.1 Zr-O. Scale corresponds to 100 nm.

Ni particles in the composite (x = 0.10) heat-treated at 923 K in H_2 atmosphere is in the range of 20 nm to 60 nm, which can be seen from the bright field TEM micrographs (Fig. 6.11 a). Fig. 6.11 (b) and (c) show dark field TEM micrographs (negative film) of composite (x = 0.10) heat-treated at 923 K in H_2 atmosphere and 723 K in air atmosphere respectively. The grain size of the Ni particle in these composites estimated from the dark field image is 20 to 60 nm, which agrees with the grain size calculated from the X-ray diffraction pattern.

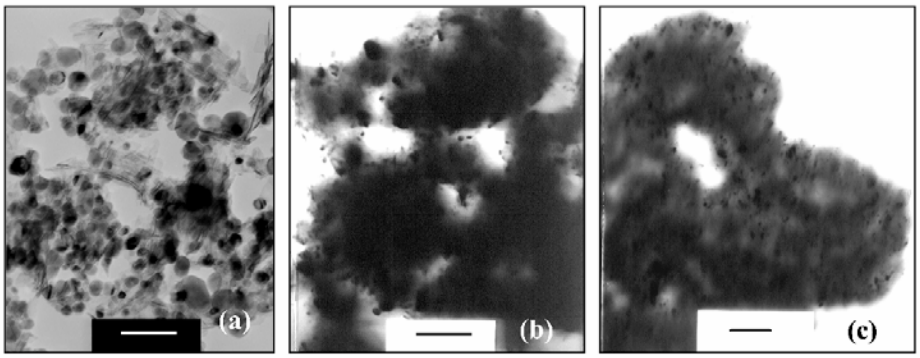

Fig. 6.11: TEM micrographs (a) bright field and (b) dark field image of composites annealed at 923 K in H_2 atmosphere and (c) dark field image of composites annealed at 723 K in air atmosphere. The grain size of Ni is in the range of 20 to 60 nm as seen from both bright and dark field image of the composite (x = 0.10). Scale corresponds to 200 nm in all cases.

6.3.2 Particle size measurement

The results on distribution of hydrodynamic diameters of the as-prepared Ni: NiO/ZrO_2 nanocomposites, obtained from the photon correlation spectroscopy (PCS) instrument (Zeta Plus) are shown in Fig. 6.12. The polydispersity index is a measure of the width and size distribution of the particles. In general, polydispersity index from 0.000 to 0.020 is an indication of monodisperse, 0.020 to 0.080 for narrow distribution and larger for broader distribution. The polydispersity index of as-prepared composite x = 0 lies in between 0.005 to 0.079. It implies narrow distribution of Ni particles in the Ni: NiO/ZrO_2 composite (see Fig. 6.12 a) and the average hydrodynamic size of Ni particles is in the range 185 to 210 nm, in agreement with TEM micrographs. It is observed that the polydispersity index of as-prepared composite x = 0.10 lies in between 0.005 to 0.214, a broader distribution of Ni particles and the average hydrodynamic size of Ni particles is in the range from 210 to 270 nm, in agreement with TEM micrographs.

The particle size increases when the as-prepared Ni: NiO/ZrO_2 nanocomposites are annealed in air or in H_2 atmosphere. The range of particle size, mean diameter of Ni particle

and the polydispersity index of the as-prepared and annealed composites (typical example of composition; x = 0 and x = 0.10) either at 723 K or at 923 K in air or H_2 atmosphere is given in Table 6.2. It can be seen that the average size increases due to annealing.

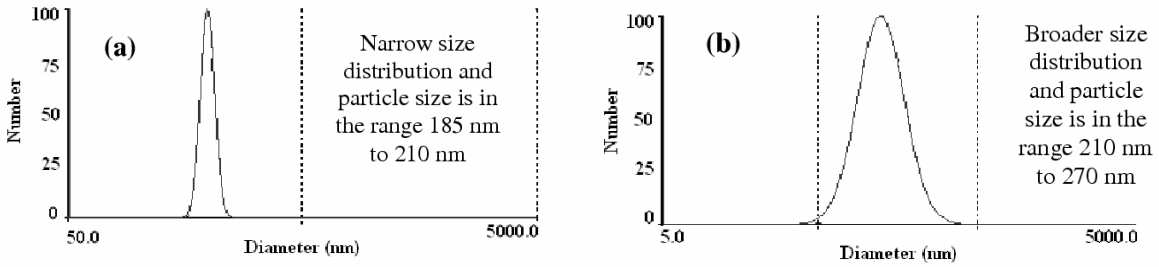

Fig. 6.12: Distribution plot of hydrodynamic diameters of Ni particles in the as-prepared Ni: NiO/ZrO_2 composites obtained from PCS measurement: (a) for sample x = 0 and (b) for x = 0.10.

Table 6.2: Particle size range, mean diameter and the polydispersity index obtained from PCS measurement for the as-prepared as well as annealed composites.

Composite	Composition	Particle size range (in nm)	Mean diameter (in nm)	Polydispersity index
As-prepared	x = 0	185 – 210	204	0.005 – 0.079
	x = 0.10	210 – 270	230	0.005 – 0.214
723 K in H_2	x = 0	321 – 410	265	0.005 – 0.224
	x = 0.10	191 – 534	356	0.005 – 0.286
923 K in H_2	x = 0	365 – 750	527	0.005 – 0.215
	x = 0.10	294 – 456	350	0.005 – 0.185
723 K in Air	x = 0	216 – 340	272	0.005 – 0.155
	x = 0.10	212 – 381	286	0.005 – 0.198
923 K in Air	x = 0	273 – 539	415	0.005 – 0.218
	x = 0.10	200 – 489	366	0.005 – 0.166

Table 6.3 summarizes the phases present in the as-prepared, annealed in H_2 atmosphere as well as air atmosphere and also grain size obtained from the XRD as well as TEM of all the composites.

Table 6.3: Phases and grain size of Ni obtained from XRD as well as TEM for all composites

Sample Ni: x M ZrO_2	Phases present from XRD	Grain Size estimated (nm) from XRD	Particle Size (nm) from TEM
As-prepared			
x = 0	Ni (A) + NiO (A)	2	20 - 50
x = 0.01	Ni (C) + NiO (A)	10	
x = 0.05	Ni (C) + NiO (A)	13	
x = 0.10	Ni (C) + NiO (A)	16	50 - 70
x = 0.15	Ni (C) + NiO (A) + ZrO_2 (A)	19	
x = 0.20	Ni (C) + ZrO_2 (A)	22	
x = 0.50	Ni (C) + ZrO_2 (A)	26	
723 K under H_2			
x = 0	Ni (C) + NiO (A)	9	30 - 60
x = 0.01	Ni (C) + NiO (A)	12	
x = 0.05	Ni (C) + NiO (A)	21	
x = 0.10	Ni (C)	46	30 - 60
x = 0.15	Ni (C)	61	
x = 0.20	Ni (C) + ZrO_2 (A)	69	
x = 0.50	Ni (C) + ZrO_2 (A)	72	
923 K under H_2			
x = 0	Ni (C)	35	50 - 100
x = 0.01	Ni (C)	49	
x = 0.05	Ni (C) + t - ZrO_2	53	
x = 0.10	Ni (C) + t - ZrO_2	66	20 - 80
x = 0.15	Ni (C) + t - ZrO_2	65	
x = 0.20	Ni (C) + t - ZrO_2	64	
x = 0.50	Ni (C) + t - ZrO_2	62	
723 K under Air			
x = 0	Ni (C) + NiO (C)	15	
x = 0.01	Ni (C) + NiO (C)	17	
x = 0.05	Ni (C) + NiO (C)	19	
x = 0.10	Ni (C) + NiO (C)	25	60 - 80
x = 0.15	Ni (C) + NiO (C) + ZrO_2 (A)	28	
x = 0.20	Ni (C) + NiO (C) + ZrO_2(A)	30	
x = 0.50	Ni (C) + ZrO (A)	39	
923 K under Air			
x = 0	NiO (C) + Ni (C)	26	50 - 80
x = 0.01	NiO (C) + Ni (C)	28	
x = 0.05	NiO (C) + Ni (C)	29	
x = 0.10	NiO (C) + Ni (C)	33	70 - 90
x = 0.15	NiO (C) + Ni (C) + ZrO_2 (A)	32	
x = 0.20	NiO (C) + Ni (C) + ZrO_2 (A)	40	
x = 0.50	NiO (C) + Ni (C) + ZrO_2 (A)	38	
1023 K under Air			
x = 0.50	t – ZrO_2 + m – ZrO_2 + Ni (C)+ NiO (C)	37	

Note: (C), (A), t and m represents crystalline nature, amorphous nature, tetragonal phase and monoclinic phase respectively.

6.3.3 Electrical transport

The electrical resistivity of as-prepared composites is of the order of 10^5 Ω cm at room temperature. The nanograin Ni particles in the as-prepared composites are distributed in NiO/ZrO_2 matrix. The higher resistivity is due to the presence of amorphous NiO/ZrO_2 layer between the two Ni particles. The composites annealed at 723 K or 923 K in air atmosphere have high resistivity, of the order of 10^6 Ω cm at room temperature and hence their temperature dependence could not be studied. However, annealing in H_2 atmosphere, reduces NiO to Ni metal at 723 K or at 923 K and thus leads to better interparticle connectivity. Hence, the electrical transport of these composites is described in detail.

Fig. 6.13 (a) shows the electrical resistivity as a function of temperature of the composites (Ni: x ZrO) annealed at 723 K in H_2 atmosphere. In the absence of Zr-salt (composition, x = 0), the composite shows major crystalline Ni phase with minor NiO insulating amorphous phase (from the XRD pattern, Fig. 6.5).

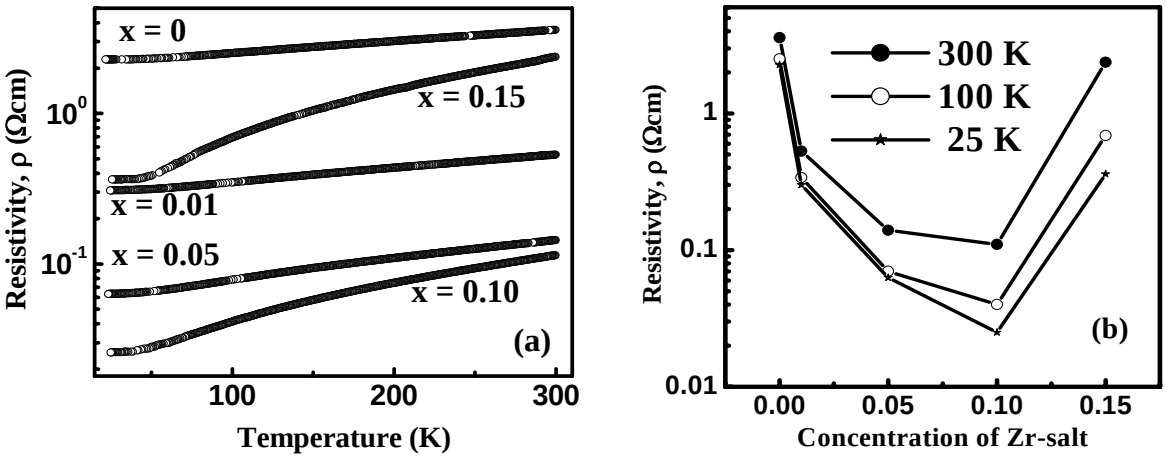

Fig. 6.13: Electrical resistivity as a function of temperature of the as-prepared composite annealed at 723 K in H_2 atmosphere is shown in (a) and the resistivity as a function of concentration of Zr-salt at three different temperatures is shown in (b).

At room temperature the electrical resistivity of the composite (x = 0) is 3.57 Ω cm, which is very large compared to bulk Ni value (6.8×10^{-6} Ω cm). Due to the presence of insulating NiO, the composite gives a higher electrical resistivity. As the Zr-salt content increases in these composites, NiO phase decreases and simultaneously the volume of Ni content increases (seen from Fig. 6.5 and Fig. 6.10) which results in higher electrical conductivity. Fig. 6.13 (b) shows the electrical resistivity as a function of concentration of Zr-

salt in the precursor solution. It can be seen that the absolute resistivity decreases first (up to x ≤ 0.10) and then increases with the addition of Zr-salt (x ≥ 0.15). The electrical resistivity of composites with x > 0.15 was very high in the insulating regime and could not be measured. These results are in agreement with the microstructural results, which show that initially the addition of Zr-salt promotes Ni formation leading to a better inter-particle connectivity while it is reduced for x ≥ 0.1 due to ZrO_2 encapsulation, which is an insulator. The resistivity of all the composites gives strong temperature dependence, which is typical of metals [116].

Fig. 6.14 (a) and (b) show the electrical resistivity as a function of temperature and concentration of Zr-salt content respectively of the as-prepared composites annealed at 923 K in H_2 atmosphere. Here, the absolute resistivity decreases first (up to x ≤ 0.01) and then increases with the addition of Zr-salt to the precursor solution (x ≥ 0.05). The resistivity of all the composites shows strong temperature dependence, which is typical of metals. The electrical resistivity of composites with x > 0.10 was very high, insulating regime and could not be measured. After annealing at 923 K in H_2 atmosphere, the volume fraction of Ni for composite x = 0 is more when compared to the composite heat-treated at 723 K. Hence, the absolute resistivity of the composite x = 0 decreases as the annealing temperature increases from 723 K to 923 K in H_2 atmosphere. The microstructural results indicate that the presence of insulating t-ZrO_2, leads to a lack of electrical conductivity between the Ni grains. Therefore, the electrical resistivity initially drops up to x ≤ 0.01 (due to better interparticle connectivity between the Ni grains) and then increases. The resistivity data of the composites heat-treated at 723 K and 923 K in H_2 atmosphere are given in Table 6.4.

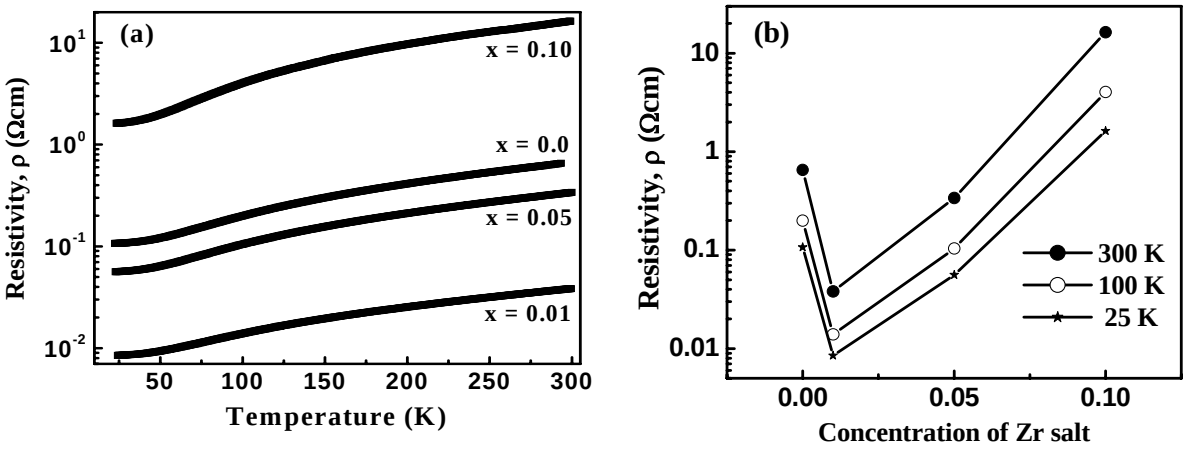

Fig.6.14: Electrical resistivity as a function of temperature of the as-prepared composite annealed at 923 K in H_2 atmosphere is shown in (a) and the resistivity as a function of concentration of Zr-salt at three different temperatures is shown in (b).

Table 6.4: Resistivity data of the composites annealed at 723 K and 923 K in H_2 atmosphere.

Sample	Resistivity at 300 K (Ω cm)	Resistivity at 100 K (Ω cm)	Resistivity at 25 K (Ω cm)
723 K in H_2			
x = 0	3.59	2.51	2.27
x = 0.01	0.53	0.34	0.30
x = 0.05	0.14	0.07	0.063
x = 0.10	0.11	0.04	0.025
x = 0.15	2.37	0.69	0.36
923 K in H_2			
x = 0	0.63	0.199	0.107
x = 0.01	0.038	0.014	0.0085
x = 0.05	0.338	0.104	0.056
x = 0.10	16.3	4.025	1.624
x = 0.15	10^{+4}	----	----

6.3.4 Magnetization

The magnetic properties of as-prepared Ni: NiO/ZrO_2 nanocomposites were studied as a function of external magnetic field H up to 2.0 T at room temperature. The M-H loops in all the cases, as a function of time t and Zr-salt concentration, show a typical ferromagnetic behavior, Fig. 6.15.

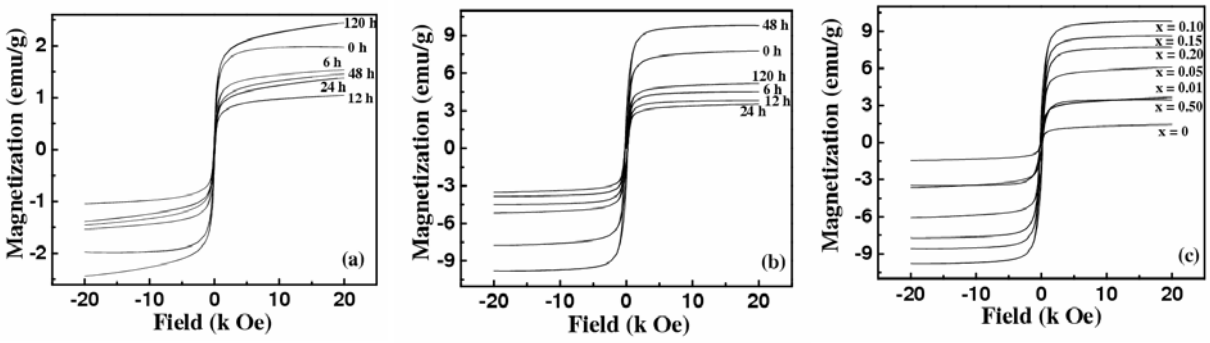

Fig. 6.15: Room temperature magnetic hysteresis loops of crystalline Ni cluster composites, (a) without addition of $ZrOCl_2$, (b) with addition of 0.1 M $ZrOCl_2$ and (c) with changing $ZrOCl_2$ concentration.

The magnetization M however reaches saturation at external fields H > 0.5 T, an order of magnitude higher compared to the saturation fields required for bulk Ni. The value of saturation magnetization in all the cases is much lower than the saturation magnetization of bulk Ni, 54.4 emu g^{-1}. The lower value of saturation magnetization is due to the presence of non-magnetic coating on the ferromagnetic Ni clusters, nano size of the crystallites and lack of a well defined crystal in the case without any Zr-salt addition. Encapsulation by non-magnetic materials and nano size are generally known to reduce the magnetization of ferromagnetic metals [117, 118]. The lowest value of coercivity is found to be ~ 60 Oe for the as-prepared Ni without any Zr-salt addition and ~ 200 Oe for the addition of 0.1 M Zr-salt. The variation of saturation magnetization M_s and coercivity H_c as a function of time t and Zr-salt concentration are shown in Fig. 6.16.The saturation magnetization and the coercivity do not show any systematic variation with reaction time t, similar to the crystallite size variation. The variation with concentration of $ZrOCl_2$ solution however has a systematic dependence. The crystallite size increases steadily while M_s increases to 10 emu g^{-1} for 0.1 M concentration before it starts to decrease. The initial increase is due to the formation of well defined crystallites which are embedded in a ZrO_2 matrix. For concentrations x > 0.1 M the non-magnetic constituents decrease the effective volume of Ni crystals leading to a decrease in M_s.

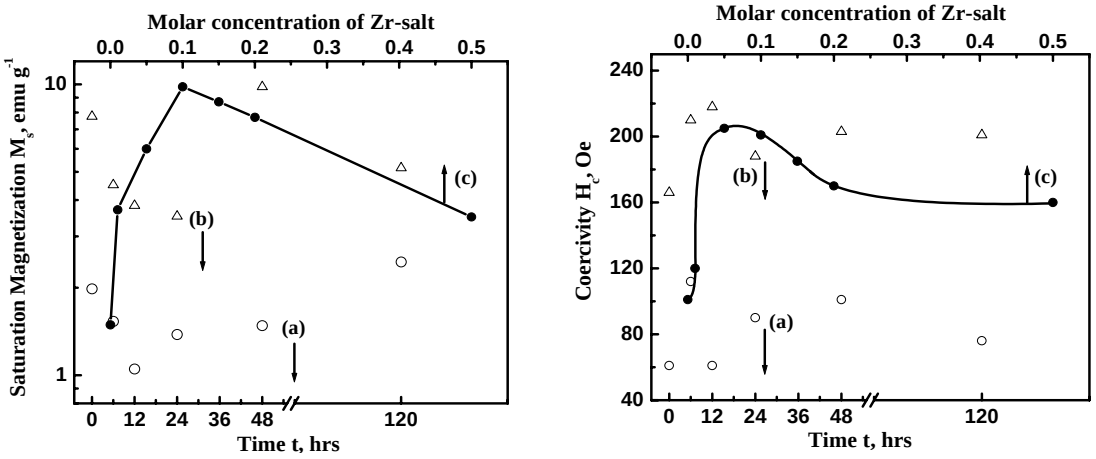

Fig. 6.16: Room temperature saturation magnetization M_s variation (a) and coercivity H_c variation (b) in the different Ni cluster composites. The line through the data points is only a guide.

Magnetization as a function of field (M-H loop) up to 20 kOe both at room temperature and at 85 K for the as-prepared and annealed Ni: NiO/ZrO_2 composites are studied and the results are shown in Fig. 6.17.

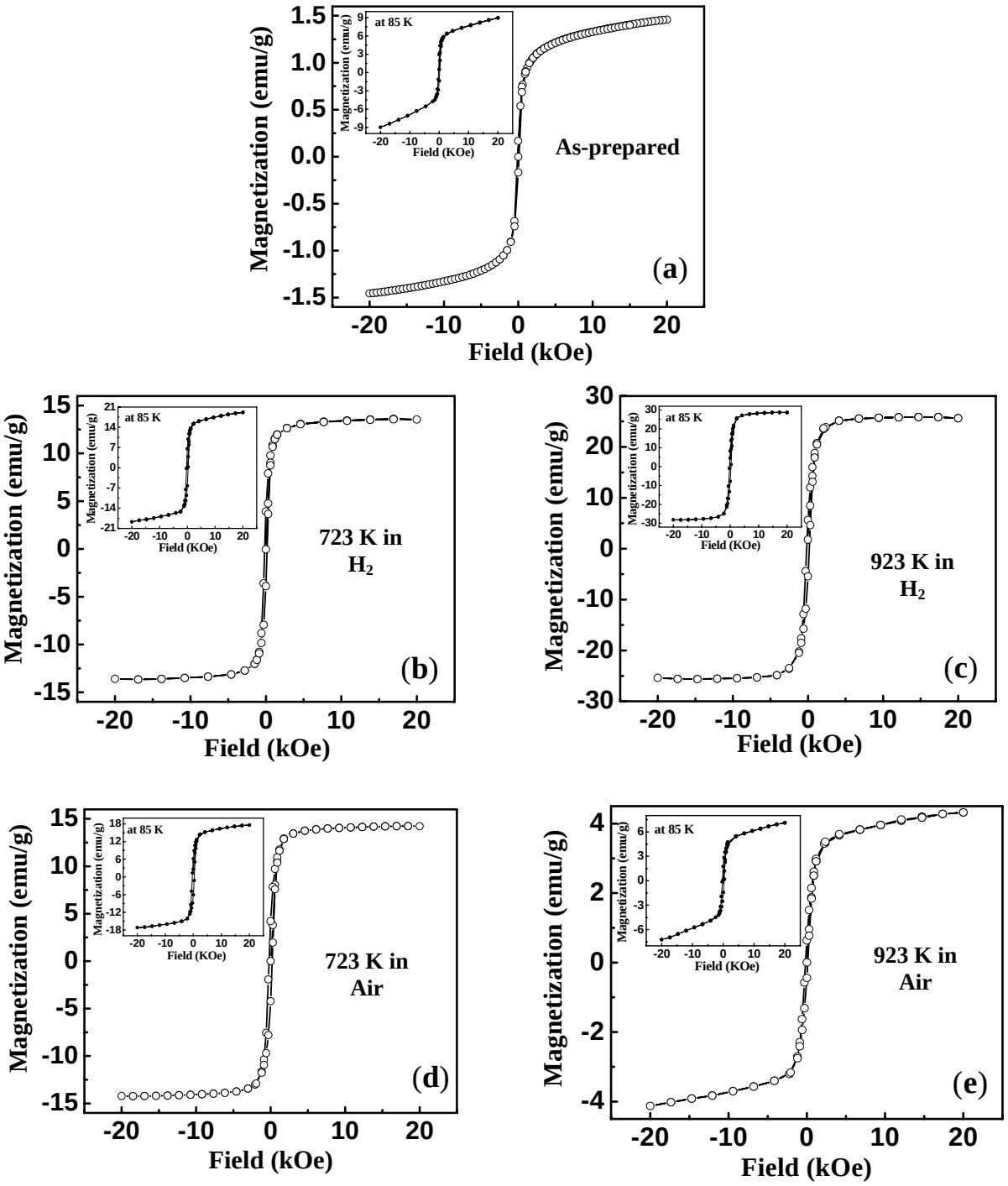

Fig. 6.17 (a) – (e): M-H loops of as-prepared composite of composition x = 0.0 heat-treated at two different temperatures in H_2 as well as in air atmosphere. Inset shows the M-H loop at 85 K of the respective samples.

The M-H loop of the as-prepared composite (x = 0) measured at room temperature indicates typical ferromagnetic nature with non-saturating behavior as shown in Fig. 6.17 (a). From the structural studies, an amorphous nature of Ni and NiO is seen for this sample. Amorphous NiO covers the nanograin Ni particles as seen from the microstructural TEM studies. The non-saturating behavior is mainly due to the presence of amorphous and antiferromagnetic nature of NiO phase present in this system. The non-saturating behavior of all these composites is also observed from the M-H loop at 85 K as seen from the inset of Fig. 6.17. The magnetization value increases progressively when the as-prepared composites are heat-treated at either 723 K or 923 K in H_2 atmosphere. In the presence of H_2 atmosphere, NiO presumably is reduced to Ni and the volume fraction of Ni increases and thus magnetization increases. The M-H loop shows near saturation behavior both at room temperature as well as at 85 K for the composite (x = 0) heat-treated at 923 K in H_2 atmosphere as shown in Fig. 6.17 (c). From Fig. 6.17 (b) and (d) it is observed that the magnetization values at room temperature are nearly same for the composite x = 0 heat-treated at 723 K either in H_2 or in air atmosphere. However, if heated in air atmosphere at 723 K, the composite (x = 0) has Ni as the major phase along with NiO as minor phase that is seen from structural studies (Fig. 6.7 a). It indicates that up to 723 K, Ni phase is stable and at higher temperature (923 K) Ni is oxidized to NiO phase when annealed in air. At higher temperature (at 923 K) in air atmosphere, the magnetization value decreases and shows non-saturating behavior at room temperature as well as at 85 K for the composite x = 0 as shown in Fig. 6.17 (e). This is due to the formation of NiO (which is antiferromagnetic in nature) in the composites.

The magnetization behavior as a concentration of Zr-salt of the as-prepared as well as annealed Ni: NiO/ZrO_2 system is shown in Fig. 6.18. All the composites indicate that the magnetization value first increases slowly and then decreases except for composite heat-treated at 923 K in air atmosphere. The first increase of magnetization value upto a certain concentration indicates the increase of volume fraction of Ni in the system. From the structural studies (Fig. 6.4) of the as-prepared composites, it was observed that nickel nanoparticles presumably nucleate and grow with the addition of Zr-salt in a single reduction process. In this case, Zr-salt stabilizes Ni formation and also protects Ni from being oxidized. Similar behavior of increase of Ni concentration is also observed for annealed composites. The volume fraction of Ni increases along with the reduction of NiO phase up to a certain

concentration resulting in an increase of magnetization in these composites. However, beyond this concentration, the magnetization decreases due to increase of non-magnetic constituents.

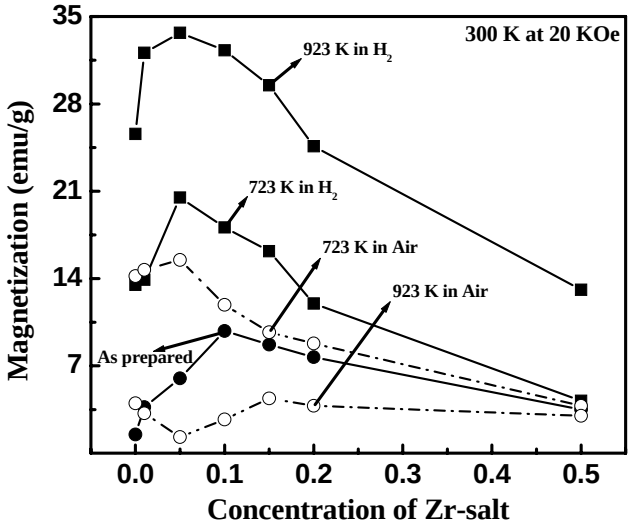

Fig. 6.18: Magnetization behavior as a function of concentration of Zr-salt for the as-prepared composite (Ni: NiO/ZrO) heat-treated at two different temperatures in H_2 as well as in air atmosphere.

The composite heat-treated at 923 K in air atmosphere indicates that the magnetization first decreases up to x = 0.05 (Fig. 6.18) due to increase of antiferromagnetic NiO as seen from the XRD pattern (in Fig. 6.7 b). The most intense peak of Ni increases slowly with the addition of Zr-salt when the concentration x > 0.05. Hence, the magnetization increases up to the composition with x = 0.15. The decrease in magnetization beyond a certain composition is due to the presence of higher amount of amorphous or crystalline NiO/ZrO_2 phases in the system, which is either antiferromagnetic or nonmagnetic respectively.

The magnetization value at 20 K Oe for all the composites are low compared to bulk magnetization value of Ni (55 emu/g). In literature it is reported that the decrease in saturation magnetization (M_S) might be due to decrease in particle size [119], disordered structure at the interface, such as that found at a grain boundary [56], or presence of surface layers which are either spin disordered (canted moments in the oxide coating) or magnetically dead [120, 121]. In Ni: NiO/ZrO_2 nanocomposite system, the presence of antiferromagnetic NiO and amorphous or crystalline nature of ZrO_2 give rise to decreases of magnetization value.

In nanoparticle systems with ferromagnetic/ antiferromagnetic interfaces, exchange coupling takes place across the interface leading to a reduction of the effective superparamagnetic limit [114] and also biasing of the magnetic hysteresis loop [122]. If the

nanoparticle system is cooled to $T < T_N$, the Néel temperature of the antiferromagnetic material in an external magnetic field, the antiferromagnetic moment exchange couples to the magnetization in the ferromagnetic layer to minimize the interaction energy of the system. In the case of Ni: NiO, the Néel temperature of antiferromagnetic NiO is 523 K, which is below the Curie temperature of Ni, 627 K. Hence, the system behaves as an exchange coupled system for temperatures < 300 K. The large coercivity of these samples at 85 K supports the presence of exchange coupling in these encapsulated particles [123, 124]. It is possible that anisotropy contribution is very high at 85 K compared to that at room temperature and is also indicated by higher coercivity and non saturation behavior at 85 K.

The amount of Ni in each of these composites can be determined based on the saturation magnetization (M_s) of pure Ni, as the magnetization is proportional to concentration. The weight fraction of Ni in these nanocomposites based on the magnetization value at room temperature is given in Table 6.5. The weight percentage of Ni obtained from the magnetization values and the electro-transport behavior of the composites (heat treated both at 723 K and 923 K in H_2 atmosphere) measured at room temperature can be correlated and is shown in Fig. 6.19. It can be seen that the weight fraction of Ni obtained from magnetization and the resistivity value obtained from the d.c four probe technique vary exactly oppositely with Zr-salt content. Initially the increase of weight fraction of Ni content (up to certain composition) in the composites lead to a better inter-particle connectivity and thus decreases the resistivity value up to that limit. Beyond this concentration, the Ni particles become isolated and thus result in a decrease of both conductivity and magnetization.

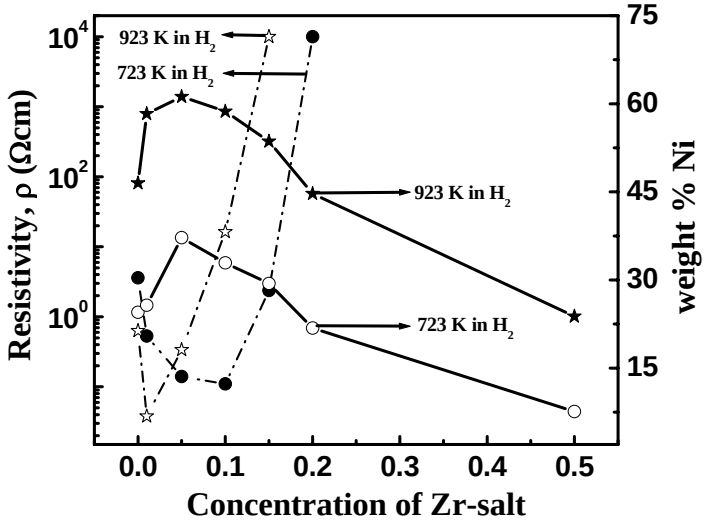

Fig. 6.19: The resistivity of the composites (heat-treated at 723 K and 923 K) at room temperature obtained from d.c four probe technique and the weight fraction of Ni determined from magnetization show an opposite dependence on Zr-O content.

Table 6.5: Magnetization data of the Ni: NiO/ZrO_2 nanostructures

Sample	**At room temperature**			**At 85 K**		**T_c (K)**
	H_c (Oe)	M (emu/g) at 20 KOe	Weight % Ni	H_c (Oe)	M (emu/g) at 20 KOe	
As-prepared						
x = 0	98	1.5	2.7	127	8.8	610
x = 0.01	121	3.7	6.7	169	9.2	---
x = 0.05	200	6.0	10.9	272	10.7	643
x = 0.10	200	9.8	17.8	332	14.5	637
x = 0.15	185	8.7	15.8	245	13.6	629
x = 0.20	171	7.7	14	201	13.0	625
x = 0.50	155	3.5	6.3	221	5.8	622
723 K in H_2						
x = 0	157	13.5	24.5	291	19.1	638
x = 0.01	148	13.9	25.7	256	18.9	---
x = 0.05	142	20.5	37.2	206	24.2	---
x = 0.10	105	18.1	32.9	161	21.5	638
x = 0.15	93	16.2	29.4	159	21.4	---
x = 0.20	81	12.0	21.8	119	16.7	---
x = 0.50	75	4.2	7.6	95	5.7	---
923 K in H_2						
x = 0	165	25.6	46.5	263	28.6	617
x = 0.01	172	32.1	58.3	350	36.2	---
x = 0.05	160	33.7	61.2	298	38.6	---
x = 0.10	125	32.3	58.7	225	34.3	626
x = 0.15	127	29.5	53.6	220	31.1	---
x = 0.20	124	24.6	44.7	215	26.7	---
x = 0.50	120	13.1	23.8	275	14.1	---
723 K in Air						
x = 0	208	14.2	25.8	364	17.6	631
x = 0.01	153	14.7	26.7	325	17.7	---
x = 0.05	211	15.5	28.2	306	22.1	---
x = 0.10	130	11.9	21.6	213	15.4	631
x = 0.15	125	9.7	17.6	208	13.2	---
x = 0.20	116	8.8	16	171	11.2	---
x = 0.50	99	3.8	6.9	167	7.5	---
923 K in Air						
x = 0	130	4.0	7.2	269	7.1	629
x = 0.01	138	3.2	5.8	212	4.9	---
x = 0.05	146	1.3	2.3	184	2.9	---
x = 0.10	163	2.7	4.9	179	4.0	628
x = 0.15	115	4.4	8	168	10	---
x = 0.20	160	3.8	6.9	135	6.1	---
x = 0.50	175	3.0	5.4	160	4.3	---

The magnetization as a function of temperature (85 to 400 K) of the Ni: NiO/ZrO_2 nanocomposites have been studied in detail. Zero field cooled (ZFC) and field cooled (FC) data are recorded in a field of 100 Oe. The dependence of M_{ZFC} (T) and M_{FC} (T) on temperature is presented in Fig. 6.20 (a – e) for composites of composition x = 0 heat-treated at two different temperatures in H_2 as well as in air atmosphere.

The as-prepared composite of composition x = 0 in Fig. 6.20 (a) indicates a superparamagnetic behavior with a blocking temperature T_B just above room temperature at 315 K. Below T_B, the magnetization is blocked i.e. magnetization can not relax during the time of measurements. The narrow divergence of ZFC and FC curve of the as-prepared composites (x = 0) indicates the smaller size and narrow particle size distribution in this composite which agrees with the grain size obtained from XRD pattern as well as size distribution curve (Fig. 6.12 a). The particle size obtained from the blocking temperature of this composite (x = 0) using the formula $T_B = \frac{KV}{25k}$ is about 27 nm, which is in agreement with structural studies. Above T_B, the magnetization could be free to align with the field during measurement time and the magnetization curve versus applied field should exhibit no hysteresis loop as seen from the Inset of Fig. 6.20 (a).

The particle size of these composites increases with heat-treatment temperature and this results in a broad divergence of ZFC and FC curve of the heat-treated composites as seen in Fig. 6.20 (b to e). All the composites show superparamagnetic behavior above 400 K except for the composite heat-treated at 723 K in H_2 atmosphere. This indicates a superparamagnetic behavior with a blocking temperature T_B at around 400 K. The particle size obtained from the blocking temperature of this composite (x = 0) using the formula $T_B = \frac{KV}{25k}$ is about 30 nm. Here, ZFC curve increases with the increase of temperature due to large size and broad particle size distribution. The FC curve of all the composites increases linearly with decrease of temperature except for the as-prepared and composite heat-treated at 923 K (in air atmosphere). As measured earlier these two samples indicate the presence of larger amount of NiO (antiferromagnetic nature) in the composite.

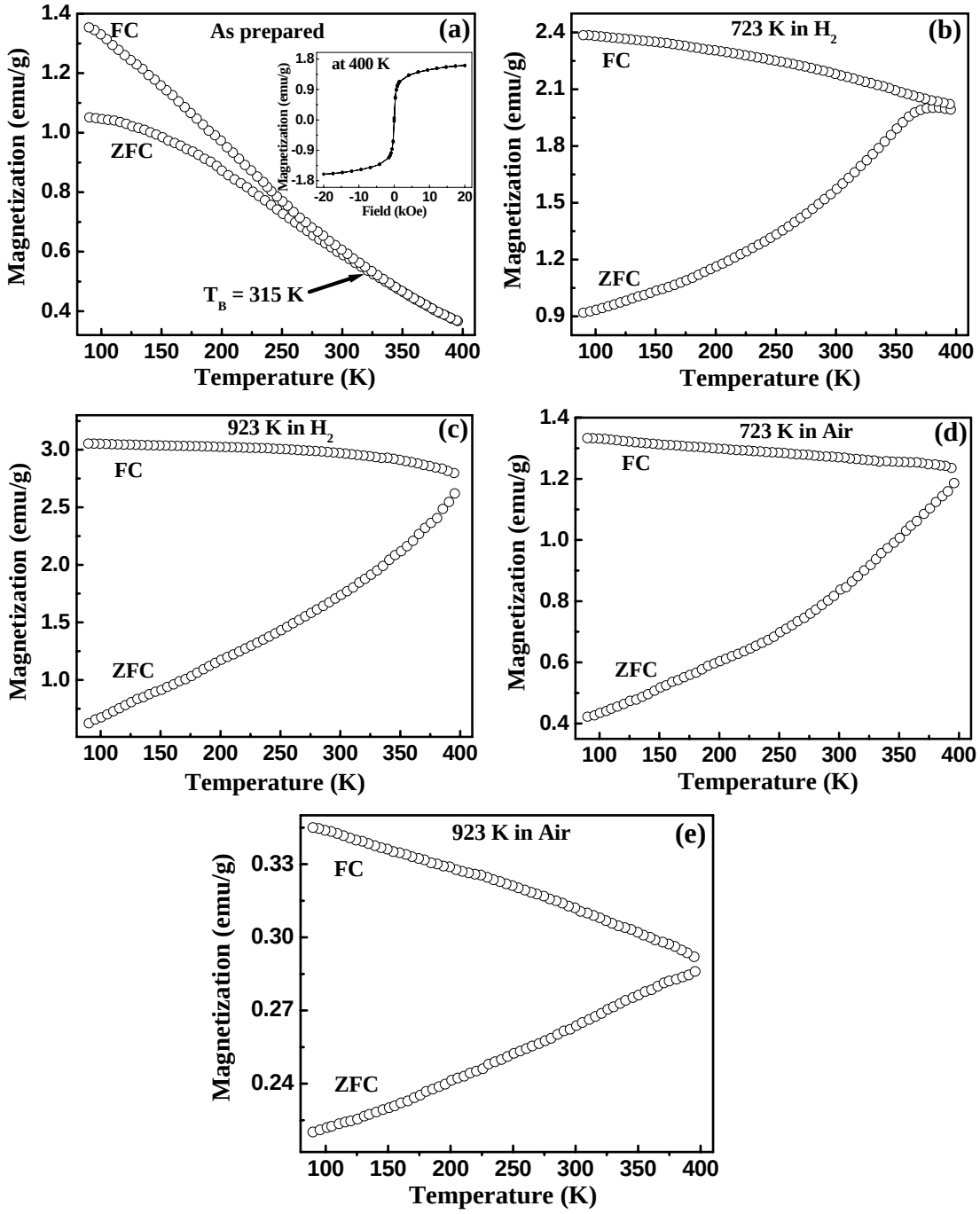

Fig. 6.20 (a) – (e): Temperature dependence of magnetization of the as-prepared composite of composition x = 0.0 and heat-treated at two different temperatures in H_2 as well as in air atmosphere. Inset of Fig. 6.21 (a) shows the M-H loop at 400 K, which indicates a superparamagnetic behavior.

The blocking temperature T_B depends on the size and distribution of the particles and varies as the strength of applied magnetic filed changes. Here two systems with two different particle sizes are considered for ZFC and FC data measured at different fields. The first one is

the as-prepared composite of composition x = 0 and the other one is as-prepared composite of composition x = 0.10. The particle size as well as the size distribution of second one is larger than the first one as seen from the Fig. 6.12.

The variation of zero-field-cooled (ZFC) and field cooled (FC) magnetization with temperature at different applied magnetic fields for the as-prepared composite of composition x = 0 and x = 0.10 are shown in Fig. 6.21 and Fig. 6.22 respectively.

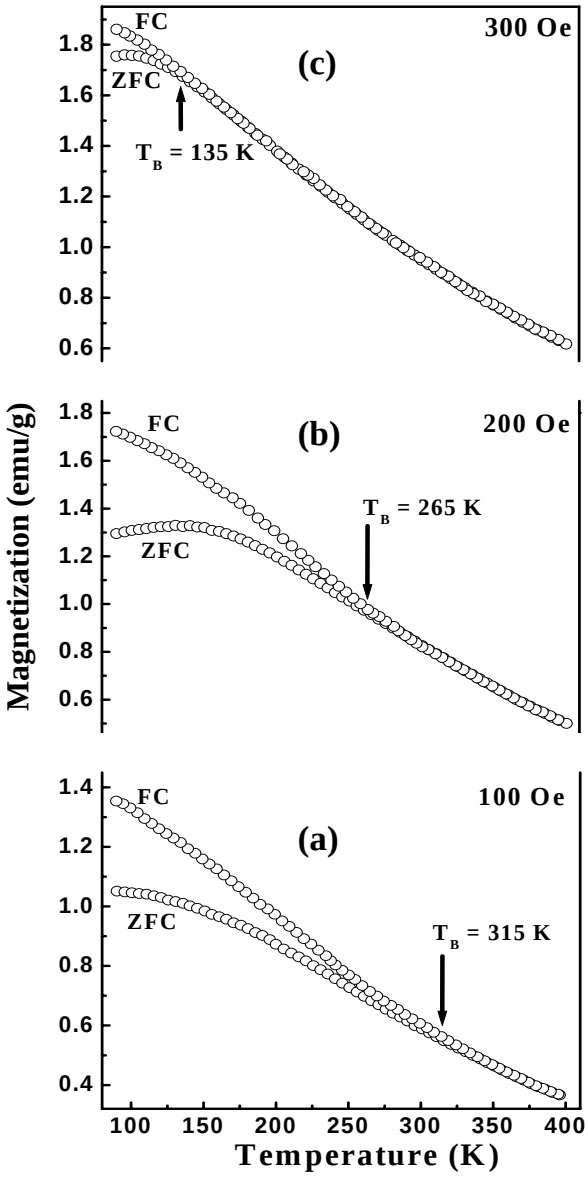

Fig. 6.21: Temperature dependence of magnetization for the as-prepared composite of composition x = 0.0 at different applied magnetic fields: (a) 100 Oe; (b) 200 Oe; and (c) 1000 Oe.

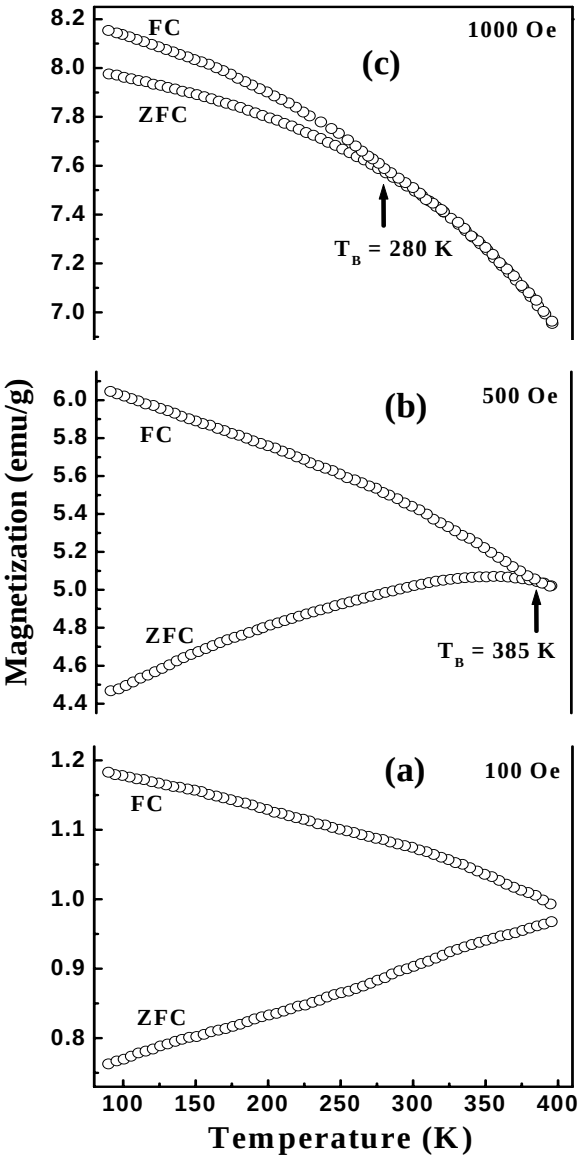

Fig. 6.22: Temperature dependence of magnetization for the as-prepared composite of composition x = 0.10 at different applied magnetic fields: (a) 100 Oe; (b) 500 Oe; and (c) 1000 Oe.

It is evident as a typical blocking behavior of superparamagnetic nanoparticles that the Ni: NiO/ZrO_2 composite show a different magnetization process when the composites are cooled below the blocking temperature with an applied magnetic field. Both the as-prepared composites (x = 0 and x = 0.10) show a decrease of irreversibility temperature with increasing applied field. It is interesting to observe that the strong irreversibility in the curves of composite x = 0 in Fig. 6.21 disappears when magnetic field is greater than 300 Oe. However, a higher magnetic applied field (> 1000 Oe) is required for disappearance of irreversibility curve for the composite x = 0.10 as seen from the Fig. 6.22. This could be related to size and size distribution of particle assembly in these composites [70].

The magnetic transition temperature (T_c) of Ni in the Ni: NiO/ZrO_2 nanocomposites were determined by performing magnetization studies in a field of 250 Oe. Fig. 6.23 shows the high temperature magnetic measurement of as-prepared composites in the temperature range 300 K to 800 K. Here it indicates two transitions at around 450 K and 630 K. The second transition at ~ 630 K indicates the magnetic transition T_C of Ni particles as it is equivalent to bulk Ni magnetic transition temperature (T_C = 627 K). As the Zr-salt content increases, there is no change in transition temperature of Ni nanoparticles indicating that there is no new phase formation due to reaction between Ni and Zr. The magnetic transition T_c for all the composites is given in Table 6.5.

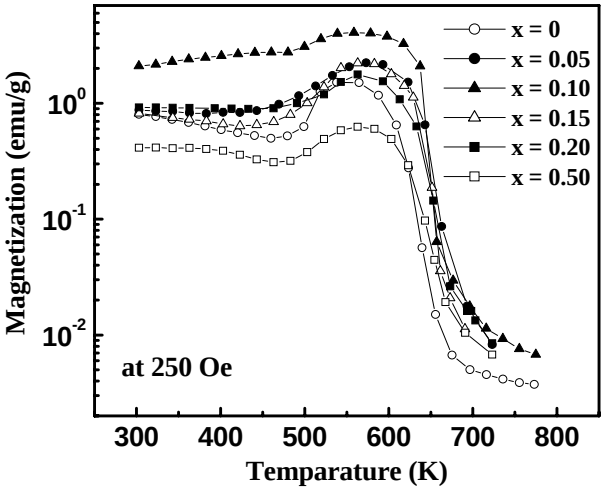

Fig. 6.23: Magnetization as a function of temperature at 250 Oe of the as-prepared composites

There is also no change of T_c of Ni when the composites are heat-treated at different temperatures either in H_2 or air atmosphere. Fig. 6.24 (a) and (b) show the high temperature magnetic measurement of the composites, x = 0 and 0.10 respectively, annealed at different

temperatures. It indicates that the T_c of Ni is same for all the composites. A broad transition at ~ 450 K is seen from high temperature magnetization of the as-prepared composites in Fig 6.23. This may be due to the presence of antiferromagnetic NiO or insulating ZrO_2 layer on the Ni core or in the composites. The as-prepared composite of composition x = 0 and x = 0.50 shows large amount of NiO or ZrO_2 in the composite as seen from the microstructural results. In the high temperature magnetization, these two samples show a large broad transition at ~ 450 K compared with other compositions. This broad transition decreases as Zr-salt increases due to decrease of NiO layer in the composite as observed from the microstructural results. The magnetization increases when the as-prepared composites are annealed in H_2 atmosphere due to the reduction of NiO, consistent with microstructural results.

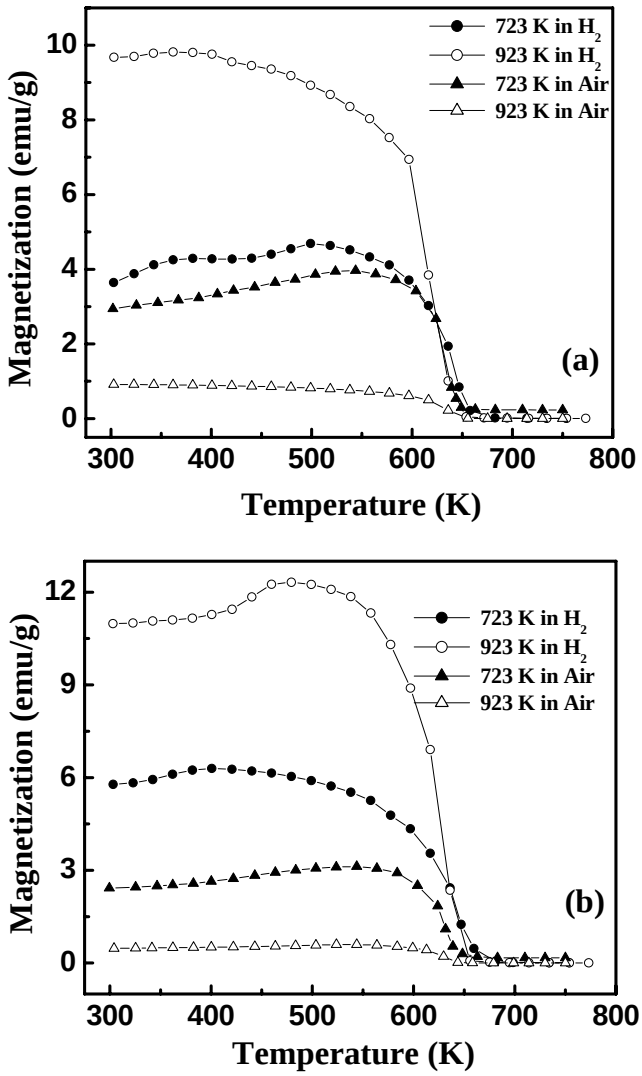

Fig.6.24: Magnetization as a function of temperature of as-prepared composites (a) x = 0 and (b) x = 0.10 annealed at different temperatures.

6.4 Summary

Nano crystalline Ni varying in size from 2 nm to 26 nm distributed in a non-magnetic matrix have been prepared by controlling the time of reaction and addition of $ZrOCl_2$ solution of different concentrations. Nanocomposites of Ni: NiO/ZrO_2 were synthesized by chemical reduction process using a reducing agent $NaBH_4$ followed by heat-treatment in H_2 atmosphere as well as in air atmosphere. The addition of Zr-salt is found to promote formation of large Ni grains and also prevent oxidation by encapsulation. Electrical transport behavior shows better interparticle connectivity for samples $x \leq 0.10$ while for $x \geq 0.10$, the interparticle connectivity is reduced due to ZrO_2 encapsulation for the composites. The formation of Ni: tetragonal (t) ZrO_2 composite is observed when the as-prepared composites were annealed at 923 K in H_2 atmosphere. The as-prepared composites show a superparamagnetic behavior with a blocking temperature of 315 K. The magnetization value of Ni is found to be less compared to bulk magnetization value due to the presence of antiferromagnetic NiO and nonmagnetic insulating ZrO_2 in the composite. The microstructural results together with the transport and magnetic properties of the nanoparticle system clearly show the potential of this technique to obtain size controlled property tuning.

Chapter 7

Conclusions

The present work deals with synthesis of composite materials consisting of magnetic nanoparticles dispersed in a magnetic or nonmagnetic insulating matrix and studies of their transport and magnetic properties. The composites of LCMO: Ni-ferrite, LCMO: SiO_2 using a nucleating agent and Ni: NiO/ZrO_2 have been synthesized using microwave refluxing, glass-ceramic and aqueous reduction processes respectively. The main advantage of these techniques is that they promote formation of composites at the nano level. The significant findings of this work are

1. LCMO nanoparticles exhibit orthorhombic and monoclinic forms depending on sintering temperature and Mn^{4+} concentration which is found to be a strong function of precursor pH and heat treatment temperature. The resistivity (ρ), magnetoresistance (MR), metal – insulator transition (T_{MI}) and the magnetic transition (T_c) strongly are found to depend on the Mn^{4+} concentration, grain size, pH of the precursor solution and the annealing temperature. From these studies, it is found that LCMO prepared from a precursor solution with a pH of 11.5 has better CMR properties over a wide temperature range. Therefore, these conditions are used for the synthesis of LCMO: $NiFe_2O_4$ (NF) nanocomposite by microwave refluxing process.

2. LCMO and NF nanocomposites have been prepared by microwave refluxing technique at moderate temperature, which is not possible by solid-state technique. Structural transition from monoclinic to orthorhombic form of LCMO takes place with increasing NF concentration when sintered at high temperatures, 1473 K. Increase in the tolerance factor due to substitution of Mn^{3+} ion by Fe^{3+} with lower ionic radii is responsible for a transition from low to high symmetry structure. The lowering of electrical and magnetic transition temperatures coupled with an increase in absolute resistivity with the addition of NF to LCMO observed in the present work indicates that the double exchange process in LCMO is severely affected.

3. The important factor for making composites through glass-ceramic process is the selection of a composition which forms glass on quenching the melt. The presence of an efficient nucleating agent, the determination of temperature and time of nucleation and growth acquire particular importance in the formation of glass-ceramic composite.

In this regard a condition for obtaining nanocomposite of LCMO with nonmagnetic SiO_2 with B_2O_3 addition is standardized. The effect of nucleating agents, Sb_2O_3 and Cr_2O_3 on the physical properties when compared with non-nucleated LCMO is studied. It is clearly observed that Sb_2O_3 and Cr_2O_3 play a more active role than merely aiding the process of nucleation of the crystalline phase. The structural and microstructural results show that Sb_2O_3 suppresses the secondary phase formation and simultaneously enhances the nucleation of LCMO phase while Cr_2O_3 has no significant effect on the nucleation behavior. Addition of Cr_2O_3 on the other hand changes the electrical transport behavior. LCMO phase is found to be highly disordered in the glassy matrix and hence is found to have inferior transport properties.

4. Different sizes and shapes of Ni nanoparticles and Ni: NiO/ZrO_2 nanocomposites have been prepared by a chemical reduction technique using $NaBH_4$ as a reducing agent. Crystalline Ni varying in size from 2 nm to 26 nm distributed in a non-magnetic matrix of NiO/ZrO_2 has been prepared by controlling the time of reaction and addition of $ZrOCl_2$ solution of different concentrations at room temperature. The crystalline Ni is found to be ferromagnetic at room temperature with a well-defined hysteresis and coercivity. The transport behavior of Ni: NiO/ZrO_2 (heat-treated at 723 K and 923 K in the presence of H_2 atmosphere) nanocomposites has been understood based on microstructural and magnetization behavior. Addition of Zr-salt aids Ni formation leading to better inter-particle connectivity and thus a decrease in the resistivity up to $x \leq 0.10$ (where x is the molar concentration of Zr-salt). For $x > 0.10$, the inter-particle connectivity is reduced due to ZrO_2 encapsulation and hence results in an increase in resistivity. This behavior is consistent with the magnetization variation with concentration of ZrO_2. Heat treatment of these nanocomposites under different conditions results in metal particles or embedded metal particles. The microstructural results together with the transport and magnetic properties of the nanoparticle system clearly show the potential of this technique to obtain size controlled property tuning.

APPENDIX

Ni and Ni-nickel oxide nanoparticles with different shapes and a core shell structure

Synthesis of ferromagnetic nanoparticles with various sizes and shapes and a core shell structure has received considerable interest in recent years due to their technological interest [125, 126]. In the present work, Ni nanoparticles with different shapes and having a core: shell structure of Ni: nickel oxide has been prepared by a combination of chemical and gaseous reduction. The first step involves chemical reduction of nickel chloride (1.0 M) in an aqueous medium with sodium borohydride, $NaBH_4$ (2.0 M). The precipitate was thoroughly washed with distilled water by repeated centrifuging in order to remove completely the water-soluble reaction products. In the second step, the as-prepared Ni-complex is reduced further in the presence of 2 % H_2 and 98 % Ar gas mixture at different temperatures ranging from 823 K to 1123 K. From the structural (X-ray diffraction) study, it was observed that Ni in the as-prepared powder is in a crystalline cluster form with a size of ~ 3.0 nm. Reducing the as-prepared Ni powder at 823 K in 2 % H_2 gas atmosphere leads to growth of the crystalline Ni clusters as well as development of Ni-oxide shell. As the temperature increase, nickel oxide shell decreases and complete elimination of the nickel oxide shell has observed when reduced at 1123 K. The crystallite size of Ni is determined using Debye Scherrer relation, and is found to be around 50 to 75 nm indicating no significant grain growth as the reduction temperature increases from 823 to 1123 K. Different shapes of nanograin Ni particles with a Ni-oxide shell structure were observed by transmission electron microscopy (Fig. A1).

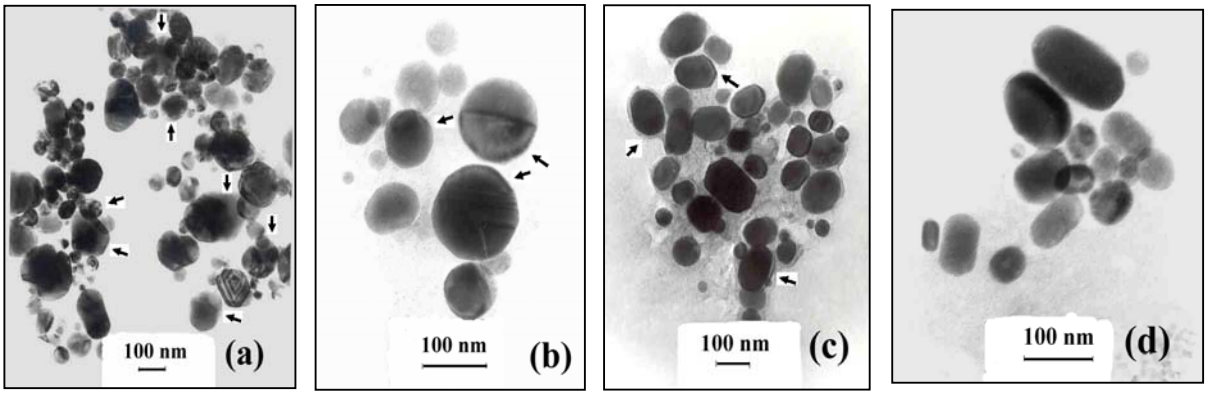

Fig. A1: TEM micrographs of Ni particles reduced at annealing temperatures of 823 K (a), 923 K (b), 1023 K (c) and 1123 K (d). Arrow indicates Ni-oxide shell on a Ni particle.

The shape of the particles varies from nearly spherical to cylindrical, hexagonal, ellipsoidal, and polyhedral. The average particle size varies from 20 to 120 nm for all the samples in agreement with X-ray results. The different shapes however were present in powders reduced at different temperatures indicating that the growth habitat is independent of temperature. The electrical transport study indicates that all samples show typical metallic behavior. The absolute resistivity decreases with increasing reduction temperature due to decreasing volume fraction of minor phase (Ni-oxide) in the system. The high value of resistivity is due to grain boundary scattering from Ni nanoparticles as well as due to the presence of small quantities of Ni-oxide. The magnetization M as a function of external field H at room temperature, 300 K and 5 K is shown in Fig. A2. The magnetization near saturation, at an external field of 20 kOe, for the Ni nanoparticles obtained after reduction at 1123 K is higher compared to that obtained after 823 K reduction. This is due to the presence of relatively higher Ni-oxide in the form of a shell around Ni-core after reduction at 823 K compared to 1123 K. A closer look at the magnetization at high fields, insets in Fig. A2, supports the presence of higher Ni-oxide after reduction at 823 K. The magnetization at 5 K does not reach saturation even at external fields of 20 kOe in the presence of thick Ni-oxide shell layer. The saturation magnetization of Ni obtained after reduction at 1123 K however is still lower than the equivalent bulk value due to the nano size as well as the presence of small amounts of oxide.

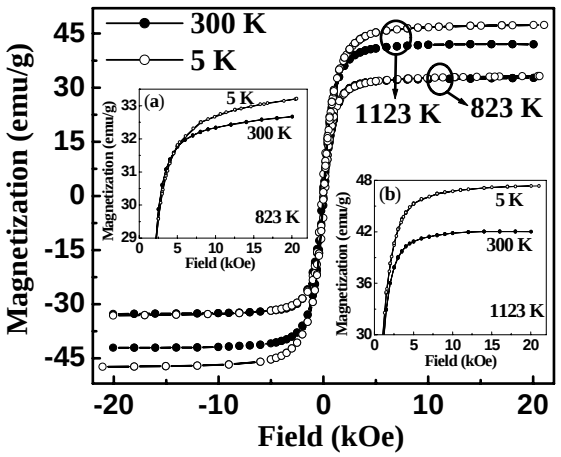

Fig. A2: The magnetization of Ni nanoparticles and Ni / Ni-oxide core / shell structures as a function of external field indicates different saturation behavior for reduction at 823 K (inset (a)) and 1123 K (inset (b)).

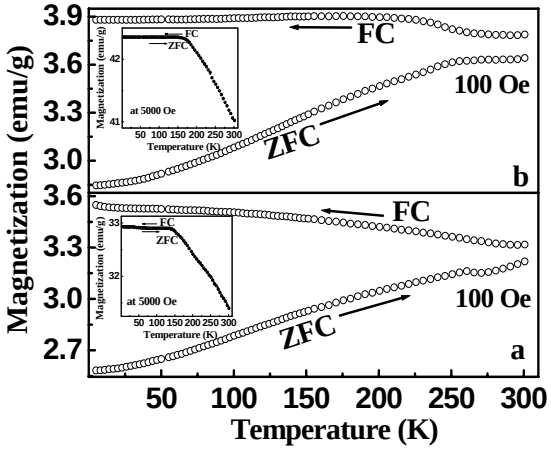

Fig. A3: Temperature dependence of magnetization of Ni nanoparticles and Ni / Ni-oxide core / shell structure in a field of 100 Oe shows thermal hysteresis. The hysteresis behavior vanishes at 5000 Oe (insets).

The electrical and magnetization data of Ni: Nickel oxide nanostructures along with that of pure bulk nickel are given in Table A1. The coercivity H_c of Ni / Ni-oxide structure obtained after reduction at 823 K increases with decreasing temperature from ~ 80 Oe at 300 K to 145 Oe at 5 K. The coercivity of nearly pure Ni nanoparticles obtained by reduction at 1123 K however remains a constant at ~ 21 Oe both at 300 K and 5 K. The Ni-oxide, NiO, is known to be antiferromagnetic and when present as a shell on the ferromagnetic Ni-core, pins the magnetization. At low temperatures, 5 K, a large external field H will be required to reverse the magnetization direction leading to an increase in the coercivity value compared to room temperature.

Table A1: Magnetization data of Ni: Ni-oxide nanostructures along with pure bulk Ni

Sample	At 300 K		At 5 K		Blocking temperature (T_B)	Resistivity (Ωcm) at 300 K
	H_C (Oe)	M_S (emu/g) at 20000 Oe	H_C (Oe)	M_S (emu/g) at 20000 Oe		
Ni_823	80	33	145	33	> 300 K	1.56×10^{-1}
Ni_1123	21	42	21	47	> 300 K	6.57×10^{-5}
Bulk Ni [125]	100	55	--	--	--	6.8×10^{-6}

The variation of magnetization with temperature in the range 5 K – 300 K in an external field of 100 Oe shows a path dependant hysteresis behavior both for the Ni-nanoparticles and Ni / Ni-oxide core-shell structures, Fig A3. In an external field of 5000 Oe however the hysteresis vanishes completely in both the cases. The presence of hysteresis at low fields and its absence at high fields is a characteristics feature of superparamagnetic behavior, observed in nanosize particles. The blocking temperature, T_B above which the magnetization is independent of the path is found to be > 300 K in 100 Oe external field. A broad variation of zero field cooled magnetization indicates the presence of a distribution of particles size, as seen in TEM Fig. A1.

References

[1]. R. W. Siegel, *Ann. Rev. Mater. Sci.*, **21**, 559 (1991).

[2]. H. Gleiter, *Prog. Mater. Sci.*, **33**, 223 (1989).

[3]. R. W. Siegel, *Nanostruc. Mater.*, **3**, 1 (1993).

[4]. J. M. D. Coey, *J. Magn. Magn. Matter.*, **196**, 1 (1999).

[5]. R. D. Shull and L. H. Bennett, Nanostruc. Mater., **1**, 83 (1992).

[6]. S. Gupta, R. Ranjit, C. Mitra, P. Raychaudhuri, and R. Pinto, *Appl. Phys. Lett.*, **78**, 362 (2001).

[7]. Y.-H. Huang, X. Chen, Z.-M. Wang, C.-S. Liao, C.-H. Yan, H.-W. Zhao, and B.-G. Shen, *J. Appl. Phys.*, **91**, 7733 (2002).

[8]. C.-H. Yan, Z.-G. Xu, T. Zhu, Z.-M. Wang, F.-X. Cheng, Y.-H. Huang, and C.-S. Liao, *J. Appl. Phys.*, **87**, 5588 (2000).

[9]. R. C. O'Handley, Modern magnetic materials principles and applications, *John Wiley and Sons, Inc.*, pp 435, (2000).

[10]. C. Zener, *Phys. Rev.*, **82**, 403 (1951).

[11]. S.-W Cheong and H.-Y Hwang in Y. Tokura (Ed.) Contribution to CMR Oxides, Monographs in Condensed Matter Science, Gordon & Breach, Londona (1999).

[12]. J. H. Van Santen and G. H. Jonker, *Physica*, **16**, 599 (1950).

[13]. N.-C. Yeh, R. P. Vasquez, D. A. Beam, C.-C. Fu, J. Huynh and G. Beach, *J. Phys. Conden. Mater.*, **9**, 3713 (1997).

[14]. G. Jakob, W. Westerburg, F. Martin and H. Adrian, *Phys. Rev. B*, **58**, 14966 (1998).

[15]. N. F. Mott, "Metal-Insulator transitions" Taylor and Francis, London, 1974.

[16]. J. M. D. Coey, M. Viret, L. Ranno and K. Ounadjela, *Phys. Rev. Lett.*, **75**, 3910 (1995).

[17]. G. J. Synder, R. Hiskes, S. DiCarolis, M. R. Beasley and T. H. Geballe, *Phys. Rev. B*, **53**, 14434 (1996).

[18]. K. Kubo and N. Ohata, *J. Phys. Soc. Japan*, **33**, 21 (1972).

[19]. Colossal Magnetoresistive Oxides, edited by Y. Tokura (Gordon & Breach, Tokyo, 1999).

[20]. T. Tang, S. Y. Zhang, R. S. Huang, and Y. W. Du, *J. Alloys and Comp.*, **353**, 91 (2003).

[21]. J. Rivas, L. E. Hueso, A. Fondado, F. Rivadulla and M. A. López-Quintela, *J. Magn Magn. Mater.*, **221**, 57 (2000).

[22]. L. Balcells, A. E. Carrillo, B. Martinez and J. Fontcuberta, *Appl. Phys. Lett.*, **74**, 4014 (1999).

[23]. D. K. Petrov, L. K.-Elbaum, J. Z. Sun, C. Field and P.R. Duncombe, *Appl. Phys. Lett.*, **75,** 995 (1999).

[24]. Z. C. Xia, S. L. Yuan, L. J. Zhang, G. H. Zhang, W. Feng, J. Tang, L. Liu, S. Liu, J. Liu, G. Peng, Z. Y. Li, Y. P. Yang, C. Q. Tang and C. S. Xiong, *Solid State Commun.*, **125**, 571 (2003).

[25]. Y.-H. Huang, C.-H. Yan, S. Wang, F. Luo, Z.-M. Wang, C.-S. Liao, and G.-X. Xu, *J. Mater. Chem.*, **11**, 3296 (2001).

[26]. L. E. Hueso, J. Rivas, F. Rivadulla, and M. A. López-Quintela, *J. Appl. Phys.*, **89**, 1746 (2001).

[27]. S. A. Köster, V. Moshnyaga, K. Samwer, O. I. Lebedev, G. V. Tendeloo, O. Shapoval and A. Belenchuk, *Appl. Phys. Lett.*, **81**, 1648 (2002).

[28]. O. A. Shlyakhtin, K. H. Shin and Y.-J. Oh, *J. Appl. Phys.*, **91**, 7403 (2002).

[29]. Q. Huang, J. Li, X. Huang, C. K. Ong, and X. S. Gao, *J. Appl. Phys.*, **90**, 2924 (2001).

[30]. R. Müller, W. Schüppel, T. Eick, H. Steinmetz and E. Steinbeiß, *J. Magn. Magn. Mater*., **217**, 155 (2000)

[31]. R. Müller, W. Schüppel, T. Eick, H. Steinmetz and E. Steinbeiß, *J. Euro. Ceram. Soc.*, **21**, 1941 (2001)

[32]. C.-H. Yan, Y.-H. Huang, X. Chen, C.-S. Liao and Z.-M. Wang, *J. Phys.*, **14**, 9607 (2002).

[33]. H. C. Seop, K. W. Seop and H. N. Hwi, *Solid State Commun.*, **121**, 657 (2002).

[34]. C.-H. Yan, F. Luo, Y.-H. Huang, X.-H. Li, Z.-M. Wang, C.-S. Liao, H. W. Zhao and B.-G. Shen, *J. Appl. Phys.*, **91**, 7406 (2002).

[35]. J.-M. Liu, G. L. Yuan, H. Sang, Z. C. Wu, X. Y. Chen, Z. G. Liu, Y. W. Du, Q. Huang and C. K. Ong, *Appl. Phys. Lett.*, **78**, 1110 (2001).

[36]. G. L. Yuan, J.-M. Liu, Z. G. Liu, Y. W. Du, H. L. W. Chan and C. L. Choy, *Mater. Chem. Phys.*, **75**, 161 (2002).

[37]. Y.-H. Huang, C.-H. Yan, Z.-M. Wang, C.-S. Liao and G.-X. Xu, *J. Alloys Comp.*, **349**, 224 (2003).

[38]. Y.-H. Huang, C. H. Yan, F. Luo, W. Song, Z.-M. Wang and C.-S. Liao, *Appl. Phys. Lett.*, **81**, 76 (2002).

[39]. S. Pal, A. Banerjee and B. K. Chaudhuri, *J. Phy. Chem. Sol.*, **64**, 2063 (2003).

[40]. X.H. Li, Y.-H. Huang, Z.-H. Wang and C.-H. Yan, *Appl. Phys. Lett.*, **81**, 307 (2002).

[41]. D. Das, P. Chowdhury, R.N. Das, C.M. Srivatsava, A.K. Nigam and D. Bahadur, *J. Magn. Magn. Mater.*, **238**, 178 (2002).

[42]. D. Das, C. M. Srivastava, D. Bahadur, A. K. Nigam, and S. K. Malik, *J. Phys: Condens Mater.*, **16**, 4089 (2004).

[43]. D. Das, A. Saha, C. M. Srivastava, R. Raj, S. E. Russek and D. Bahadur, *J. Appl. Phys.*, **95**, 7106 (2004).

[44]. D. Das, A. Saha, S. E. Russek, R. Raj and D. Bahadur, *J. Appl. Phys.*, **93**, 8301 (2003).

[45]. R. D. Shannon and C. T. Prewitt, *Acta Crystallogr. B*, **25**, 925 (1969).

[46]. D. Das, M. R. Raj, C. M. Srivastava, A. K. Nigam, D. Bahadur and S. K. Malik, *J. Phys: Condens Matter.*, **16**, 6213 (2004).

[47]. V. P. Dravid, J. J. Host, M. H. Teng, B. Elliott, J. Hwang, D. L. Johnson, T. O. Mason, and J. R. Weertman, *Nature*, **374**, 602 (1995).

[48]. H. E. Schaefer, H. Kisker, H. Kronmüller and R. Würschum, *Nanostruct. Mater.*, **1**, 523, (1992).

[49]. C. L. Chien, John Q. Xiao and J. Samuel Jiang, *J. Appl. Phys.*, **73**, 5309 (1993).

[50]. A. G. Evans, *J Amer Ceram Soc.*, **73**, 187 (1990).

[51]. R. Riedel, H. J. Kleebe, H. Schonfelder, F. Aldinger, *Nature*, **374**, 526 (1995).

[52]. S.-H. Wu and D.-H. Chen, *J. Colloid Interface Sci.*, **259**, 282 (2003).

[53]. R. W. Siegel and H. Hahn, in M. Yussouff (ed.), "*Current Trends in Physics of Materials*", World Scientific, Singapore, pp. 403 (1987).

[54]. J. Legrand, A. Taleb, S. Gota, M.J. Guittet and C. Petit, *Langmuir*, **18**, 4131 (2002).

[55]. G. N. Glavee, K. J. Klabunde, C. M. Sorensen and G. C. Hadjipanayis, *Langmuir*, **10**, 4726 (1994).

[56]. J. H. Hwang, V.P. Dravid, M.H. Teng, J.J. Host, B.R. Elliott, D.L. Johnson and T.O. Mason. *J. Mater. Res.*, **12**, 1076 (1997).

[57]. J. M. Broto, J. C. Ousset, H. Rakoto, S. Askenazy, Ch. Dufor, M. Brieu, and P. Mauret, *Solid State Commun.*, **85**, 263 (1993).

[58]. H. Tao Zhang, G. Wu, X.H. Chen, X.G. Qiu, *Mater. Res. Bull.*, (2005) (in press).

[59]. J.-S. Jung, W.-S. Chae, R. A. Mclntyre, C. T. Seip, J. B. Wiley, and C. J. O'Connor, *Mater. Res. Bull.*, **34**, 1353 (1999).

[60]. O. C.- González, C. Estournés, M. R.-Plouet, J. L. Guille, *Mater. Sc. Engg. C*, **15**, 179 (2001).

[61]. O. Aharon, S. Bar-Ziv, D. Gorni, T. Cohen-Hyams, W.D. Kaplan, *Scripta Materialia*, **50**, 1209 (2004).

[62]. J.E. Sundeen, R.C. Buchanan, *Sensors and Actuators A*, **90**, 118 (2001).

[63]. N. Q. Minh, *J. Am. Ceram. Soc.*, **76**, 563 (1993).

[64]. H. Uchida, H. Suzuki, and M. Watanabe, *J. Electrochem. Soc.*, **145**, 615 (1998).

[65]. K. Eguchi, *J. Alloys Compd.*, **250**, 486 (1997).

[66]. S. J. A. Livermore, J. W. Cotton, and R. M. Ormerod, *J. Power Sources*, **86**, 411 (2000).

[67]. H. Konno and H. Kataniwa, *J. Appl. Phys.*, **69**, 5933 (1991).

[68]. M. H. Kryder, *Thin Solid Films*, **216**, 174 (1992).

[69]. N. J. Tang, W. Zhong, W. Liu, H. Y. Jiang, X. L. Wu and Y. W. Du, *Nanotechnology*, **15**, 1756 (2004).

[70]. X. Sun, M.J. Yacaman, *Mater. Sci. Engg. C*, **16**, 95 (2001).

[71]. A. Roy, V. Srinivas, S. Ram, J. A. De Toro and J. M. Riveiro, *J. Appl. Phys.*, **96** 6782 (2004).

[72]. A. Roy, V. Srinivas, S. Ram, J. A. De Toro and U. Mizutani, *Phys. Rev. B*, **71**, 184443 (2005).

[73]. A. Bhaskar, B. Rajini Kanth and S. R. Murthy, *MSI Bulletin*, **25**, 17 (2002).

[74]. J. Giri, T. Sriharsha and D. Bahadur, *J. Mater. Chem.*, **14**, 875 (2004).

[75]. H. M. Rietveld, *J. Appl. Cryst.*, **2**, 65 (1969).

[76]. R. A. Young, *Rietveld Method*, International Union of Crystallography, Oxford University Press (1996).

[77]. A. I. Vogel, A text book quantitative inorganic analysis including elementary instrumental analysis, 3rd ed. pp. 343-354, ELBS, New York (1978).

[78]. D. Mogilyansky, G. Jung, V. Markovich, C.J. van der Beek and Ya.M. Mukovskii, ***Physica B: Condensed Matter***, **378**, 510 (2006)

[79]. M. Pissas, I. Margiolaki, G. Papavassiliou, D. Stamopoulos, and D. Argyriou, *Phys. Rev. B* **72**, 064425, (2005)

[80]. S. Surthi, S. Kotru, R. K. Pandey and P. Fournier, *Solid State Commun.*, **125**, 107 (2003)

[81]. H. Y. Hwang, S. W. Cheong, P. G. Radaelli, M. Marezio and B. Battlog, *Phys. Rev. Lett.*, **75**, 914 (1995).

[82]. Y.-K. Tang, Y. Sui, D.-P. Xu, Z.-N. Qian and W.-H. Su, *J. Magn. Magn. Mater.* **299**, 260 (2006)

[83]. E. Dagotto, T. Hotta, and A. Moreo, *Phys. Reports*, **344**, 1 (2001).

[84]. H. Y. Hwang, S. W. Cheong, N. P. Ong and B. Batlogg, *Phys. Rev. Lett.*, **77**, 2041 (1996).

[85]. M. Jaime, P. Lin, M. B. Salamon, and P. D. Han, *Phys. Rev. B*, **58**, R5901 (1998).

[86]. M. Jaime, P. Lin, S. H. Chun, M. B. Salamon, P. Dorsey, and M. Rubinstein, *Phys. Rev. B*, **60**, 1028 (1999).

[87]. A. Alexandrov, and A. M. Bratkovsky, *J. Appl. Phys.*, **85**, 4349 (1999).

[88]. G.-M. Zhao, V. Smolyaninova, W. Prellier, and H. Keller, *Phys. Rev. Lett.*, **84**, 6086 (2000).

[89]. P. Dai, J.A. Fernandez-Baca, N. Wakabayashi, E.W. Plummer, Y. Tomioka and Y. Tokura, *Phys. Rev. Lett.*, **85**, 2553 (2000).

[90]. P. Schiffer, A. P. Ramirez, W. Bao and S.-W. Cheong, *Phys. Rev. Lett.*, **75**, 3336 (1995).

[91]. G. Li, H.-D. Zhou, S. J. Feng, X.-J. Fan, X.-G. Li, and Z. D. Wang, *J. Appl. Phys.*, **92**, 1406 (2002).

[92]. M Uehara, S. Mori, C. H. Chen, and S.-W. Cheong, *Nature*, **399**, 560 (1999).

[93]. J. C. Loudon, N. D. Mathur, and P. A. Midgley, *Nature*, **420**, 797 (2002).

[94]. A. Moreo, S. Yunoki, and E. Dagotto, *Phys. Rev. Lett.*, **83**, 2773 (1999).

[95]. In-Bo Shim, Seung-Young Bae, Young-Jei Oh and Se-Young Choi, *Solid State Ionics*, **108**, 241 (1998).

[96]. J.R. Gebhardt, S. Roy and N. Ali, *J. Appl. Phys,*. **85**, 5390 (1999).

[97]. M. C. Walsh, M. Foldeaki, A. Giguere, D. Bahadur, S.K. Mandal and R.A. Dunlap, *Physica B* **253**, 103 (1998).

[98]. F. M. Araujo-Moreira, M. Rajeswari, A. Goyal, K. Ghosh, V. Smolyaninova, T. Venkatesan, C.J. Lobb and R.L. Greene, *Appl. Phys. Lett.* **73**, 3456 (1998).

[99]. L L Balcells, J Fontcuberta, B Martínez and X Obradors, *J. Phys.: Condens. Matter* **10**, 1883 (1998)

[100]. X. W. Li, A. Gupta, Gang Xiao and G.Q. Gong, *Appl. Phys. Lett.*, **71**, 1124 (1997)

[101]. K. H. Ahn, X. W. Wu, K. Liu and C. L. Chien, *Phys. Rev. B*, **54**, 15299 (1996).

[102]. J. R. Sun, G. H. Rao, B. G. Shen and H. K. Wong, *Appl. Phys. Lett.*, **73**, 2998 (1998).

[103]. O. Toulemonde, F. Studer and B. Raveau, *Solid State Commn.*, **118**, 107 (2001).

[104]. A. Pena, J. Guiterrez, J.M. Barandiaran and T. Rojo, *J. Magn. Magn. Mater.*, **272**, 1425 (2004).

[105]. K. S. Shankar, S. Kar, G.N. Subbanna and A.K. Raychaudhuri, *Solid State Commn.*, **129**, 479 (2004).

[106]. P. W. McMillan, “Glass-ceramics” (Academic Press London, 1979) Page 1-5.

[107]. N. Rezlescu, E. Rezlescu, I. Ciobotaru, M. L. Craus and P. D. Popa, *Ceram. Inter.*, **24**, 31 (1998).

[108]. D. Bahadur, M. Yewondwossen, Z. Koziol, M. Foldeaki and R. Dunlap, *J. Phys.: Condens. Mater.*, **8**, 5235 (1996).

[109]. Y. Sun, X. Xu and Y. Zhang, *Phys. Rev. B*, **63**, 054404 (2000).

[110]. Y. Sun, W. Tong, X. Xu and Y. Zhang, *Appl. Phys. Lett.*, **78**, 643 (2001).

[111]. H. L. Jhu and H. Sohn, *J. Magn. Magn. Mater.*, **167**, 200 (1997).

[112]. S. P. Isaac, N. D. Mathur, J. E. Evetts and M. G. Blamire, *Appl. Phys. Lett.*, **72** 2038 (1998).

[113]. A. Gupta, G. Q. Gong, G. Xiao, P. R. Duncombe, P. Leconeur, P. trilloud, Y. Y. Wang, V. P. Dravid and J. Z. Sun, *Phys. Rev. B*, **54**, R15629 (1996).

[114]. V. Skumryev, S. Stoyanov, Y. Zhang, G. Hadjipanayis, D. Givord and J. Nogués, *Nature*, **423**, 85 (2003).

[115]. Annual Book of ASTM standards, 1916 Race Street, PA,1989, 15, C373–88, pp. 109– 110.

[116]. J. E. Sundeen and R. C. Buchanan, *Sensors and Actuators A*, **63**, 33 (1997).

[117]. J. M. Rojo, A. Hernando, M. El Ghannami, A. Garcia-Escorial, M. A. Gonzalez, R. Garcia-Martinez, and L. Ricciarelli, *Phys. Rev. Lett.*, **76**, 4833 (1996).

[118]. S.-J. Park, S. Kim, S. Lee, Z. G. Khim, K. Char, and T. Hyeon, *J. Am. Chem. Soc.*, **122**, 8581 (2000).

[119]. V. P. M. Shafi, A. Gedanken, R. Prozorov and J. Balogh, *Chem. Mater.*, **10**, 3445 (1998).

[120]. P. Zhang, F. Zuo, F. K. Urban, A. Khabari, P. Griffiths and A. Hosseini-Tehrani, *J. Magn. Magn. Mater.*, **225**, 337 (2001).

[121]. S. Gangopadhyay, G. C. Hadjipanayis, B. Dale, C. M. Sorensen, K. J. Klabunde, V Papaefthymiou and A. Kostikas, *Phys. Rev. B*, **45**, 9778 (1992).

[122]. W. H. Meiklejohn, *J. Appl. Phys.*, **33**, 1328 (1962).

[123]. X.-C. Sun and X.-L. Dong, *Mat. Res. Bull.*, **37**, 991 (2002).

[124]. O. Palchik, S. Avivi, D. Pinkert and A. Gedanken, *Nanostruc. Mater.*, **11**, 415 (1999).

[125]. X. Lu, G. Liang, Z. Sun and W. Zhang, *Mater. Sc. Engg. B*, **117**, 147 (2004).

[126]. S. Illy-Cherrey, O. Tillement, J.M. Dubois, F. Massicot, Y. Fort, J. Ghanbaja and S. Bégin-Colin, *Mater. Sci. Eng, A*, **338**, 70 (2002).

Publications resulting from the Ph.D work

1. "Ni and Ni-nickel oxide nanoparticles with different shapes and a core shell structure" **Bibhuti B. Nayak**, Satish Vitta, A. K. Nigam and D. Bahadur, *Thin Solid Films* **505**, 109 (2006).
2. "Transport and magnetic properties of encapsulated Ni – Ni-O/Zr-O nanostructures" **Bibhuti B. Nayak**, Satish Vitta, A. K. Nigam and D. Bahadur, *IEEE Transaction on Magnetics*, **41**, 3298 (2005).
3. "Mixed mode electrical transport in nanocrystalline La-Ca-Manganite synthesized by Microwave refluxing" **Bibhuti B. Nayak**, Satish Vitta, and D. Bahadur, *Physica Status Solidi A*, **202**, 2790 (2005).
4. "Processing, properties and some novel applications of magnetic nanoparticles" D. Bahadur, J. Giri, **Bibhuti B. Nayak**, P. Pallab, T. Sriharsha, K. C. Barick, R. Ambashta, *Pramana – J. Physics*, **65**, 663 (2005).
5. "Structure and properties of La-Ca-Mn-O composites prepared by the glass-ceramic method" **Bibhuti B. Nayak**, Satish Vitta, D. Bahadur and A.K. Nigam, *Materials Science and Engineering B*, **113**, 50 (2004).
6. "Microstructural evolution and magnetic behavior of Ni/ZrO_2 nanocomposites" **Bibhuti B. Nayak**, Satish Vitta, and D. Bahadur (Submitted to Langmuir).

Research Presentation

1. "Transport and magnetic properties of encapsulated Ni – Ni-O/Zr-O nanostructures" **Bibhuti B. Nayak**, Satish Vitta, A. K. Nigam and D. Bahadur – was presented in *International Conference on Magnetics **INTERMAG 2005**,* 4-8th April, Nagoya, JAPAN .
2. "Ni and Ni-nickel oxide nanoparticles with different shapes and a core shell structure", **Bibhuti B. Nayak**, Satish Vitta, A. K. Nigam and D. Bahadur – was presented in *International conference: **ICMAT2005,** 3-8 July 2005,* Singapore.
3. "Magnetic behavior of $La_{0.67}Ca_{0.33}MnO_3$: SiO_2 nanocomposite prepared by glass ceramic process", **Bibhuti B. Nayak**, A. K. Nigam, Satish Vitta and D. Bahadur – was presented in *International Symposium on Recent Advances in Inorganic Materials (**RAIM 2002**), IIT Bombay, Dec 11-13, 2002.*
4. "Electrical and Magnetic properties of La-Ca-Mn-O / SiO_2 nanocomposite through glass ceramic route", **Bibhuti B. Nayak**, S. Asthana**,** A. K. Nigam, Satish Vitta and D. Bahadur – was presented in ***In house Symposium on Nanotechnology** at IIT Bombay, (IRCC) 13th Sept 2003*.
5. "Nanograined alloys and composites for temperature sensor application", **Bibhuti B. Nayak**, A. Khuntia, Satish Vitta and D. Bahadur – was presented in *In house Symposium on **Materials Research MR04** @ Department of Metallurgical Engineering and Materials Science, IIT Bombay, 27th March 2004*.